The Dissertation Committee for Feng Liu
certifies that this is the approved version of the following dissertation:

Sparse Representation and Learning for Discriminative EEG Source Imaging

Committee:

Dr. Shouyi Wang, Co-Chairs

Dr. Jay Rosenberger, Co-Chairs

Dr. Victoria Chen

Dr. Junzhou Huang

Sparse Representation and Learning for Discriminative EEG Source Imaging

by

Feng Liu, B.E., M.E.

DISSERTATION

Presented to the Faculty of the Graduate School of

The University of Texas at Arlington

in Partial Fulfillment

of the Requirements

for the Degree of

DOCTOR OF PHILOSOPHY

THE UNIVERSITY OF TEXAS AT ARLINGTON

May 2018

Dedicated to my family and my coming daughter.

Acknowledgments

I would like to thanks my advisors Dr. Shouyi Wang and Dr. Jay Rosenberger for their tremendous efforts and patience on training me, constantly motivating and encouraging me. I can not imagine what I can achieve without their valuable guidance and the supports throughout the journey of my Ph.D. study. Dr. Wang introduced me to this exhilarating research topic and guided me with his tremendous knowledge in data mining, machine learning, and brain science. His extensive and intensive knowledge, strong mentality and easy-going personality make he be an ideal advisor to work with. He also cares about my career development and gives me very valuable advices. Dr. Rosenberger guided me with his unmatched expertise in operations research and optimization knowledge. Dr. Rosenberger can always suggest good insight into my research, encouraged me to think independently, and he motivates me to work harder and do better research. It has been my great honor to work with both of them.

Heartfelt thanks also give to Dr. Victoria Chen who is always available addressing my questions and concerns, her intelligence, broad knowledge, fantastic communication skills, dedication to teaching and research as well as deep understanding how things work set an example to me to become better on different aspects. She is always there helping students in IE department. I am amazed how much energy she had when I figured out how many hours she put on her work every week, and she read carefully on every sentence for all the students' project reports in her class. Dr. Junzhou Huang

v

Sparse Representation and Learning for Discriminative EEG Source Imaging

Publication No. _____

Feng Liu, for Ph.D.

The University of Texas at Arlington, 2018

Supervisors: Shouyi Wang
                       Jay Rosenberger

As a direct measurement modality of neural electrical firing patterns, electroencephalogram (EEG) has a much higher temporal resolution up to millisecond compared to positron emission topography (PET) and functional magnetic resonance imaging (fMRI) and it has become one of the popular neuroimaging tools to find signatures of brain diseases and to understand how the brain works. Other advantages of EEG include low cost, easy portability, and non-invasive. However, a limitation of EEG is its low spatial resolution since the measurement is on the scalp rather than inside the brain. Given the recorded scalp EEG data, to reconstruct the activated brain sources signal inside the brain is known as EEG inverse problem or EEG source imaging (ESI). ESI technique has been widely used in the study of language mechanisms, cognition process, sensory function, as well as the localization of epileptic seizure, etc. However, due to the existing strong spontaneous background source activations, traditional ESI methods will inevitably incur the spurious activation patterns that are not task-related.

In this dissertation, we proposed the idea of discriminative ESI which aims to find the task-related sources and reduce the contamination from high background noises or spurious sources and reformulated the traditional ESI problem by using label information. Discriminative source activation pattern corresponding to different cognitive tasks provides more insights compared to the activation pattern reconstructed from traditional methods. To discover discriminative ESI, label information was integrated to the traditional ESI problem, and several frameworks have been proposed: (1) A sparse dictionary learning framework was proposed and a revised version of discriminative K-SVD (DK-SVD) algorithm is given to solve the formulated supervised dictionary learning problem. As the proposed learning framework incorporated the EEG label information of different brain status, it is capable of learning a sparse representation that reveals the most discriminative brain activity sources among different brain states. (2) A graph regularized ESI model, which implicitly use label information in the graph regularization term to promote in-class consistency and out-class discrimination, an efficient algorithm called feature sign search is used to optimize the proposed model. (3) As ESI solution always favors spatially smooth activation pattern instead of isolated discrete activations, we included first-order total variation (TV) and spatial graph Fractional Order Total Variation (gFOTV) with ADMM algorithm and practical technique to find a better spatially smoothing source activations. (4) Traditional ESI methods usually do not distinguish the task-related and spurious non-task-related sources that jointly generate EEG signal, which will inevitably yield misleading reconstructed activation patterns. We proposed to infer the true task-related EEG sources location by exploiting its low-rank property. To find a source activation pattern with low-rank structure, a novel ESI

viii

model based on low-rank representation was developed. Simulation results illustrate the effectiveness of those several proposed methods under different Signal Noise Ratio (SNR) and a variant of source configuration settings.

Table of Contents

xi

List of Tables

List of Figures

xvi

xvii

xviii

Chapter 1

Introduction

1.1 Introduction to EEG Source Imaging

The development of neuroimaging technology and intelligent algorithms contribute significantly to a better understanding of brain functionality and brain structure via analyzing bio-electrical brain signals. Neuroimaging technique plays an integral role in neurodegenerative disease diagnosis and intelligent surgical planning [42].

To study the brain, different brain modality data are recorded including electroencephalography (EEG) and magneto-encephalopathy (MEG), positron emission tomography (PET), and more recently functional near infra-red (fNIR) spectroscopy. Due to its low cost, easy portability, high temporal resolution and no exposure to radioligands, EEG has become one of the most popular brain imaging tools. Compared to other techniques such as PET and functional magnetic resonance imaging (fMRI), EEG is a direct measurement of real-time electrical neural activities, and EEG is more suitable to answer exactly *when* different brain modules are activated and hence in what processing steps each module is involved [64]. PET and fMRI cannot be used to assess rapidly varying neuronal activity due to the slow response of metabolism [35]. In this dissertation, we focus on techniques for EEG signal analysis. Successful applications of EEG can be found in several clinical environments, such as real-time monitoring of

patients' sleep apnea [73], detection and prediction of epilepsy seizures [18] [91] [80].

The electrical potentials measured by EEG electrodes originates from secondary ohmic current propagation from the tissues with primary intracellular currents [42]. It has been previously estimated that if as few as one in a thousand synapses become activated simultaneously in a region of about 40 mm^2 of cortex, the generated signal can be detected and recorded by EEG electrodes. However, the EEG electrodes measure electrical activities on the scalp surface instead of directly measuring the active neurons in the brain; it doesn't provide conclusive locations and distributions of the related activated sources. The problem of inferring the brain source from the recorded EEG is termed as *EEG inverse problem*, EEG Source localization or EEG Source Imaging (ESI). In this dissertation, we use the expression ESI, EEG inverse problem, source localization interchangeably. By solving EEG inverse problem, we can better understand how our brain is functioning under different cognitive tasks, and the discovery of underlying reason that caused brain functionality impairment as suffered by patients with neurological disorders such as Parkinson's disease, epilepsy, schizophrenia, depression and Alzheimer's diseases. Precise localization of activated sources inside the brain can also offer an insightful awareness of the responsible cortex regions that collaborated to perform certain cognitive tasks. The relationship between EEG forward and EEG inverse problem is given Fig.1.1. For the forward problem, source activation pattern is assumed to be known. The source signal propagates to the EEG electrodes via a conductivity matrix or lead field matrix calculated through a pipeline described in [2]. For the inverse problem, we want to infer the activation pattern in the brain given the EEG data and lead field matrix, which is a more realistic problem compared to the for-
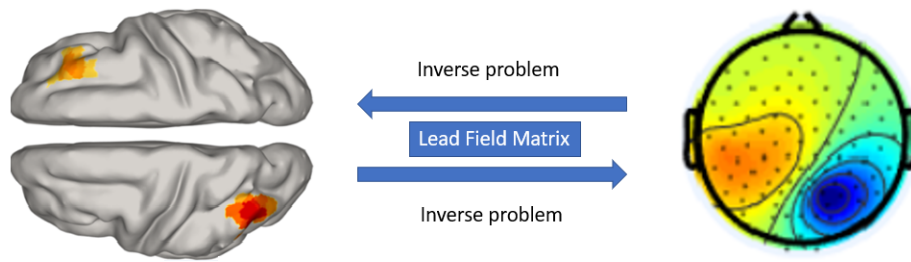
Figure 1.1: Illustration of forward and inverse problem.

ward problem. As a result, the inverse problem has been a hot topic among biomedical imaging and computational neuroscience community.

1.2 Literature Review

Since the number of electrodes usually outnumbers that of brain sources, the ESI problem is highly ill-posed or mathematically underdetermined. A variety of methods have been proposed to address this challenging problem with different neurophysiological assumptions, formulated by various regularization techniques [29, 64]. There are two main types of inverse solvers for ESI: *equivalent dipole fitting* and *distributed source imaging* [69]. Dipole fitting empirically solves the MEG/EEG forward and inverse problems by characterizing a few equivalent current dipoles of unknown locations which are responsible for electrical potential detected on the scalp sensors [44, 64]. Although dipole fitting gives a good estimate when the number of estimated sources are small, it is difficult to determine in advance the number of dipoles to explain very complicated neural activations. The algorithms proposed in recent years to solve the ESI problem within distributed dipoles paradigm can be further summarized into three

categories in general, which are the (1) Bayesian framework [8, 11, 19, 20, 56, 87], (2) state-space based algorithms [9, 43, 92, 96], (3) models using sparse representation technique [26, 28, 35, 69, 81, 83, 101].

In many sensory or cognitive studies, the underlying activated cortical responsible for the signal processing are relatively focal and thus sparse, which makes the sparse representation models being extremely successful in brain signal reconstruction [6, 13]. For the ESI problem, one widely accepted assumption is that a sparse spatial structure is favored than a complicated source configuration to explain the same data [16]. A representative early pioneering work is the ℓ_2-norm based minimum norm estimate (MNE) inverse solver [31]. Based on MNE algorithm, Pascual-Marqui et al. later proposed standardized low-resolution brain electromagnetic tomography (sLORETA) [71] that enforces spatial smoothness of the neighboring sources and normalizes the solution concerning the estimated noise level. Some algorithms proposed to use combined multiple solvers, e.g., Weighted minimum norm-LORETA (WMN-LORETA) which combines the LORETA solver and a weighted minimum norm to compensate for deeper sources originate from the subcortical regions [82]. As the above-mentioned algorithms are based on ℓ_2-norm to different extents, the estimated source area is over-diffuse. By replacing ℓ_2-norm by ℓ_1-norm, minimum current estimate (MCE) [85] is proposed to overcome overestimation of active area sizes incurred by ℓ_2-norm. Recent development of compressive sensing algorithm proved the ℓ_p $(p \leq 1)$ regularization on the original source signal usually provides a set of discrete sources distributed across the cortex due to high coherence of lead field matrix, in order to encourage reconstruction of extended source patches, it has been found that by enforcing sparsity in a transformed domain,

4

e.g., total variation (TV) regularization [22, 47, 75, 81], focal source extents can be better estimated.

The aforementioned algorithms estimate source location at each time point independently, leading to discrepancy along the time direction. To encourage temporal smoothness, a number of regularization techniques based on spatiotemporal mixed norms have been developed, including the famous Mixed Norm Estimates (MxNE) which uses $\ell_{1,2}$-norm regularization [26], and time-frequency mixed-norm estimate (TF-MxNE) which uses structured sparse priors in time-frequency domain for better estimation of the non-stationary and transient source signal [28].

1.3   Scientific Proposal

In this section, we make four new proposals to solve the ESI problem from a different perspective, regarding problem formulation or assumptions on source structure.

- **Proposal 1:** As is summarized in the literature review section, different algorithms solving the inverse problem were proposed, implemented and validated. However, to the best of our knowledge, there is no literature addressing simultaneously estimation of brain sources and distinguishing different sources given different states of the brain. We propose to use label information in the inverse problem and develop efficient algorithms to solve it. The new formulation is composed of two ingredients, source reconstruction, and supervised source classification. The contributions of this proposal are fourfold, including: (1) First

proposed a model with the discriminative power to solve EEG inverse problem. (2) First described the EEG inverse problem as an overcomplete dictionary learning problem and show the opportunities of using algorithms from compressive sensing and computer vision community. (3) The proposed revised version of K-SVD algorithm to solve the optimization model good accuracy. (4) Employed the most recently developed highly accurate head model rather than approximated.

- **Proposal 2:** As EEG data is highly non-stationary, and task-related sources also exhibit time-variant patterns. Thus the EEG inverse solver should also retrieve consistent patterns within each class. To explicitly extract factual sources and promote the in-class consistency and out-class discrimination, we implemented the graph regularized version of discriminative source reconstruction, tested on simulated EEG data, and showed its effectiveness in finding the discriminative sources and precise localization of the task-related sources. The contributions of this proposal are listed as follows: (1) A graph regularized EEG inverse model is presented that can promote in-class consistency and out-class discrimination. (2) A Voting Orthogonal Matching Pursuit algorithm is given to decompose the common sources.

- **Proposal 3:** We propose a novel EEG source imaging model in transformed domain based on a temporal graph structure by exploiting label information of brain state. In particular, both a first order TV n and graph fractional-order TV are proposed to seek spatial smoothness. The proposed spatiotemporal graph regularized model is solved by applying the alternating direction method of multipliers

(ADMM). Numerical experiments are conducted to verify the effectiveness of the proposed work on discovering is discriminative source extents. The contribution of our paper is summarized as follows: (1) We proposed a novel EEG source imaging model to promote spatial smoothness and intra-class consistency. (2) We derived the ADMM procedure to solve our model, and an enhanced framework based on the derived ADMM procedure is given to address the limitation of the standard ADMM procedure and achieved better performance. (3) We use a common source extents to represents the spontaneous activation and a discriminative source patch to represent the task-related activation pattern to make the simulation more realistic which is seldom explored in the literature.

- **Proposal 4:** One common drawback of the existing ESI algorithms is that they only consider noises on the sensor level and ignore the spurious noise from the cortex. If perfectly reconstructed, the estimated source is aggregated by task-related source and spurious noise in the source space. The true task-related sources will be corrupted by spurious sources, which motivates us to develop new algorithms to find the true task-related source. There are two commonly accepted assumptions (1) spatially sparse (2) temporally continuous for the task-related source activation pattern, which inevitably leads to the low-rank property of the source space. To better discover the task-related source, we impose the low-rank term in the goal function as we consider it is a more direct constraint for spatial sparse. We use a more direct penalty term for temporal smoothness, which is to penalize dissimilarity of temporally neighboring samples based on manifold graph embedding. It is worth noting that we used the graph regularization term

in our previous paper, however the graph is defined to be fully connected among all the points within one class [50], which inevitably drive all the activate patterns at different time points having the same magnitude, thus making the previously defined graph regularization term rely on a strong assumption and limit its future application for realistic cases.

We propose a novel EEG source imaging model based on temporal graph regularized low-rank representation. The model is solved based on the alternating direction method of multipliers (ADMM) [12]. We conducted extensive numerical experiments to verify the effectiveness of discovering task related low-rank sources. The reconstructed solution is temporally smooth and spatially sparse. The graph regularization can help to eliminate the spurious source and rectify bad estimations based on temporally neighbored reconstruction results. The contributions of our paper are summarized as follows: (1) We propose to consider the noise not only at the sensor level but also in the source space. (2) A low-rank representation model (LRR) is proposed for the first time on EEG inverse problem inspired by the low-rank property of true task-related source configurations. (3) We redefined graph embedding regularization based on our previous paper that utilizes temporal vicinity information of samples to promote temporal smoothness. (4) An algorithm based on ADMM is given which is efficient extracting the low-rank task-related source patterns.

Chapter 2

Fundamentals

2.1 Brain conductivity model

Brain conductivity model quantifies the amount of electrical signal received from EEG electrodes from the source signal. The brain conductivity model can also be called lead field matrix, forward model in ESI literatures.

A simplified brain model assumes spherical shape for three layers of head tissue with assumption of isotropic and homogeneous conductivities. However a three-layer spherical model oversimplified the realistic shape and tissue distribution of the head. Thus a Boundary element method (BEM) calculated brain model after mesh generation and tissue segmentation is more realistic and preferred in ESI study. Figure 2.1 gives one example of the head model containing 5 types of tissues, i.e. the scalp, skull, grey tissue, white tissue and Cerebrospinal fluid (CSF), which are segmented from the MRI DICOM format and tessellated into triangular meshes.

There are many software packages available to calculate the head model include Fieldtrip [68], OpenMEEG [27], SPM [25], SCIrun [70] and Brainstorm [84]. They are based on different programming languages including Matlab, Python, C etc. An illustration of tissue segmentation and mesh generation for a head using SCIRun [70] is given in Fig.2.1. The location of electrodes and all the voxels in the cortex are co-

9
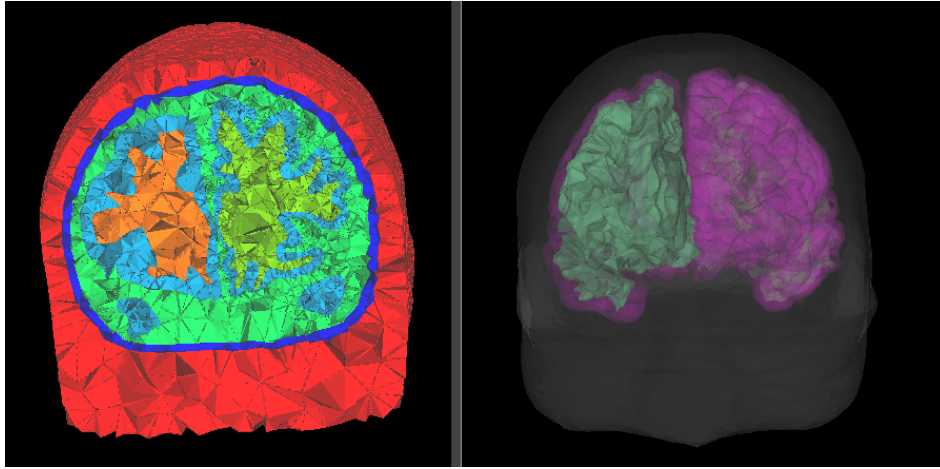
Figure 2.1: Illustration of tissue segmentation and mesh generation using FEM

registered and a lead field matrix can be calculated, a realistic brain model registered with EEG electrodes are illustrated in Fig.2.2 generated using the code from [1]. Each brain source is represented by a triangle.

2.2 Forward Model, Inverse Model and Regularizations

In this section, we first talk about the forward problem and then the inverse problem, and why we use regularization technique to solve EEG inverse problem.

2.2.1 Forward Model

The collective interaction from neurons with electrical activity induced by the flow of changed ions across membranes give rises to potentials that can be measured by EEG electrodes. Under the quasi-static approximation of Maxwell's equations, the measured EEG signal X can be described as the following linear function of current
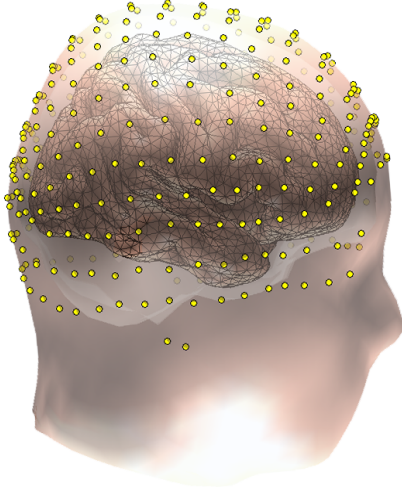
Figure 2.2: Triangle meshed realistic brain model. Each triangular element represents a current dipole located at its center and the orientation of dipoles is assume to be perpendicular to the cortical surface.

sources S,

$$X = LS + E, \tag{2.1}$$

where $X \in \mathbb{R}^{N_c \times N_t}$ is the EEG data measured at a set of N_c electrodes for N_t time points, $L \in \mathbb{R}^{N_c \times N_s}$ is the lead field matrix which maps the brain source signal to sensors on the scalp, each column of L represents the activation pattern of a particular source to the EEG electrodes. Fig.2.2 gives an exemplary brain model, the cortex is represented with triangle meshes, each triangle represents a brain voxel. In this dissertation, we use brain model and lead field matrix interchangeably. Also we use brain voxel, source, dipole interchangeably, sometimes with triangle as well. The number of triangles is equal to N_s. $S \in \mathbb{R}^{N_s \times N_t}$ represents the corresponding electrical potentials in N_s source locations for all the N_t time points. $E \in \mathbb{R}^{N_c \times N_t}$ is additive noise signal.
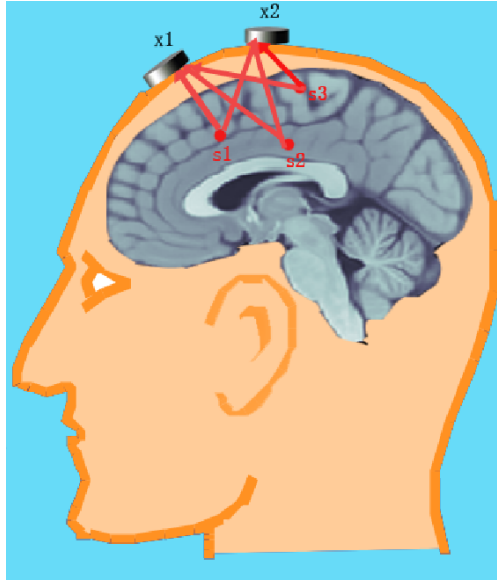
Figure 2.3: Illustration of brain sources propagate to EEG electrodes.

2.2.2 Inverse Model

According to Hadamard, a problem is well-posed if

1. there exists a solution to the problem (existence).

2. there is only one solution to the problem (uniqueness).

3. the solution depends continously on the parameters (stability).

A problem is ill-posed if it's not well-posed. Contrary to forward problem which is to find EEG data if given the mapping operator L and the source matrix S, the inverse problem is to infer the source signal given the EEG data, which is highly ill-posed. The inverse model is written as:

$$S = \arg \min_{S} \|X - LS\|_F^2, \tag{2.2}$$

12

As L is a matrix with number of columns far much greater than number of rows, the inverse problem becomes ill-posed. There are infinite number of solutions.

2.2.3 Regularization

To seek an unique solution, a regularization term has to be adopted. An estimate of S can be found by minimizing the following cost function, which is composed of a data fidelity term and a regularization term:

$$\arg\min_{S} \|X - LS\|_F^2 + \lambda\Theta(S). \tag{2.3}$$

The regularization term $\Theta(S)$ is to discourage complicated source configurations temporally or spatially and enforces neurophysiologically plausible solutions, and $\|\cdot\|_F$ is the Frobenius Norm. The regularization term take the form of ℓ_2, ℓ_1 or mixed norm [26] [83], spatially smooth formulation such as in LORETA algorithm or spatial total variation formulation in a transformed domain [22]. The earliest version of regularization is based on minimum energy of source signal using ℓ_2 norm, known as minimum norm estimation [31]. To promote sparsity, one of the best intuitive formulations is to use ℓ_0-norm to restrict the total number of activated sources less than a scalar k, the following formulation can be used:

$$\arg\min_{S} \|X - LS\|_F^2 \ \ s.t. \ \|s_i\|_0 \leqslant k, \tag{2.4}$$

As ℓ_0-norm constrained problem is NP-hard, to avoid the NP-hard problem, approximating ℓ_0 with ℓ_1-norm is a common practice. Donoho suggested that ℓ_1 and ℓ_0 norm are equivelant under certain conditions [23]. The ℓ_1-norm regularized formulation is

described as

$$s_i = s^*(x_i, L) = \arg\min_{s_i} \|x_i - Ls_i\|_2^2 + \gamma\|s_i\|_1. \tag{2.5}$$

The ill-posed problem of Eq.2.2 arises from the fact that the L is an wide matrix, and the number of columns is greater than number of rows. From a linear system perspective, the dimension of observed output is less than that of input signal, making inferring s_i from x_i an under-determined problem with infinite solutions if no regularization term is applied. Given the EEG recordings at a time point, which is denoted as ith column x_i of X matrix, we want to represent the signal with minimum error by trying to find the best linear representation from activation patterns (atoms) in the overcomplete dictionary L. The solution s_i is the sparse coding for the x_i in the dictionary L, the non-zero entries in s_i represent the activated regions inside the brain.

2.3 Optimization Algorithms

Based on different ESI problem formulations, the solutions can be iterative algorithm or closed form one. We list several models and the corresponding optimization algorithms.

2.3.1 Minimum Norm Estimate (MNE)

The expression for MNE is given as:

$$\min_s \|s\|_2^2 \quad \text{subject to} \quad x = Ls. \tag{2.6}$$

The solution for the MNE is $\hat{s} = L^T(LL^T)^{-1}x$. The MNE solution prefers superficial sources and usually omit deeper sources. To rectify for this biased preference, a subse-

quent modification for the MNE algorithm is called weighted minimum norm estimate (WMNE), which is formulated as:

$$\min_{s}\|Ws\|_2^2 \quad \text{subject to} \quad x = Ls, \tag{2.7}$$

where W is a diagonal matrix with $w_{ii} = (\|L_i\|)_2^2$ with L_i being the i-th column of L. The corresponding solution is $\hat{s} = WW^T L^T (LWW^T L^T)^{-1} x$.

2.3.2 LORETA

LOw Resolution Electromagnetic Tomography (LORETA) is a widely used approach for ESI problem. LORETA further includes spatial smooth prior based on WMNE formulation by defining a Laplace operator B for smoothness regularization, the LORETA is trying to solve the formulation below:

$$\min_{s}\|BWs\|_2^2 \quad \text{subject to} \quad x = Ls. \tag{2.8}$$

Here W is similarly defined as WMNE formulation to correct the bias of MNE towards superficial sources. The solution of LORETA algorithm is

$$\hat{s} = (WB^T BW)^{-1} L^T \left[L(WB^T BW)^{-1} L^T \right]^\dagger,$$

where $\dagger$ denotes Moore-Penrose pseudo-inverse.

2.3.3 Augmented Lagrangian Multiplier Method

The general formulation of an optimization problem is an objective function subject to some constraints. The ESI problem can be generalized into the following form:

$$\min_{x \in R^n} f(x) \quad \text{subject to} \quad g(x) = 0, \tag{2.9}$$

15

where $f(x)$ is the objective function, and $g(x)$ is constraints. Without loss of generation, $g(x) \in R^k$ To solve Eq.2.9, the method of Lagrange multipliers is commonly. By introducing a new variable μ, the Lagrangian function is defined as

$$L(x, \mu) = f(x) + \langle \mu, g(x) \rangle. \tag{2.10}$$

Usually, we use an augmented Lagrangian multiplier method by incorporating an additional quadratic penalty term of the constraints, to make the dual ascent more robust. The augmented Lagrangian formulation at the k-th iteration is

$$L_k(x, \mu) = f(x) + \langle \mu, g(x) \rangle + \frac{\lambda}{2} \|g(x)\|_2^2 \tag{2.11}$$

We update the solution x and the multiplier alternatively as follows

$$\begin{cases} x^k = \operatorname{argmin} L_k(x, \mu^{k-1}) \\ \mu^k = \mu^{k-1} + \lambda g(x^k) \end{cases} \tag{2.12}$$

If the goal function can be decomposed into two parts, and the original update on x^k in Eq. 2.12 is difficult to calculate. Support $f(x) = f_1(x) + f_2(x)$, and $\operatorname{argmin}_x f(x)$ is hard to calculate and both the solution to minimization of $f_1(x)$ and $f_2(x)$ has a close form solution or approximate solution. The original problem can be reformulated as

$$\min_{x \in R^n} f_1(x) + f_2(y) \quad \text{subject to} \quad g(x) = 0, y = x. \tag{2.13}$$

Write those two constraints $g(x) = 0, y = x$ as $\tilde{g}(x, y) = 0$. The augmented Lagrangian formulation at the k-th iteration is

$$L_k(x, y, \mu) = f_1(x) + f_2(y) + \langle \mu, \tilde{g}(x, y) \rangle + \frac{\lambda}{2} \|\tilde{g}(x, y)\|_2^2 \tag{2.14}$$

We update the solution x, y and the multiplier alternatively as follows

$$\begin{cases} x^k = \operatorname{argmin} L_k(x, y^{k-1}, \mu^{k-1}) \\ y^k = \operatorname{argmin} L_k(x^k, y, \mu^{k-1}) \\ \mu^k = \mu^{k-1} + \lambda \tilde{g}(x^k, y^k) \end{cases} \qquad (2.15)$$

The above Gauss-Seide way of updating the variable and Lagrangian multipliers falls into the framework of Alternating Direction Method of Multipliers (ADMM).

Chapter 3

Sparse Dictionary Learning for Supervised EEG Source Imaging

3.1 Introduction

Per the discussion in literature review section, based on different assumptions, different algorithms solving the inverse problem were proposed, implemented and validated. Due to the existing strong spontaneous background source activations, discriminative source activation pattern corresponding to different cognitive tasks which provide more insights shall be reconstructed but with few studies. To the best of our knowledge, there is no literature addressing simultaneously estimation of brain sources and distinguishing different sources given different states of the brain. In this chapter, we propose a new supervised formulation of the inverse problem and with efficient algorithms to solve it. The new formulation is composed of two ingredients, source reconstruction and supervised source classification. The contributions of this chapter is fourfold, including:

1. First proposed the idea of combining traditional EEG Source Imaging (ESI) problem and classification problem and solve them in a joint framework to find task-related discriminative patterns rather than find the overall activation patterns with spontaneous brain activations.

2. Reformulated the EEG inverse problem as a sparse dictionary learning problem and show the opportunities of using algorithms from compressive sensing and computer vision community.

3. Proposed revised version of DK-SVD algorithm to solve the optimization model good accuracy.

4. Employed the most recently developed highly accurate head model rather than approximated head model compared to previous studies.

The structure of the rest chapter is as follows: In Section 2, the problem formulation is given. In Section 3, the optimization method is proposed. In Section 4, the numerical experiments and the effectiveness of our proposed framework, conclusions are given in Section 5.

3.2 Discriminative Source Reconstruction

In this section, we first briefly review the inverse problem, and then the proposed model in the form of discriminative dictionary learning is described, which comprises the source reconstruction term and label guided discriminative term. The motivation of such a discriminative inverse model will be discussed in details.

3.2.1 The Inverse Problem

Generally, an estimate of S can be found by minimizing the following cost function, which is composed of a quadratic error and a regularization term:

$$\arg\min_{S} \|X - LS\|_F^2 + \lambda\Theta(S) \tag{3.1}$$

The penalty function $\Theta(S)$ is to discourage unnecessary complicated source configurations and enforces neurophysiologically plausible solutions, and $\|\cdot\|_F$ is the Frobenius Norm. The regularization term takes the form of ℓ_2, ℓ_1 or mixed norm, spatially smooth formulation as in LORETA estimation or spatially sparse formulation with least absolute shrinkage and selection operator estimate.

3.2.2 Extract Discriminative Sources with Label Information

As the brain has different emotion/task related states, classification of different status is important in Brain-Computer Interface(BCI) application, also it helps us understand the mechanism how the brain is functioning. Mapping the EEG to the source gives us a direct sense of how the sources are evoked and evolved in different states. The motivation of the supervised inverse problem formulation can be explained using a simple demonstrative example as it is illustrated in Fig.3.1. The electrical potential mentioned at x_1 can be formulated as $x_1 = a_1 s_1 + a_2 s_2 + a_3 s_3 + \epsilon$ and the same case for x_2 channels, where $a_i (i = 1, 2, 3)$ describe the conductivity from for electricity traveling from site s_i to channel x_1. According to previous studies [76], only a small portion of electrical energy are task related and it's reasonable to assume that s_1 represents to the non-task resting state source and contribute most of the potential measured in sensors. Assume s_2 is activated when performing task A and s_3 is related to task B. Under the condition of low signal noise ratio (SNR), the reconstructed source tends to be only s_1 without explicitly using the supervising label. Here we leverage the label information explicitly in the hope of successful reconstruction of the discriminative source s_2 and s_3. Here we present a new framework that can infer the source signal guided by the
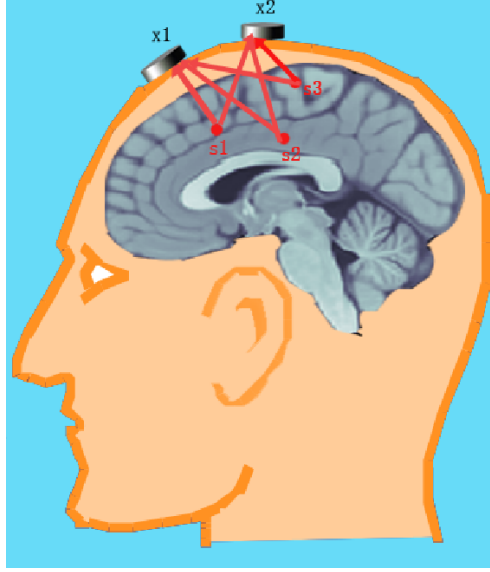
Figure 3.1: Cortex source signal propagate to EEG electrodes. Both discriminative sources (s_2, s_3)and common sources (s_1) contribute to EEG data.

label information. A classification of different brain status based on the sparse coder s_i is obtained by determining its model parameters W, where

$$W = \arg\min_W \sum_i \ell\{h_i, f(s_i, W)\} + \lambda \|W\|_F^2 \qquad (3.2)$$

where $\ell\{\cdot\}$ is the loss function for classification accuracy based on the ground truth and classification model $f(\cdot)$, and h_i is the label vector where non-zero entry denotes the corresponding class. Traditional procedure solves the pure inverse problem ignoring the supervising label and then train the sparse coding s_i with classification model. Separating the inverse problem and classification problem can be misleading, we argue that since we have the brain status information, it's better to use it as a label to make the inverse solution exhibiting discriminative capability. With this thought and inspired by literature in computer vision community [41, 74, 95, 99], the following

21

sparse discriminant inverse model is given:

$$\langle W, S \rangle = \arg\min_{W,S} \|X - LS\|_F^2 + \beta \sum_i \ell\{h_i, f(s_i, W)\}$$
$$+ \lambda \|W\|_F^2 \, s.t. \, \forall i, \quad \|s_i\|_0 \leqslant T \tag{3.3}$$

The first term is the reconstruction error; the second term represents the classification loss, the third term is the regularization of W to avoid over-fitting. This formulation aims to simultaneously learn the sparse coding and the classification model. Using the multi-class classifier $f(\cdot)$ instead of one-against-all classifiers is efficient for classification, by suppressing features sharing among classes and trying to explicitly extract different sparse representation among different classes. In this paper, We focus on an inverse solution with more balanced reconstructive and discriminative power by adding the classification regularization term λ. A summary of our proposed framework is illustrated in Fig.3.2. In Fig.3.2 The left two topoplots represent the recorded EEG potentials on the scalp for two stimulus status (e.g. finger tapping and comedy video stimulus), and the lead field matrix is represented as overcomplete dictionary, the sparse coefficients are the codes for the source activation location and activation potentials; The sparse coefficients and W matrix are estimated simultaneously. Each row of the W matrix is termed as the discriminative filter because the Hadamard product of the source code coefficient and the discriminative filter can highlight the corresponding stimulus activated source signal by masking the common background or resting activation signals which are share by other different brain stimulus inputs. The rightmost pictures are exemplary reconstructed discriminative source activation patterns on the cortex.
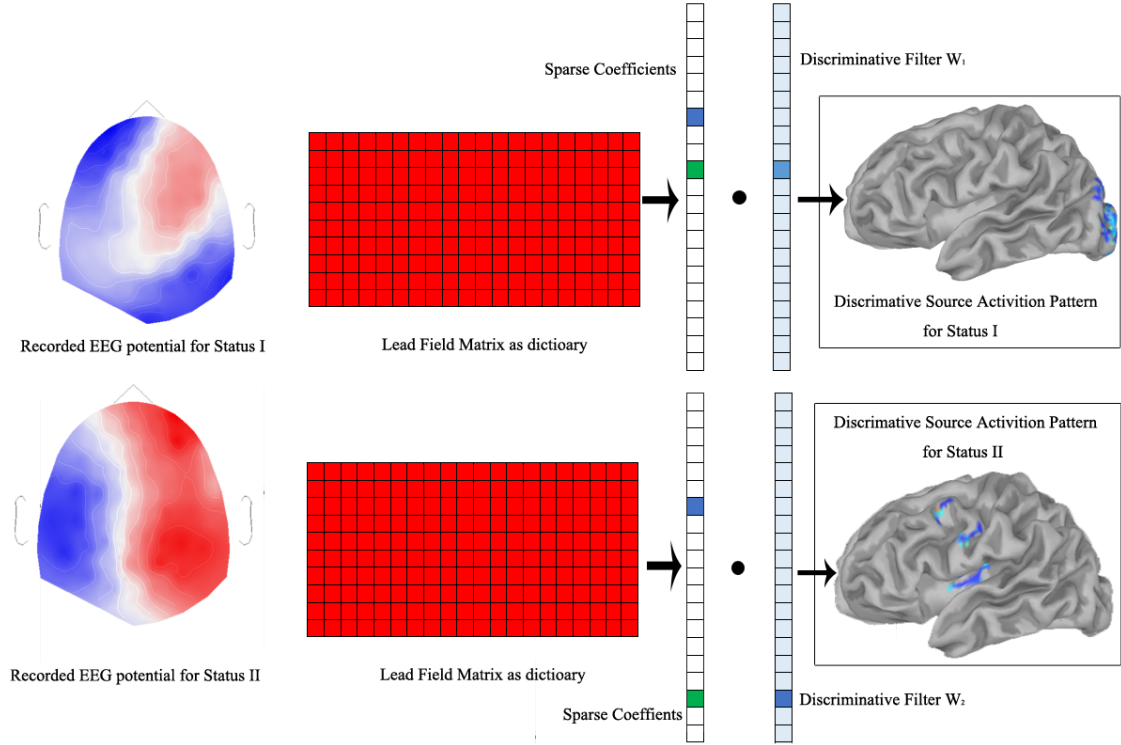
Figure 3.2: Discriminative Source Reconstruction Framework.

3.2.3 Source Reconstruction Based on Linear Classifier

From Eqn.3.3, we reduce to the following optimization problem by using a simple linear classifier.

$$
\begin{aligned}
\langle W, S \rangle &= \arg\min_{W,S} \|X - LS\|_F^2 + \beta \|H - WS\|_F^2 \\
&\quad + \lambda \|W\|_F^2 \; s.t. \; \forall i, \quad \|s_i\|_0 \leqslant T
\end{aligned}
\tag{3.4}
$$

Here $H = [h_1, h_2, \ldots, h_N] \in \mathbb{R}^{m \times N_t}$, with each row h_i, $i = 1, \ldots, N_t$ being the label vector corresponding to an EEG signal x_i. In order to solve the optimization problem (3.4), the K-SVD algorithm and its derivatives can be used. However, our proposed

method is different from these previous methods in several aspects, owing to it being tailored to solve the EEG inverse problem.

3.3   Optimization with K-SVD Algorithm

For Equation 3.4, it can be rewritten as

$$\langle W, S \rangle = \arg\min_{W,S} \left\| \begin{pmatrix} X \\ \sqrt{\beta}H \end{pmatrix} - \begin{pmatrix} L \\ \sqrt{\beta}W \end{pmatrix} S \right\|_F^2 \tag{3.5}$$
$$+ \lambda \|W\|_F^2 \qquad s.t. \ \forall i, \ \|s_i\|_0 \leqslant T$$

Let $X_{new} = (X^t, \sqrt{\beta}W^t)^t$, $L_{new} = (L^t, \sqrt{\beta}W^t)^t$, the optimization of Equation 3.5 is equivalent to solving the following problem:

$$\langle L_{new}, S \rangle = \arg\min_{L_{new},S} \|X_{new} - L_{new}S\|_F^2$$
$$+ \lambda \|W\|_F^2 \qquad s.t. \ \forall i, \ \|s_i\|_0 \leqslant T \tag{3.6}$$

We use normalized lead field matrix L to meet the requirement of K-SVD algorithm. It's more important to find an explanatory activation pattern compared to magnitude of the signal as a common practice [33]. Later we show that the normalization doesn't effect the solution in case of ℓ_0 norm. The normalization is defined as:

$$L' = \{l'_1, l'_2, ..., l'_{N_d}\}$$
$$= \{\frac{l_1}{\|l_1\|_2}, \frac{l_2}{\|l_2\|_2}, ..., \frac{l_{N_d}}{\|l_{N_d}\|_2}\}$$
$$W' = \{w'_1, w'_2, ..., w'_{N_d}\} \tag{3.7}$$
$$= \{\frac{w_1}{\|l_1\|_2}, \frac{w_2}{\|l_2\|_2}, ..., \frac{w_{N_d}}{\|l_{N_d}\|_2}\}$$

Suppose x_i is the EEG signal vector and we want to find corresponding source location. x_i is a sparse linear combination of the atoms in L, which can be expressed as:

$$x_i = \sum_{m=1}^{N_d} l_m s_i(m) = \sum_{m=1}^{N_d} \left(\frac{l_m}{\|l_m\|_2} \right) (s_i(m)\|l_m\|_2)$$
$$= \sum_{m=1}^{N_d} l'_m s'_i(m)$$

Also, the Label matrix h_i can be expressed as

$$h_i = \sum_{m=1}^{N_d} w'_m s'_i(m) = \sum_{m=1}^{N_d} \left(\frac{w_m}{\|l_m\|_2} \right) (s_i(m)\|l_m\|_2)$$
$$= \sum_{m=1}^{N_d} w_m s_i(m)$$

The sparse coding with or without normalization of L is equivalent in terms of ℓ_0-norm, which is $\|s_i\|_0 = \|s'_i\|_0$, thus the normalization of lead field matrix doesn't effect the reconstruction solution under condition of ℓ_0-norm. As L_{new} is always normalized column-wise, we can drop the regularization penelty term $\|W\|_F$.

$$\langle L'_{new}, S \rangle = \arg \min_{L'_{new}, S} \|X_{new} - L'_{new} S\|_F^2$$
$$s.t. \; \forall i, \; \|s_i\|_0 \leqslant T \tag{3.8}$$

For similarity, we omit the apostrophe ($'$) notation when there is no confusion. When fixing S, solving L matrix can be regarded as solving a simple regression problem:

$$\hat{L} = \arg \min_L \|X - LS\|_F^2, \tag{3.9}$$

where $\hat{L} = XS^T(SS^T)^{-1}$. The computational complexity of $XS^T(SS^T)^{-1}$ is $O(n^3)$, it is advisable to solve it using K-SVD by updating the dictionary atom-by-atom. This optimization problem of Eqn.3.8 is exactly what K-SVD algorithm [3] solves and the only difference is that the upper L part of dictionary L_{new} will not be updated. We adopt the procedure in the original K-SVD algorithm.

Following K-SVD, denote l'_k as the kth column in the L'_{new}, and s_k is the corresponding kth row in S. The second term $L'_{new}S$ can be decomposed into the following formulation:

$$L_{new}S = \sum_{k=1}^{N_d} l_k * s_k$$

Let $E_k = (X - \sum_{j \neq k}(l_j * s_j))$, representing the error without using the atom l_k, the main idea of K-SVD is to update each atom in the dictionary sequentially to the projected direction that most reduces the error. Let $\tilde{s}_R^k$ and $\tilde{E}_k$ denote the result of discarding the zero entries in x_R^k and E_k, respectively. As a result, l_k and $\tilde{s}_R^k$ can be computed using

$$\left\langle l_k, \tilde{s}_R^k \right\rangle = \arg \min_{l_k, \tilde{s}_R^k} \left\| \tilde{E}_k - l_k \tilde{s}_R^k \right\|_F^2 \tag{3.10}$$

The above optimization problem can be easily solved by employing an SVD composition of $\tilde{E}_k$, namely, $U \Sigma V^t = SVD(\tilde{E}_k)$, and using the SVD result and update the l_k and $\tilde{s}_R^k$ with $l_k = U(:, 1)$, $\tilde{s}_R^k = \Sigma(1, 1)V(1, :)$. $U(:, 1)$ denotes the first column of matrix U, and $V(1, :)$ is the first row of V, $\Sigma(1, 1)$ is the first diagonal value of Σ. The upper part of the L_{new} matrix will not be updated, and only the lower part composed of W matrix is updated. The detailed algorithm is given in the following algorithm 1 with matlab indexing notation.

3.4 Numerical Experiments

In this section, we conducted numerical experiments comparing the proposed framework with the benchmark algorithms for ESI based on a realistic high accurate brain model. The benchmark algorithms include sLORETA [71], Minimum Norm Es-

---

Algorithm 1 Revised DK-SVD algorithm

INPUT: Lead field matrix L, preprocessed EEG signal matrix X, relative controlling scalar β, label matrix H

OUTPUT: classification matrix W, EEG source matrix S

Initialization: Using K-SVD initialization described in Ref. [3]

    set $m = 1$

    while not converged **do**

        Solve the following sparse coding problem using matching pursuit algorithm for $i = 1, 2, \ldots, N$:

$$\min_{s_i} \|x_i - Ls_i\|_2^2 \quad s.t. \quad \|s_i\|_0 \leqslant T$$

        while i is not equal to N_d **do**

            (1) Compute the representation error without atom l_i, $E_i = (X - \sum_{j \neq i}(l_j * s_j))$

        (2) Extract the nonzero entries of s_i and truncate the E_i to E_i^P accordingly.

        (3) SVD decomposition for E_i^P as $E_i^P = U\Lambda V$

        (4) Update l_i and s_i^T:

            $l_i(N_c + 1 : end) \longleftarrow U(:, 1)(N_c + 1 : end)$,

            $\tilde{s}_R^i \longleftarrow \Sigma(1, 1)V(1, :)$.

        (5) Update index $i \longleftarrow i + 1$;

        end while

    $m \longleftarrow m + 1$

    end while

---

timate (MNE), Minimum Current Estimate (MCE), also known as ℓ_1 constrained formulation. All computations in this paper were conducted on a 64–bit windows 7 with i7-6700 CPU, the memory of 16 GB and frequency is 3.40 GHz.

3.4.1 Head Model

Head model is a volume conductor model which is used to describe the flow of electric current in the head. Usually, the brain model was built in 4 steps, (1) col-

lect the MRI images; (2) tissue segmentation (3) Mesh generation and assignment of conductivities for different tissues (4) Solve boundary element finite equations to get the lead field matrix. We used a newly developed lead field model called ICBM-NY or "New York Head" [39] which is based on highly detailed standardized finite element model (FEM) of the non-linear averaged anatomical template-ICBM152. The brain tissue segmentation is divided into six tissue type (scalp, skull, cerebrospinal fluid(CSF), gray matter, white matter and air cavities) with native MRI resolution of $0.5mm^3$. Also, we divided the brain into 8 regions of interests (ROI) [34] called Right Anterior Inferior (RAI), Right Anterior Superior (RAS), Right Posterior inferior (RPI), Right Posterior Superior (RPS), Left Anterior Inferior (LAI), Left Anterior Superior (LAS), Left Posterior inferior (LPI), Left Posterior Superior (LPS) to measure the distance between the reconstructed EEG source and the true source locations within each region. The "New York Head" model has two different precision levels, corresponding to 74382 and 2004 voxels respectively. The dimension of lead field matrix we are using is 108×2004, representing 108 channels and 2004 voxels. We also assume that source orientation is perpendicular to the cortex surface.

3.4.2 Experiment Setup

In the simulation experiments, we designed 1-3 common sources that are located in different ROIs with a higher magnitude and three discriminative sources related to three different brain states with smaller magnitude located at different ROIs. The common sources represent the spontaneous activation patterns in the brain. The each of the discriminative source is corresponding to one of three the brain states in the simulation.

28

Specifically, we designed the spontaneous sources with a magnitude of 0.6 with standard deviation to be 0.1 and task-related discriminative with a magnitude of 0.4 with a standard deviation of 0.05 located in different ROIs from the common sources.

We sampled 200 time points for each class and repeated 20 times the experiments under the same setting. The noise matrix is designed to affect the EEG recording together with the true source signal. For each time point, three random voxels are corrupted randomly with the average value being $\{0.2, 0.3, 0.4\}$ resulting in different SNR design. We define the SNR $= 10 \log_{10} \frac{P_s}{P_n}$, where P_s and P_n are the power of signal and noise respectively. We did experiments with common activation sources with different level, using 1,2,3 common sources, the test the performance of the discriminative source locations under different SNR.

3.4.3 Result

The discriminative source reconstruction performance of the proposed method, as well as the benchmark methods, are summarized in Table 3.1–3.3. In Table 3.1-3.3, computation time is recorded in seconds (s). The distance evaluation is based on the shortest path of two voxels on the cortex surface instead of direct Euclidean distance. The location of the largest source in the same ROI with the ground truth location is considered to be the reconstructed source. Unlike the previous way of measuring both the common source accuracy and discriminative source accuracy in previous paper [50], we only focus on the accuracy of the discriminative sources, and their location accuracy in the one of the 8 ROIs. As in the simulated data, we know the ground truth of discriminative sources, the location error is calculated with the ground truth of discriminative

29

source and the largest activated source in the same ROI. The distance was defined on the surface of an irregular mesh, calculated using shortest path algorithm. All of the values in Table 3.1-3.3 except the Time column in the table represents distance in (mm) from ground true source to the reconstructed source. The time column records the amount of time spent to calculate each time point to perform source reconstruction. EC1 represents localization Error for Class 1, which is the distance of the reconstructed discriminative source to the ground truth within the same ROI. EC2 and EC3 are similarly defined.

Table 3.1: Localization accuracy summary when number of common source is 1.

	SNR =4.5				SNR =1.5				SNR = -1			
Methods	Time	EC1	EC2	EC3	Time	EC1	EC2	EC3	Time	EC1	EC2	EC3
Homotopy	0.27	9.4	7.0	12.3	0.26	15.9	12.8	11.4	0.25	19.4	15.9	19.4
sLORETA	0.017	16.0	18.1	17.7	0.017	23.8	20.1	21.1	0.017	31.5	28.0	31.5
MNE	3.2e-5	20.2	22.0	22.5	2.6e-5	27.9	26.4	25.4	2.4e-5	32.8	30.0	32.8
Proposed	0.27	7.5	5.1	10.4	0.26	12.7	8.8	8.75	0.26	13.0	9.9	12.9

Table 3.2: Localization accuracy summary when number of common source is 2.

	SNR =5.4				SNR =2.0				SNR = 0.5			
Methods	Time	EC1	EC2	EC3	Time	EC1	EC2	EC3	Time	EC1	EC2	EC3
Homotopy	0.27	8.6	10.5	11.4	0.26	8.0	9.9	12.4	0.25	15.1	13.9	17.1
sLORETA	0.017	18.7	19.7	25.0	0.017	23.9	23.6	26.6	0.02	31.9	28.9	31.1
MNE	3e-5	20.8	24.3	27.8	2.5e-5	26.9	27.3	26.2	2.5e-5	29.5	27.1	30.7
Proposed	0.28	6.7	8.2	9.1	0.26	5.15	6.6	9.6	0.25	9.4	7.7	11.3

Table 3.3: Localization accuracy Summary when number of common source is 3.

	SNR =6.2				SNR =3.5				SNR = 0.35			
Methods	Time	EC1	EC2	EC3	Time	EC1	EC2	EC3	Time	EC1	EC2	EC3
Homotopy	0.21	3.9	6.5	9.1	0.21	5.8	7.1	7.3	0.2	12.6	12.8	13.1
sLORETA	0.013	29.1	28.7	28.6	0.013	27.1	25.2	24.4	0.01	30.3	27.8	30.8
MNE	5.7e-5	31.6	34.7	31.7	5.4e-5	25.3	27.7	21.8	4.8e-5	29.7	26.3	30.2
Proposed	0.21	2.3	5.12	6.8	0.21	2.1	3.1	3.6	0.2	6.7	6.6	7.4

We can see from Table (3.1-3.3) and the Fig.3.3–Fig.3.5 that our proposed method provide much high accuracy in locating the discriminative sources under all the

settings conducted in the experiment. The sLORETA algorithm and MCE and MNE give very diffuse solution and failed to estimate the exact location. When we increase the noise, our algorithm performs very robust compared to others. It is worth noting that in most of the cases, our algorithm can find a very good solution, however, in several cases, our algorithm failed to estimate the exact location due to the high coherence of the lead field matrix. As the traditional algorithm such as MNE ans sLORETA may find common sources due to they have larger magnitude, missing unanimously the discriminative source, meaning that the task related source can't be estimated correctly. As is shown in the boxplots, even though the mean value of the proposed algorithm is very small, still in some cases, our algorithm failed, and the exact locations on the cortex where the sources are difficult to reconstruct needs further exploration.
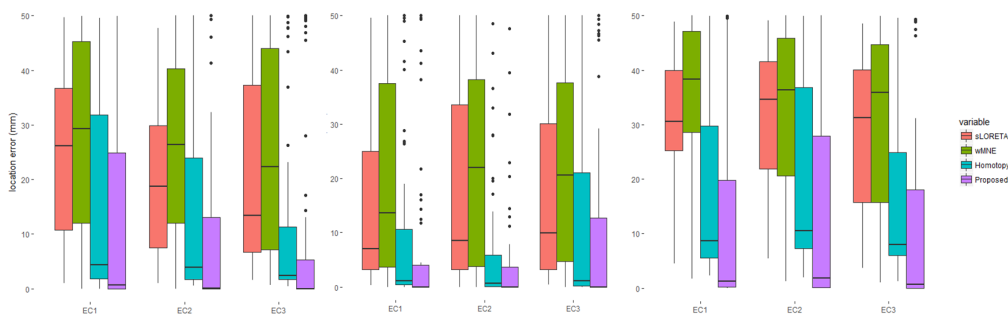
Figure 3.3: Boxplot of the error comparing different algorithms when there is 1 common source, from left to right when SNR equals 4.5, 1.5 and -1 respectively.

We also conducted a pairwise t-test comparing all the localization error of all algorithms, and the summary table for the is given below Table 3.4. According to t-test, all the comparison is significant, and sLORETA is slightly better than wMNE and the localization error from both sLORETA and wMNE are significant larger than
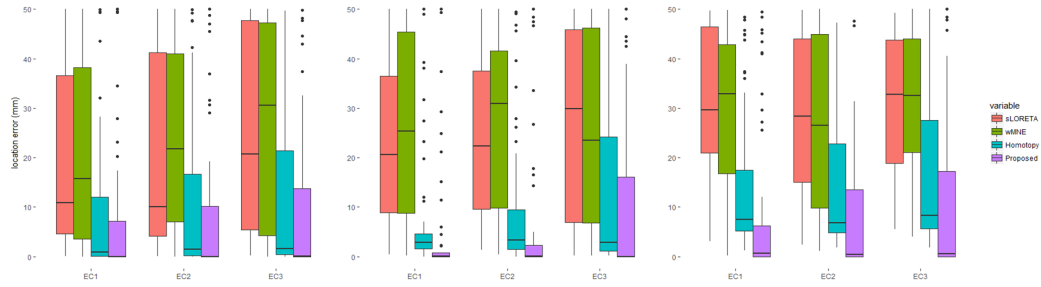
Figure 3.4: Boxplot of the error comparing different algorithms when there are 2 common sources, from left to right when SNR equals 5.4, 2.0 and 0.5 respectively.
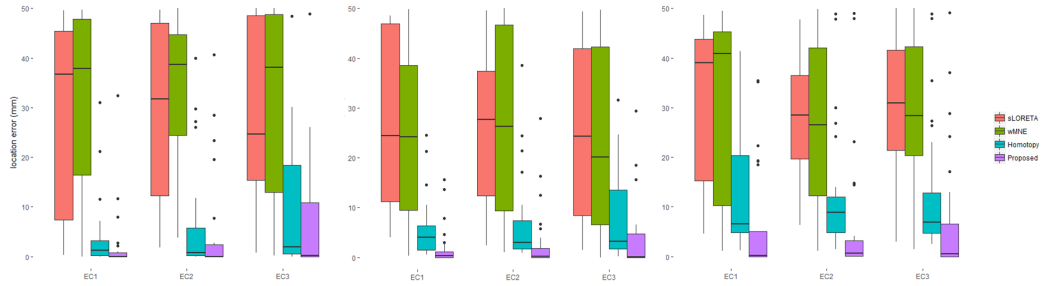
Figure 3.5: Boxplot of the error comparing different algorithms when there are 3 common sources, from left to right when SNR equals 6.2, 3.5 and 0.35 respectively.

Table 3.4: Localization error pairwise comparison using t-test

Comparison Test	mean	std	T-value	p-value
sLORETA - wMNE	-2.60	0.36	-7.28	<0.001
sLORETA - Homotopy	11.45	0.49	23.6	<0.001
sLORETA - Proposed	15.14	0.52	29.22	<0.001
wMNE - Homotopy	14.05	0.50	28.19	<0.001
wMNE - Proposed	17.74	0.52	34.03	<0.001
Homotopy - Proposed	3.69	0.12	31.57	<0.001

Homotopy and the proposed method. Our proposed algorithm has smaller localization error than the Homotopy, on average, we do 3.69 mm better than Homotopy and more than 10 mm better than sLORETA and wMNE. Although, we did not list Homotopy in our result, we compared Homotopy and FOCUSS algorithm, and they have similar result, but FOCUSS is much slower than Homotopy.

We also demonstrated an exemplary results in Fig.3.6 and Fig.3.7. Fig.3.6 demonstrates the reconstructed source and calculated discriminative filters W; the discriminative filters suppress common source shared by different status while extracting and magnifying distinguished ones. The common resting state signal is attenuated by W (as is illustrated in LAS region) and the reconstructed discriminative sources are extracted and magnified by the corresponding rows of W. The upper subfigure is the reconstructed source S and discriminative filter W is given in the lower subfigure. Fig.3.7 illustrates the EEG potentials topoplots on the scalp before and after the application of our method, distinctive source activation patterns can be revealed. We also give the exemplary plots of cortex from different algorithms. In fig.3.7, the top 3 topoplots are corresponding to 3 different brain tasks with the high common source of spontaneous activity or resting state potentials, it's very hard to distinguish them. Below is the topoplots after we applied our methodology to extract the discriminative expression for different brain tasks. The lower topoplots are constructed by applying the discriminative source to the forward model.

To illustrate the effect of the proposed algorithm, the ground truth of the activated pattern is given in Fig.3.8, with the reconstructed source estimated by MNE, sLORETA, Homotopy, and our method given in Fig.3.9–Fig.3.12. In Fig.3.8, Each row
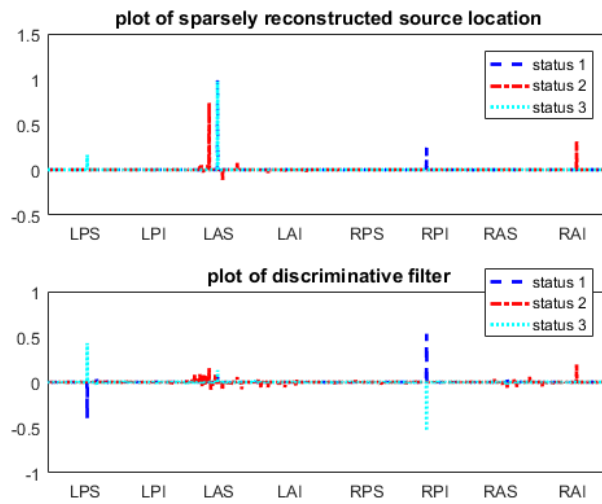
Figure 3.6: Sparse coding and discriminative filter for 3 different brain status.
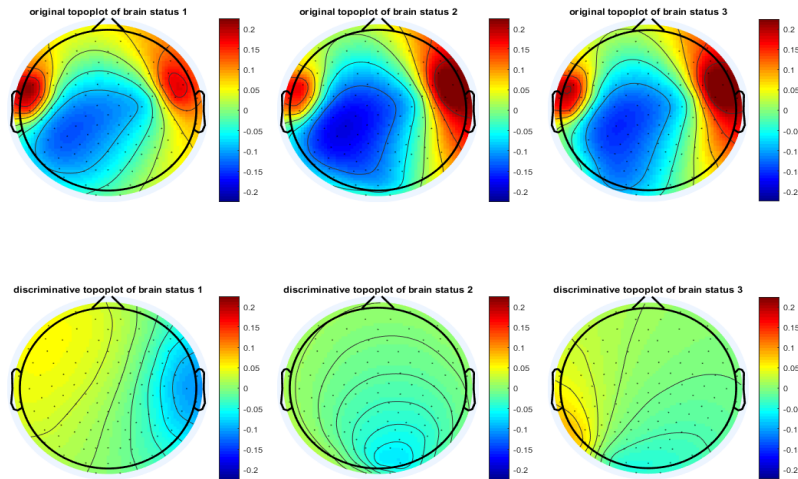
Figure 3.7: Discriminative filtered topoplots for 3 different brain status.

34

is a source activation pattern for each brain states. From left to right, are the left lateral view, right lateral view and superior view. There are two common sources shared by 3 brain states, which are circled in blue, and the discriminative source are specific to each class, which is circled in red. For the reconstructed EEG Source Imaging illustrated in Fig.3.9–Fig.3.12, each row is a source activation pattern for each brain states. From left to right, are the left lateral view, right lateral view and superior view. There are two common sources shared by three brain states, and the discriminative source is specific to each class. The sLORETA and MNE failed to find the discriminative sources, and MCE (Homotopy) can find the solution pretty well but with a lot of spurious sources so that reconstructed result can be misleading. Our filtered result is given in Fig.3.12, which illustrates the discriminative source particular to one brain state.
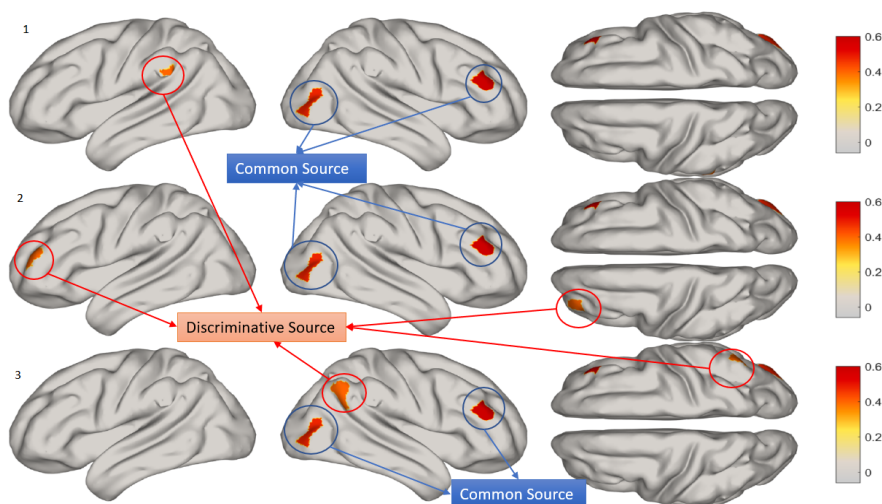
Figure 3.8: Ground truth common sources and discriminative source corresponding to 3 different classes.
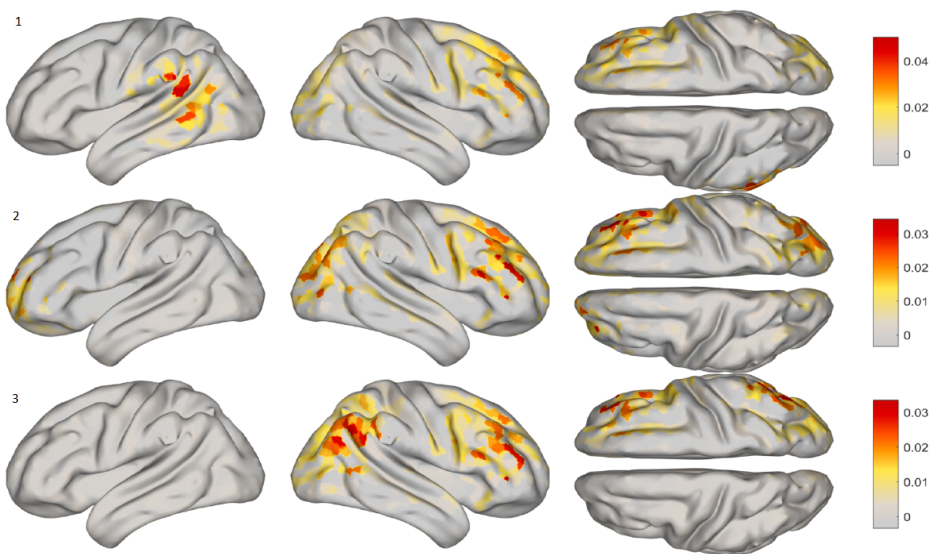
Figure 3.9: Solution from wMNE algorithm for 3 classes with left lateral view, right lateral view and superior view respectively from left to right.
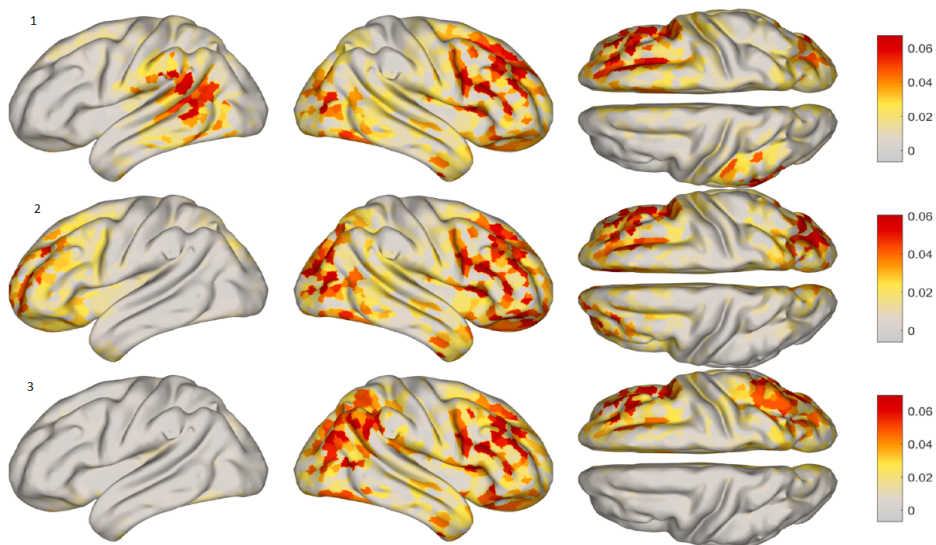
Figure 3.10: Solution from sLORETA algorithm for 3 classes with left lateral view, right lateral view and superior view respectively from left to right.
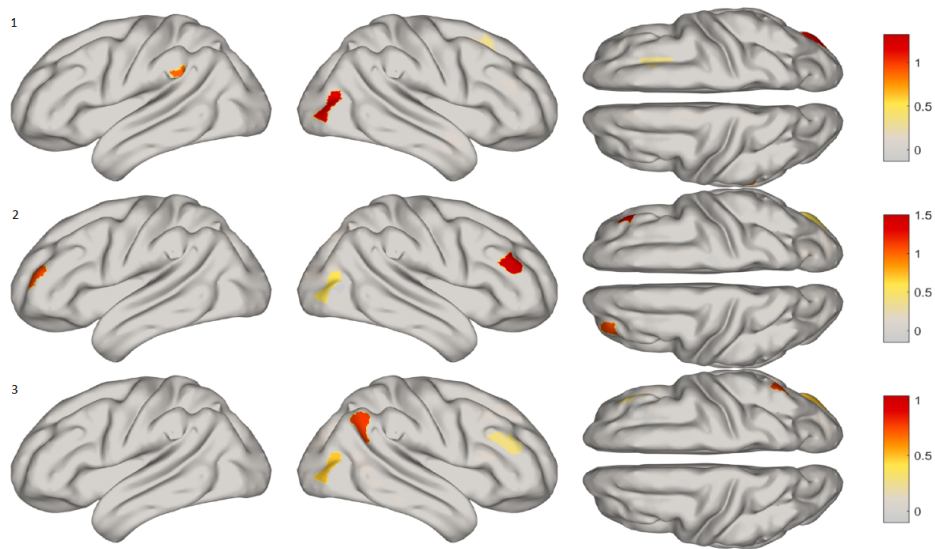
Figure 3.11: Solution from Homotopy algorithm for 3 classes with left lateral view, right lateral view and superior view respectively from left to right.
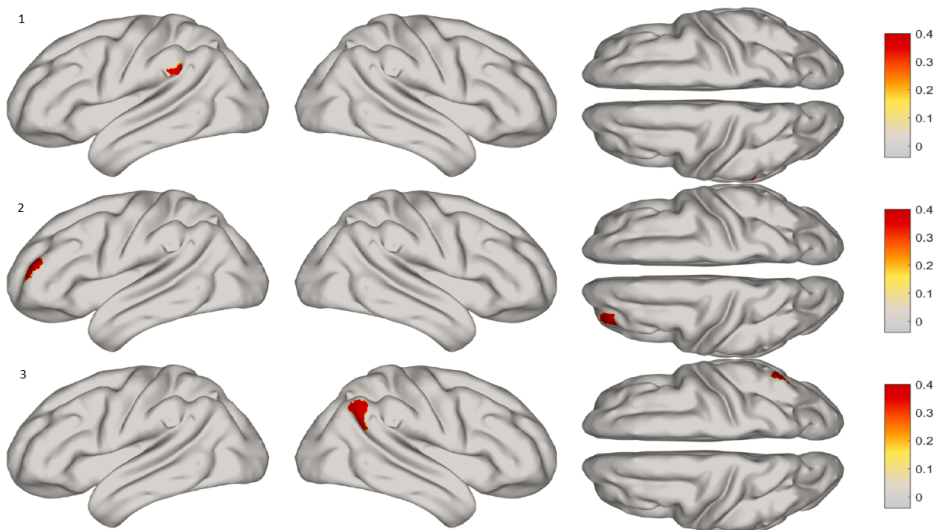
Figure 3.12: Solution from Homotopy algorithm for 3 classes. Each row is corresponding to each class with left lateral view, right lateral view and superior view respectively from left to right.

3.5 Conclusion and Discussion

We aim to reconstruct discriminative sources given different brain status. A label guided dictionary learning formulation is given for the first time is solved using our revised version of the DK-SVD algorithm. Through numerical simulations, we showed that regarding accuracy and speed, our method is better than the ℓ_1 or ℓ_2 related ones. The reason is the high coherence of lead field matrix and sparsity constraints are easy to fail. The classification component trained a W matrix with each row corresponding certain type of brain status, which is physically meaningful, we termed as a discriminative filter. Our proposed framework can achieve satisfactory result compared to traditional methods and can be extended to more specific priors such as spatially smoothness requirement or depth compensation requirement.

Even though in the same experiment setting, our algorithm performs better than the benchmark algorithms, we find that there is a large portion of outliers regarding localization error in the algorithm when the linear mapping true source location has a high coherence with the linear mapping from sources at other locations. The intuition is if the SNR is higher, the more accurate the localization performance it should be. However, due to the huge computation time, we only repeated 20 times of each experiment. The comparison of the proposed algorithm with the benchmark algorithms under the same setting makes more sense rather than compare across different experimental settings. The inverse nature of ESI problem makes the accuracy unstable. Further investigation of the impact of level different sensor noises is our future work.

Chapter 4

Graph Regularized EEG Source Mapping using with in-class consistency and out-class discrimination

4.1 Introduction and Motivation

It's worth noting that the previous EEG inverse problem solvers solve the problem in an unsupervised way without taking any available label information. The inverse problem was solved under different brain statuses independently rather compare and discriminate different brain status in a comprehensive and unified framework. Usually, when we design a sequence of experiments to record the EEG and asked the subjects to perform different psychological tasks within certain time windows, the label information (happiness, sadness, surprise, etc. in emotion processing experiment, or different motion imagination tasks in brain-computer interface (BCI) studies) of the recorded EEG data can be easily obtained. Label information in such controlled environment is not expensive to collect. Traditional algorithms solve the EEG inverse problem without leveraging the label information, which will make it hard to compare the reconstructed sources for different brain statuses due to its low SNR (Signal-to-Noise Ratio) and high volume of spontaneous background source activation patterns. EEG data is highly non-stationary, and task-related sources also exhibit time-variant patterns. Thus the EEG inverse solver should also retrieve consistent patterns within each class. To explicitly extract factual sources and promote the in-class consistency and out-class
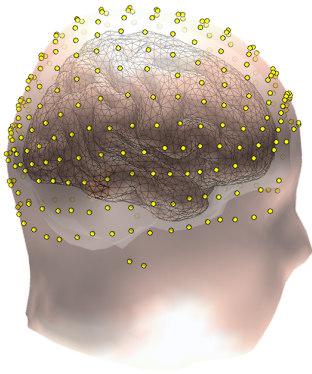
Figure 4.1: Triangle meshed realistic brain model. Each triangular element represents a current dipole located at its center, and the orientation of dipoles is assume to be perpendicular to the cortical surface.
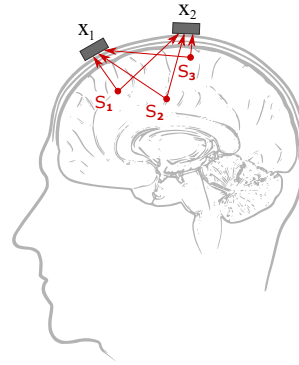
Figure 4.2: Sources propagate to electrodes: s_3 is the common activation source and has larger magnitude, s_1 is a discriminative source corresponding to class 1, and s_2 is a discriminative source corresponding to class 2.

discrimination, we implemented the graph regularized version of discriminative source reconstruction, tested on simulated EEG data, and showed its effectiveness in finding the discriminative sources and precision localization of the task-related sources.

The contributions of this chapter are listed as follows: (1) We propose to use label information to solve the EEG inverse problem in a supervised way. (2) A graph regularized EEG inverse model is presented that can promote in-class consistency and out-class discrimination. (3) A Voting Orthogonal Matching Pursuit algorithm is given to decompose the common sources.

4.2 Proposed Framework

4.2.1 Discriminative Source Reconstruction with Graph Regularization

According to previous research [38] [76], most the EEG potentials originate from the non-task related spontaneous neural firing that can be regarded as the background activity. Combined with the fact that an EEG signal is non-stationary with low SNR, traditional method is hard to extract discriminative signal of interests. A simple example is shown in Fig.4.2, s_1 and s_2 represent the discriminative sources corresponding to class 1 and class 2, s_3 is the common source shared by class 1 and class 2. If the magnitude of s_3 is much larger than s_1 and s_2, a lot of algorithms will fail to infer the discriminative sources under low SNR. In the following numerical experiments section of this paper, we use similar source configurations: each class has a dominant primary source that is shared with other classes and relatively small secondary source that is unique to this class. We are trying to get consistent inverse solutions under the same brain state and discriminative solutions given different brain states [77] utilizing the available label information. Inspired by the successful applications of graph regularization in computer vision community [30] [14], the proposed model is in the form of sparse representation of discriminative sources with a graph regularization term, which is termed as Laplacian Graph Regularized Discriminative Source Reconstruction (LGRDSR), and includes the source reconstruction fidelity term and label guided in-class consistency and out-class discrimination term:

$$\langle S \rangle = \arg\min_{S} \|X - LS\|_F^2 + \alpha\|S\|_{1,1} + \frac{\beta}{2}\sum_{i,j=1}^{N}\|s_i - s_j\|_2^2 M_{ij}, \qquad (4.1)$$

41

where $X \in \mathbb{R}^{N_c \times N}$, N is the total number of time points from different classes, $\|\cdot\|_{1,1}$ is the ℓ_1 norm notation for a matrix, equal to the sum of the absolute values of all elements in a matrix, the second term is the cost of sparse coding, and the third term is the graph regularization term that requires the sources within the same category to have similar patterns while making the sources for different classes to be distinct. The definition of the M matrix is written as:

$$M_{ij} = \begin{cases} +1, & \text{if } (s_i, \text{s}_j) \text{ belong to the same class} \\ -1, & \text{if } (s_i, \text{s}_j) \text{ belong to different classes} \end{cases}$$

The goal of this formulation is to find discriminative sources while maintaining the consistency of in-class reconstructed sources.

Remarks on *design of M matrix*

When (s_i, s_j) belong to the same class, the value of M_{ij} should be positive, which will penalize difference in in-class sources. By driving the intrinsic geometric structure of s_i and s_j to be the same, the in-class consistency of the sources can be achieved.

When (s_i, s_j) belong to different classes, assigning a negative value to M_{ij} will explicitly promote out-class discrimination of the source. In practice, if we care more about in-class consistency, we can set $M_{ij} = 0$ when (s_i, s_j) belongs to different classes. The magnitude of M_{ij} can also be adjusted to tailor the relative weight between in-class consistency and out-class discrimination.

Define D as a diagonal matrix whose entries are column or row sums of the symmetric matrix M, $D_{ii} = \sum_j M_{ij}$, define $G = D - M$, where G is called the graph Laplacian Matrix [14], The third term of Eq.4.1 can be further derived as:

$$\sum_{i,j=1}^{N} \|s_i - s_j\|_2^2 M_{ij} = \sum_{i,j=1}^{N} (s_i^T s_i + s_j^T s_j - 2 s_i^T s_j) M_{ij} = 2tr(SGS^T).$$

As a result, Eq.4.1 is written as

$$\langle S \rangle = \arg \min_{S} \|X - LS\|_F^2 + \alpha \|S\|_{1,1} + \beta (Tr(SGS^T)). \qquad (4.2)$$

Eq.4.2 can be rewritten into a decomposed form

$$\langle s_1, s_2, \ldots s_N \rangle = \arg \min_{s_1, s_2, \ldots s_N} \sum_{i=1}^{N} \|x_i - Ls_i\|_2^2 + \beta \sum_{i,j=1}^{N} G_{ij} s_i^T s_j + \alpha \sum_{i=1}^{N} \|s_i\|_1. \quad (4.3)$$

Fixing the other sources s_j ($j \neq i$) while solving s_i, each problem is presented as

$$\langle s_i \rangle = \arg \min_{s_i} \|x_i - Ls_i\|_2^2 + \beta G_{ii} s_i^T s_i + s_i^T h_i + \alpha \sum_{k=1}^{N_s} \left| s_i^{(k)} \right|, \qquad (4.4)$$

where $h_i = 2\beta (\sum_{j \neq i} G_{ij} s_j)$, and $s_i^{(k)}$ is the k-th coefficient of vector s_i. Eq.4.4 can be solved using feature-sign search algorithm [45] [14] [59]. To better describe the feature-sign search algorithm, denote $g(s_i) = \|x_i - Ls_i\|_2^2 + \beta G_{ii} s_i^T s_i + s_i^T h$ and $f(s_i) := g(s_i) + \alpha \sum_{k=1}^{N_s} \left| s_i^{(k)} \right|$, Eq.4.4 is rewritten as $\langle s_i \rangle = \arg \min_{s_i} f(s_i) = \arg \min_{s_i} g(s_i) + \alpha \sum_{k=1}^{N_s} \left| s_i^{(k)} \right|$. Each s_i is solved sequentially while fixing other s_j ($j \neq i$). Algorithm (2) presented the famous feature-sign search algorithm properly adapted for Eq.4.2 with the graph regularized term. Note that the analytical solution for Eq.4.4 is $\tilde{s}_i^{new} = (L^T L + \beta G_{ii} I)^{-1} (\tilde{L}^T x_i - \frac{\alpha \tilde{\theta} + \tilde{h}_i}{2})$ in part b) of the feature-sign stage of Algorithm (2), and the inversion of $L^T L + \beta G_{ii} I$ is the most computationally expensive part since L matrix is overdetermined wide matrix, the calculation speed can be boosted by using *Woodbury formula* [88]:

$$(L^T L + \beta G_{ii} I)^{-1} = \frac{1}{\beta G_{ii}} (I - \frac{1}{\beta G_{ii}} L^T (LL^T + \frac{1}{\beta G_{ii}} I)^{-1} L).$$

The inverse operation of a matrix with the same dimension as the number of dipoles/voxels is reduced to the inverse of a matrix with the dimension number equal the total number

43

of electrodes, as a result, the calculation cost is reduced significantly. Different from original version of feature sign search algorithm which includes only the inner for-loop, Algorithm (2) has an while-loop since the updates of all $s_j (j \neq i)$ will impact the solution of s_j due to the inclusion of graph regularized term, the algorithm stops until the convergence of S^*.

4.2.2 Common Sources Decomposition with Voting Orthogonal Matching Pursuit (VOMP)

Under the assumption of strong common spontaneous source activation pattern, the contribution of discriminative sources to the EEG recorded data is relatively small, making the solution space for different classes highly correlated, which limits the capability of discrimination. Previous research has shown that pulling out the high absolution value of coefficients s_{ij} associated with the common activation pattern can assist to find the discriminative source of interest [10].

In the similar way as addressing the "cross-and-bouquet" model presented in [90], a useful step is decomposition of X for better extraction of discriminative sources. Similar procedure can be found in [93]. As we assumed, the spontaneous source activation pattern is very strong, thus making the convex hull spanned by all the source configuration to a tiny portion of the space [90]. The Voting Orthogonal Matching Pursue (VOMP) is proposed as given in Algorithm 3. The aim is to extract the common sources across all classes by voting the most popular source location using stepwise orthogonal matching pursuit. Problem (4.5) describes the common source decomposition problem. The VOMP is considered as an integral preprocessing part to find discrimi-

Algorithm 2 Feature-sign search algorithm

INPUT: Lead field matrix L, EEG data X, graph matrix G, parameter α and β

OUTPUT: Source matrix S

while S^* is not converged

for $i = 1, \ldots, N$

1. Initialization:

$s_i := \overrightarrow{0}$, $\theta := 0$, *active set* $\mathcal{A} := \{\}$, where $\theta_j \in \{-1, 0, 1\}$ denotes $\text{sign}(s_i^{(j)})$

2. Update of the active set:

For all zero coefficients of s_i, find $j = \arg\max_j |\frac{\partial g(s_i)}{\partial s_i^{(j)}}|$, add j to the *active set* $\mathcal{A}$

only if it locally improves the objective, under the following conditions:

if $\frac{\partial g(s_i)}{\partial s_i^{(j)}} > \alpha$, then let $\theta_j := -1$, $\mathcal{A} = \mathcal{A} \cup \{j\}$.

if $\frac{\partial g(s_i)}{\partial s_i^{(j)}} < -\alpha$, then let $\theta_j := 1$, $\mathcal{A} = \mathcal{A} \cup \{j\}$.

3. Feature-sign step

a) Let $\tilde{L}$ be a submatrix of L that contains only the columns corresponding to the *active set* $\mathcal{A}$, $\tilde{s}_i$ and $\tilde{h}_i$ is the subvectors of s_i and h_i similarly defined.

b) The analytical solution for Eq.4.4 is derived:

$\tilde{s}_i^{new} = \frac{1}{\beta G_{ii}}(I - \frac{1}{\beta G_{ii}}L^T(LL^T + \frac{1}{\beta G_{ii}}I)^{-1}L(\tilde{L}^T x_i - \frac{\alpha\tilde{\theta}+\tilde{h}_i}{2}).$

c) Perform discrete line search from $\tilde{s}_i^{new}$ to $\tilde{s}_i$:

Examine the objective value at $\tilde{s}_i^{new}$ and all points where any coefficient changes sign.

Update $\tilde{s}_i$ (and corresponding entries in s_i) where the objective function achieves the lowest value.

Remove the zero coefficients of $\tilde{s}_i$ from the *active set* and update $\theta = sign(s_i)$.

4. Check the optimality conditions

a) Optimality condition for nonzero coefficients: $|\frac{\partial g(s_i)}{\partial s_i^{(j)}}| + \alpha\text{sign}(s_i^{(j)}) = 0$, for all $s_i^{(j)} \neq 0$.

If condition (a) is not satisfied, go to step 3 to perform discrete line search.

b) Optimality condition for zero coefficients: $|\frac{\partial g(s_i)}{\partial s_i^{(j)}}| < \alpha$, for all $s_i^{(j)} = 0$.

If condition (b) is not satisfied, got to Step 2; otherwise return s_i as the solution, denoted as s_i^*

end for

end while
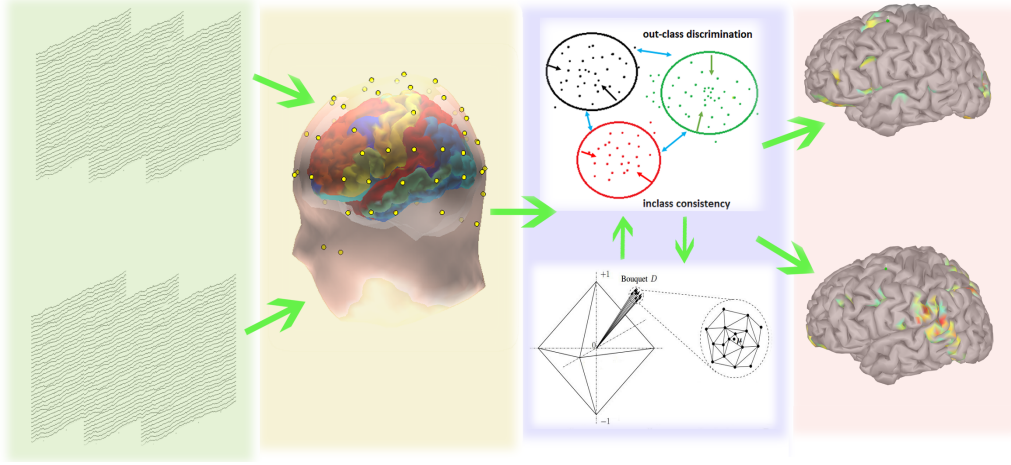
Figure 4.3: Procedures of our framework: After gathering labeled EEG recorded data, the brain model is constructed using finite element method (BEM) based on MRI images, then we first use the VOMP algorithm to decompose the primary common source starting with a high minimum voting percentage, and then solve it using feature-sign search algorithm, validate the source configurations and do these steps alternative until solutions are converged, the last step is to map discriminative sources to the cortex.

native sources. The procedure to solve Problem (4.2) is given in Algorithm (4) and is illustrated in Fig.4.3.

$$\langle S_c \rangle = \arg\min_{W_c} \|X - LS_c\|_F^2$$
$$s.t. \ \|s_i\|_0 \leqslant T_{max}, \quad i = 1, 2, ... N_d$$
$$s_i = s_j, i = 1, 2, ... N_d, j = 1, 2, ... N_d \tag{4.5}$$

After the decomposition of common source, its contribution to the EEG data X is also removed. The new EEG data after removal of the common source is written as $X_{new} = X - LS_c$. In the following part, we still use X to represent X_{new} when no confusion is caused.

Algorithm 3 Decomposition of Non-discriminative Sources with VOMP

INPUT: Lead field matrix L, EEG data X, maximum number of common sources T_{max}, minimum voting acceptance threshold p

OUTPUT: S_c, result of removed common sources X_{new}

Initialization: $T \leftarrow 1$, $\Omega = \emptyset$, $R = X$, $R_{new} = X$, $S' = 0$

    while Stopping criteria is not met **do**
        for $i \in 1, ..., N_t$ **do**
            $s_i \leftarrow \text{OMP}(L, x_i, 1)$
            $q_i \leftarrow$ nonzero index of s_i
        end for
        $q_{best} \leftarrow$ most frequent q_i
        if $T = T_{max}$ or frequency of $f(q_{best}) < p$ **then**
            break;
        else
            $\Omega \leftarrow \Omega \cup q_{best}$; $L' = (L_{:,i}|i \in \Omega)$; $S' \leftarrow pinv(L')X$; $S' \leftarrow mean(S')$;
            $R_{new} \leftarrow X - L'S'$
        end if
        for $k \in 1, ..., C$ **do**
            $R_{new}^k = \{R_{new}(i)|i \in \text{class } k\}$;
            $R^k = \{R(i)|i \in \text{class } k\}$
        end for
        if $\|R_{new}^k\| < \|R^k\|$ for $k \in 1, ..., C$ **then**
            continue;
        else   **break**;
        end if
        $T \leftarrow T + 1$; $R \leftarrow R_{new}$
    end while
    $X_{new} = R_{new}$; $S_c = S'$
    return S_c, X_{new}

Algorithm 4 Proposed framework of solving Problem (4.2)

INPUT: Lead field matrix L, EEG data X, graph matrix G
OUTPUT: Discriminative source S_d
Initialization: $T \leftarrow 1$, $\Omega = \emptyset$, $R = X$, $R_{new} = X$, $S' = 0$
    while stopping criteria not met **do**
        (1) Use VOMP algorithm for common source decomposition.
        (2) Solve the following sparse coding problem for
        $\langle S \rangle = \arg\min_{S} \|X - LS\|_F^2 + \alpha\|S\|_{1,1} + \beta(Tr(SGS^T))$ using the feature-sign
        search algorithm described in Algorithm (2) .
        (3) Adjust the voting threshold p.
    end while

4.3 Numerical Results

4.3.1 Experiment setup

We used a recently developed realistic head model called ICBM-NY or "New York Head" [40] which is based on highly detailed standardized finite element model (FEM) of the non-linear averaged anatomical template-ICBM152. The "New York Head" model has two different precision levels, corresponding to 74382 and 2004 voxels respectively. The dimension of lead field matrix we are using is 108×2004, representing 108 channels and 2004 voxels. We also assume that source orientation is perpendicular to the cortex surface. In Ref. [81] Sohrabpour et al. estimated source when the source signal is around the peak value, the similar practice can be found in Ref. [54]. As is shown in the experiment part of Ref. [69], the source images are plotted when the source activation is at peak value. Here in our experiments, we designed all the source activation magnitude bearing a positive value. For really EEG data, a technique called energy thresholding (in the following subsection) can be used to find the corresponding EEG data samples that have non-zero source activation pattern. In each

48

simulation, noises originate from sensor level and cortex voxel level both contributed to the recorded EEG data. The SNR is calculated as

$$SNR = 20 \log_{10} \frac{\|S\|_2}{\|N\|_2}.$$

The brain is divided into 8 Region Of Interest (ROI)s, namely RAI Right Anterior (RAI), Right Anterior Superior (RAS), Right Posterior Inferior (RPI), Right Posterior Superior (RPS), Left Anterior Inferior (LAI), Left Anterior Superior (LAS), Left Posterior Inferior (LPI), Left Posterior Superior (LPS) [34]. In the simulation experiments, we designed common sources that contain much higher magnitude and three discriminative sources related to three brain states with smaller magnitude from different ROIs. All computations in this paper were conducted on a 64–bit Linux workstation with i7-5960x CPU, a memory of 64 GB and frequency is 3.00 GHz.

4.3.2 Validate the VOMP algorithm

In this subsection, we validated the VOMP under different SNR and source configurations. The voting threshold p was set to different values to test the VOMP's performance. For example, if we set the voting threshold to be 0.5, it means that a common source is determined when at least half of the samples in each class "agreed" the common source pattern. Note that, when there are more than 3 classes, the common source pattern is still extracted if more than 50% of at least two classes shared the same pattern. The VOMP algorithm can be further improved by using multi-step VOMP, which is to run OMP for multiple steps for each sample instead of just one step as described in Algorithm (3), and then aggregate the common source location information calculated from above steps and only keep the best one in terms of occurrences, and find

49

the residual matrix and continue the VOMP procedure. Another improvement is that the spatially adjacent source locations can be regarded the same instead of treating them differently, as they have similar forward mappings.

The VOMP algorithm tries to reduce the signal correlation by decomposing common sources. Two experiments were conducted under different SNR values and source configurations. Each time, a different voting threshold was tested. In the first experiment, there are two common sources and two discriminative activated sources at different ROIs corresponding to three classes. Both noises originating from brain voxels and white noise from sensor measurement are added to the original signal. In the first experiment, the noise level is SNR= 17 dB. In the second experiment, the SNR is 12 dB with 3 common sources. The energy boxplots of 600 samples from 3 different classes under different voting threshold p are given in Fig.4.4. and Fig.4.5 for both experiment setups. The first common source can easily be extracted in the first iteration. However, if the noise level is large, it's hard to reach a consensus for a voting threshold $p = 0.3$ as is shown in Fig.4.5. Choose a small p will introduce false common source that will cause potential problem locating the right discriminative source. Our framework requires to check the accuracy and soundness of the final prediction and adjust the threshold back and forth. A recommended starting search point is $p = 0.2$. The advantage of VOMP is its speed as its core ingredient is OMP, and the evaluation time for each sample took 1.2763×10^{-4} s on our workstation.

An example of our VOMP algorithm in filtering out the common background iteratively is illustrated in Fig.4.6, which is the time series version of "cross-and-bouquet" example, in contrast to the image recognition version as is illustrated in Fig.2 of Ref.
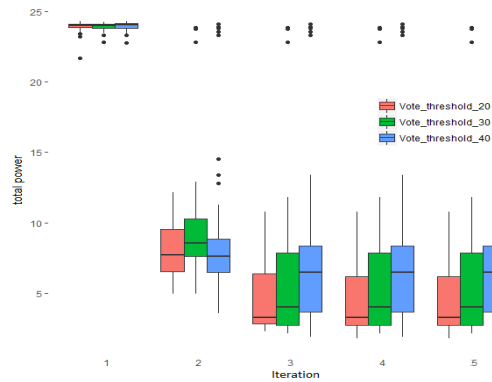
Figure 4.4: Boxplot of total signal energy of 50 experiments: to show the effectiveness of VOMP in removal of common souces under SNR=12 with 3 common sources.
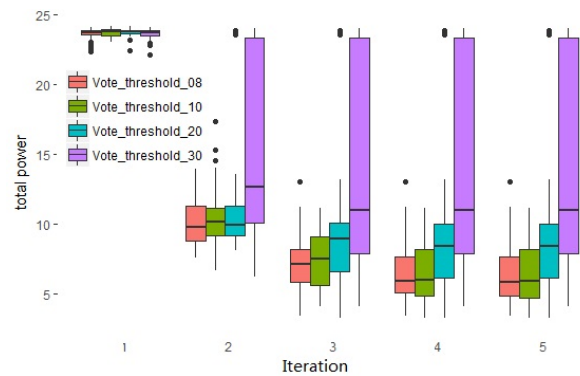
Figure 4.5: Time series plot of common source decomposition: from left to right, common sources are removed iteratively.

[89].
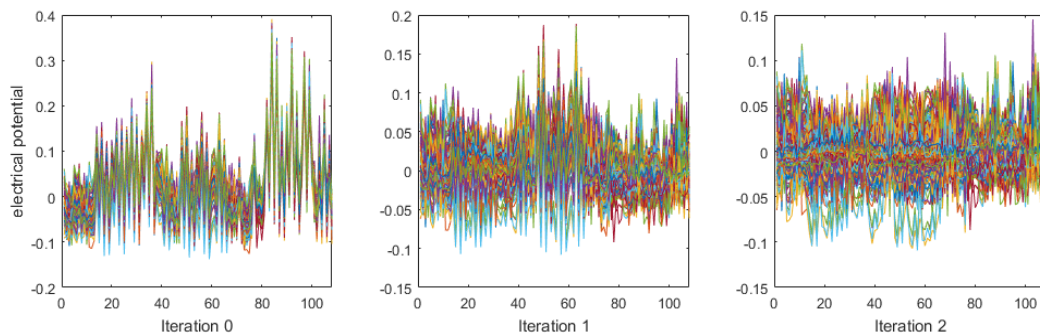
Figure 4.6: Time series plot of common source decomposition: from left to right, common sources are removed iteratively.

4.3.3 Discussion on Tuning the Parameters

Usually, if there are two parameters, the common practice is to do a grid search and find the best combination of the best performance. However, this can involve a

lot of computation to find the best parameters. Moreover, the performance measurement can be misleading since it's not a direct measurement of accuracy, which is based on squared error of the reconstructed signal and the ground truth signal. Instead, it's based on the shortest path distance between inferred location and true source location. For example, if the ground truth signal is $(1, 0, 0, 0)$, the first reconstructed signal is $(0, 1, 0, 0)$, and the second reconstructed signal is $(0.3, 0, 0.7, 0)$, with the assumption that the neighboring elements in the vector are also neighboring voxels in the brain, the first reconstruction has larger squared error compared to the second one, even though the first one has better performance (location) precision. If the reconstructed sources are spurious ones (can be anywhere inside the brain), a better performance does not really mean the parameter setting is better compared to worse performance in one numerical experiment. It may mean the spurious source with better accuracy happened to locate a source close to the actual source.

Based on the discussion above, its quite tricky to find the best combination of parameters. However, there are some ways to fine-tune the parameters. We propose a two-step fine-tuning mechanism. In the first step, we assign the graph regularization weight β to 0 and try to solve the simple ℓ_1 constrained problem using the Homotopy algorithm and find the best setting of α, which is quite easy since there is only one parameter to tune. The second step is to find the best value of β while fixing α. The rationale behind this is that our proposed model works well if the ℓ_1 problem can be solved with accurately. The graph regularization term can smooth out spurious sources that are not shared within a class, and the representative sources are encouraged and remained. The localization error under a different parameter setting is illustrated in Fig.4.7 under SNR

52

= 16. Fig.4.7 is based on a result from 3rd outer iterations depicted in Algorithm (2). The maximum inner iteration is set to be 50. We assigned 250 mm when the inferred location is in a different hemisphere for visualization purposes. When the parameters are not well set, the graph penalty term will drive all the inferred source location from all time points to the wrong hemisphere. When the sparse regularization parameter α is set to be large, the solution will be a zero matrix.
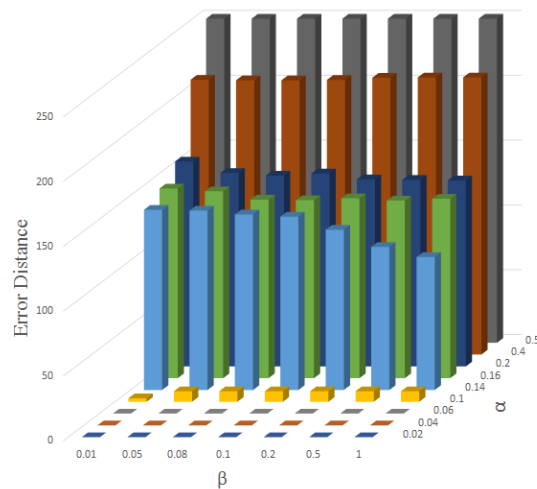
Figure 4.7: Discriminative source location error (in mm) given different parameter settings

4.3.4 Effect of Graph Regularization

In this section, we show the effectiveness of the graph regularization term in reconstructing the discriminative sources by comparing it with the other eight benchmark algorithms. We designed the spontaneous common sources with a magnitude of 0.8 with standard deviation to be 0.1 and task-related discriminative source with a magnitude of 0.2 with a standard deviation of 0.05 located in different ROIs from the common

sources.

We sampled 200 time points for each class and did the experiment 5 times to get the average accuracy of the reconstructed source. For the LGRDSR parameter, we set β to be 0.05 and α to be 0.06; M_{ij} is set to 1 if sample i and j belong to the same class since we care more about in-class consistency based on the example. The noise matrix is designed to affect the EEG recording together with the true source signal. For each time point, 3 random voxels are corrupted randomly with the average value being 0.2, 0.4, 0.6 and variance being 0.05 based on different SNR design. The 8 benchmark methods include ElasticNet [86], Homotopy [5], DALM [100], PDIPA [100], FISTA [100], sLORETA [71], MNE [31]. The former six algorithms are compared in image reconstruction applications and can be referred to Ref. [93] for details. The reconstruction performance of the proposed method, as well as the benchmark methods based on 150 experiments, are given in Table 4.1.

In Table 4.1, computation time is recorded in seconds (s), PSE represents primary source error, which is the distance of reconstructed primary source to the ground truth primary source. The distance evaluation is based on the shortest path of two voxels on the cortex surface instead of direct Euclidean distance. PSE measures the capability of each algorithm to reconstruct the common sources.

All of the values in Table (1), except the Time column in the table represents distance in (mm) from ground true source to the reconstructed source. When the reconstructed location is on a different hemisphere from the ground truth, there is no path connecting those two voxels, so we mark the distance to be 250 mm. EC1 represents error for class 1, which is the distance of the reconstructed discriminative source

54

to the ground truth. EC2 and EC3 are similarly defined. To illustrate the effect of the proposed framework, the ground truth of the activated pattern is given in Fig.4.8, with the reconstructed source estimated by MNE, sLORETA, Homotopy, DALM and our method given in Fig.4.9–Fig.4.13. We can see from Table (4.1) and the Fig.4.9–Fig.4.13 that when the SNR is large, all the algorithms perform well in reconstructing primary sources. As for the discriminative sources for different classes, our method can achieve almost perfect reconstruction. All other algorithms' performances are also acceptable when SNR is large, except for sLORETA, MNE and ElasticNet. When we increase the noise, all of the algorithms can still achieve high accuracy in finding the primary source. For the discriminative source, our algorithm performs much better. We also validated that, to solve a pure ℓ_1 EEG inverse problem, the Homotopy algorithm performs better in most cases than other algorithms in the EEG inverse problem, which is in accordance with Ref. [93].
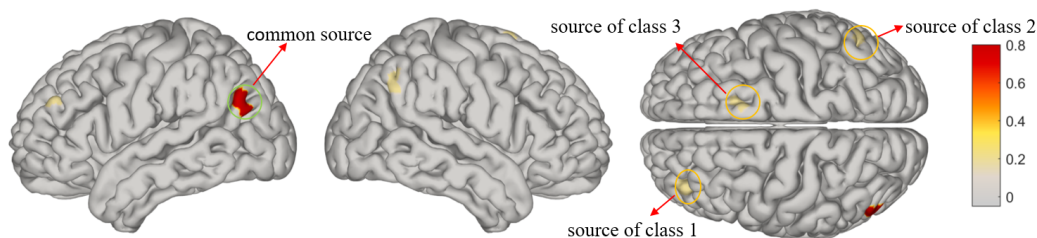
Figure 4.8: Ground truth for all 3 classes

4.3.5 Signal Energy Thresholding

In our experiments, we designed our primary sources to hold a large value, and the magnitude of discriminative sources are also larger than zero. One may argue that

55

Table 4.1: Reconstruction Accuracy Summary

Methods	SNR = 10					SNR =16					SNR = 22				
	Time	PSA	EC1	EC2	EC3	Time	PSA	EC1	EC2	EC3	Time	PSA	EC1	EC2	EC3
ElasticNet	0.001	43.4	142.3	159.6	159.2	0.001	21.5	188	162.3	136.0	0.001	8.87	172.5	195.0	13.0
Homotopy	0.12	3.43	53.2	42.5	40.8	0.11	0.006	20.9	23.4	45.9	0.09	0	0.28	0.70	8.00
DALM	0.07	4.59	53.0	43.1	39.6	0.07	0.01	20.9	22.0	45.5	0.08	0	0.28	1.73	7.98
PDIPA	0.29	3.43	53.4	45.0	40.4	0.31	0.006	22.1	26.7	48.4	0.26	0	0.28	0.63	7.98
L1LS	3.89	0.69	51.6	67.4	37.1	3.98	0.25	24.6	24.0	47.1	3.92	0.069	0	0	4.36
FISTA	0.95	0.63	61.0	95.2	47.6	0.95	2.92	44.1	33.1	62.9	0.96	40.1	66.1	73.5	54.5
sLORETA	0.015	10.2	131.7	178.2	142.8	0.015	16.9	200	175.1	152.1	0.02	2.62	194.1	164.2	123.5
MNE	3e-5	29.3	131.8	157.7	131.7	3e-5	9.02	197.5	174.9	131.9	3e-5	4.30	119.8	136.2	113.5
LGRDSR	0.15	1.85	14.4	4.13	3.67	0.13	0.006	0	5.42	10.2	0.10	0	0	0	2.12
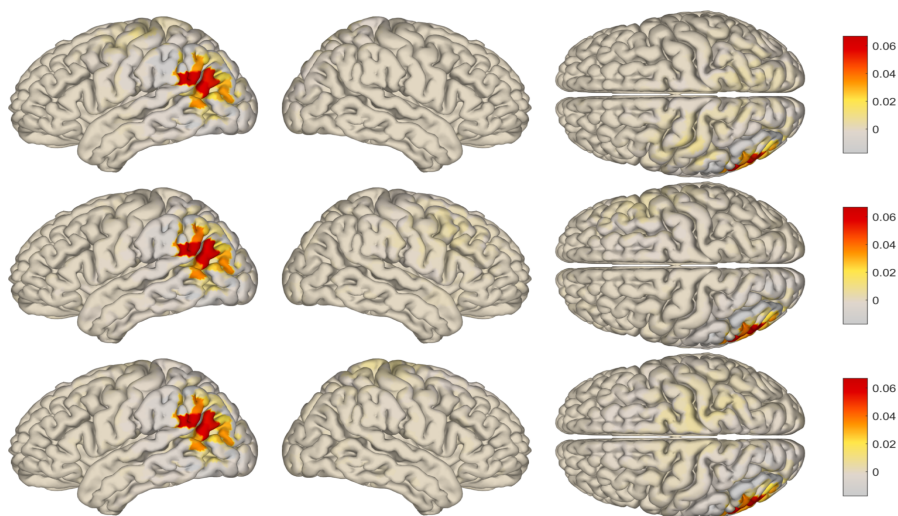
Figure 4.9: MNE solution: The above row is the MNE solution for class 1; Class 2 and class 3 is illustrated in the middle and bottom row. The solution MNE gives is not sparse, with too many spurious sources of small magnitude.
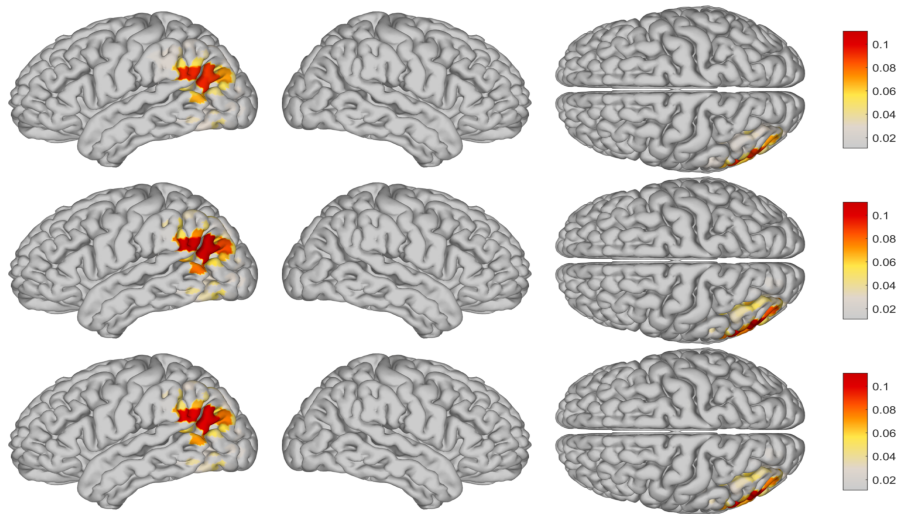
Figure 4.10: sLORETA inverse solution: sLORETA solution for class 1, class 2 and class 3 is illustrated from the top to bottom rows. sLORETA can successfully reconstruct the primary source, however the secondary source is not successfully reconstructed. Compared to the solution of MNE, sLORETA can suppress the numerous spurious sources with small magnitude.
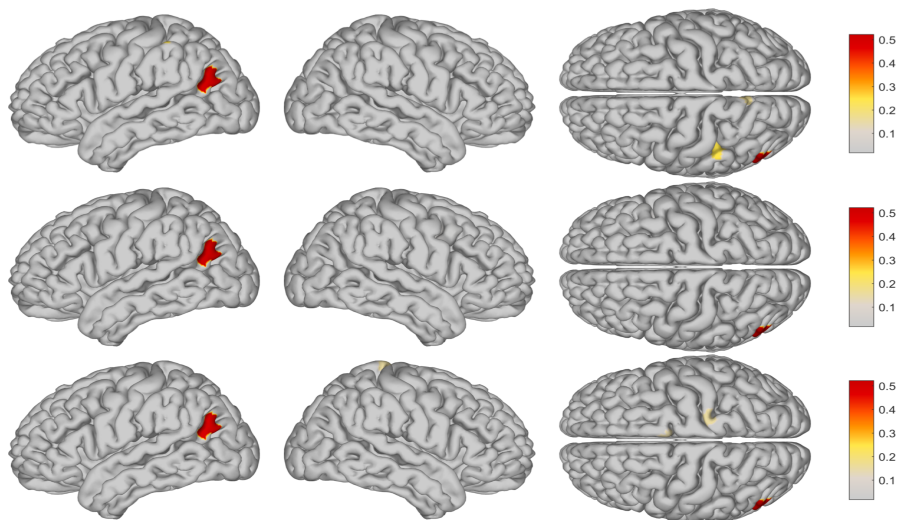
Figure 4.11: Homotopy inverse solution: From top to bottom are the Homotopy solution for class 1, Class 2 and class 3 respectively. Homotopy can successfully reconstruct the primary source, however the secondary source is not successfully reconstructed.
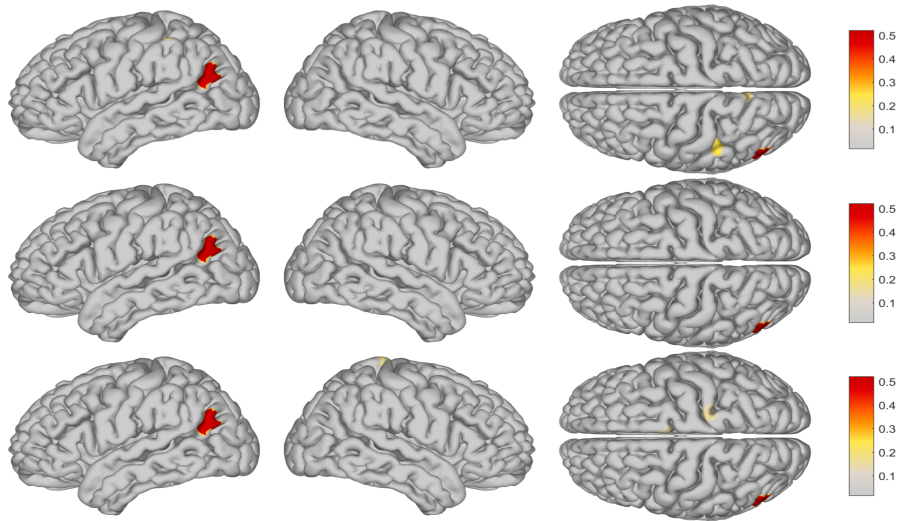
Figure 4.12: DALM inverse solution: DALM can successfully reconstruct the primary source, however the secondary source is not successfully reconstructed. Compared to the solution of MNE and sLORETA, the solution is better in terms of accuracy and sparsity, similar performance compared to Homotopy.
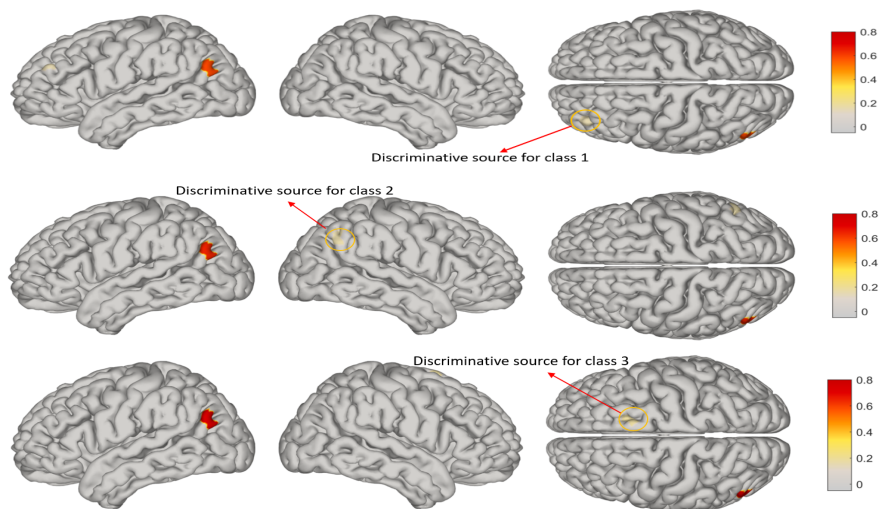
Figure 4.13: LGRDSR reconstructed source: The reconstruction solutions for 3 classes are given in each row. As can be seen from the illustration, the discriminative source can be successfully reconstructed compared to other methodologies.

it's not realistic since the value we designed is never close to zero in real situations. However, the logic behind it is that once the source signal is close to zero, its contribution to the EEG data can't be reflected, making the corresponding reconstruction impossible. A useful technique to circumvent this problem is using Energy Thresholding (ET) of the EEG data. The purpose of ET is to eliminate data points of low energy with the hope of inferring a source signal that is not close to zero. The relationship between EEG data and source is $x_i = Ls_i + \epsilon$. Energy of the signal is defined as $p(x_i) = x_i^T x_i$. To find out the relationship of $p(x_i)$ and $p(s_i)$, we did a linear regression to predict $p(x_i)$ using $p(s_i)$ based on Monte Carlo simulation with 3000 samples, and found the linear trend between $p(x_i)$ and $p(s_i)$ is statistically significant, and the detailed regression model is given in Table (4.2). From previous research, the Event-

Table 4.2: Regression result on energy of signal and source

	Estimate Std.	Error	t value	$Pr(> |t|)$
(Intercept)	0.004841	0.008742	0.554	0.58
x	0.144889	0.007761	18.669	2e-16

related potential demonstrates higher energy on P1 and N1 points that can be used to do the source mapping [60]. By using ET techniques, we can select the EEG data points with higher energy that correspond to source signals with higher energy. The discussion above shows it's reasonable to set the source signal with a magnitude not close to zero.

4.4 Conclusion and Future Goal

In this paper, we proposed using label information to retrieve discriminative sources corresponding to different brain statuses, extending the traditional EEG source

imaging problem to a supervised one guided by label information. Although determining a sparse representation with graph regularization in the computer vision and compressive sensing communities is not new, its application in the EEG inverse problem that implicitly utilizes label information has never been proposed. Our model employed a Laplacian graph regularized term that can boost the in-class similarity and discourage the out-class similarity, thus making the source solution from the same class more robust to noise. Numerical results show the proposed algorithm outperforms eight benchmark algorithms in localizing the task related sources under certain levels of noise. We showed the common source decomposition using the "cross-and-bouquet" model in the inverse problem and presented an efficient algorithm to address the high background spontaneous source signals. Our proposed supervised version of EEG source imaging algorithm can be incorporated with other state-of-the-art algorithms. To sum up, the EEG inverse problem can be solved in a supervised framework, and it's beneficial to formulate it in that way to extract task related source activation patterns.

We tried to mimic the true source activation data using the simulated data. As it is well studied using fMRI data, our brain contains a resting state default mode network with some spontaneous neural behavior in certain brain areas. Another fact is that when given a specific task, different brain regions can be activated which correspond to the discriminative sources described in our paper. In that perspective, our model is more realistic than numerous previous studies that used simulated data. However, the weakness of our paper is that we used one spot as a common activated source, even though there may be several common source activation regions co-existing in reality. Overcoming this weakness is one of our future research goals.

60

Chapter 5

Graph Regularized EEG Source Mapping in Transformed domain with Total Variation

5.1 Graph Regularized EEG Source Imaging in Transformed Domain

The idea of transform sparseness in solving ESI was first reported by by Ding in 2009 using a first order total variation (TV) matrix, which penalize variations between neighboring elements and leading to sparsity in extended source space [22]. In this section, we first introduce the sparse constraints in the transformed domain (first-order TV) which promote the discovery of extended source patches rather than isolated noncontinuous sources on the cortex. Our proposed graph regularized model in the transformed domain is presented in the first part of this chapter. In the second part of this chapter, we use fractional order graph total variation to promote natural spatial smoothness, which requires the center source activation point has the highest magnitude and the magnitude decreases as the distance is farther away from the center point. A practical computation framework is given to solve the ESI problem with spatial and temporal smoothness.

5.1.1 EEG Source Imaging in Transformed Domain

In order to encourage source extents estimation, Ding [22] proposed to used sparse constraint in the transformed domain and the model was termed as Variation-

Based Sparse Cortical Current Density (VB-SCCD). In [101], Zhu *et al* proposed to use multiple priors including variation-based and wavelet-based constraints. The VB-SCCD model can be extended by adding sparse constraint in the original source domain named Sparse VB-SCCD (SVB-SCCD) [10]. The common yet most important term is the total variation term, which encourage the neighboring sources to be activated or remain unactivated simultaneously so that the spatial smoothness can be guaranteed. The total variation measurement was defined on ℓ_1 norm of the transformed domain using a linear transform characterized with matrix V, defined as below:

$$
V = \begin{bmatrix}
v_{11} & v_{12} & \cdots & v_{1N} \\
v_{21} & v_{22} & \cdots & v_{2N} \\
\vdots & \vdots & \ddots & \vdots \\
v_{P1} & v_{P1} & \cdots & v_{PN}
\end{bmatrix}
$$

with

$$
\begin{cases}
v_{ij} = 1; v_{ik} = -1; & \text{if element } j,k \text{ share edge } i \text{ ;} \\
v_{ij} = 0; & \text{otherwise.}
\end{cases}
$$

where $p = 1, ..., P, d = 1, ..., D$, and N is the number of nodes, P is the number of edges from the triangular grid. The motivation of total variation regularization is illustrated in Fig.(5.1), when the red triangle is estimated to be activated, the neighboring blue voxels should also be activated.

The VS describes the differences in amplitude between adjacent voxels, and the VB-SCCD optimization cost function is defined as follows:

$$
\langle S \rangle = \min_S \|X - LS\|_F^2 + \lambda \|VS\|_{1,1}. \tag{5.1}
$$

62
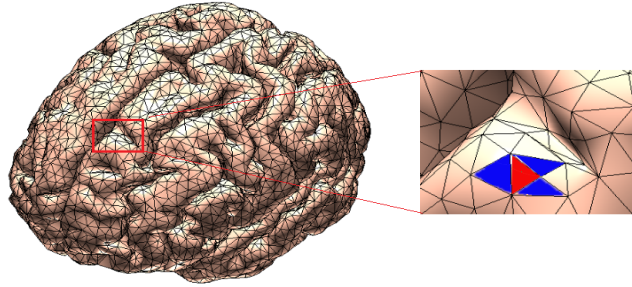
Figure 5.1: Illustration of V matrix design purpose. When one voxel (in red) is activated, the neighbor voxels (in blue) are encouraged to be activated to achieve smaller goal value in Eq.5.1

5.1.2 Discriminative Source Reconstruction with Graph Regularization

Previous studies [38] [76] indicated that the brain spontaneous sources contribute most part of the EEG signal. The neurons in our brain are still active even the subjects are in closed-eye resting state. As a result, the source solution given by traditional EEG inverse algorithm is likely to be corrupted by background noise. A simple example is that suppose $x_1 = L(s_0 + s_1)$ and $x_2 = L(s_0 + s_2)$, and s_0 is the spontaneous common source across different classes: brain status 1 and status 2. s_1 is the discriminative source for class 1, and s_2 is the discriminative source for class 2. Without the label information, traditional method is trying to estimate the overall source activation pattern instead of the task related ones. Even worse, when the magnitude of s_0 is much greater than s_1 and s_2, the traditional method will be more likely to fail.

Inspired by graph regularization in computer vision community for discovering discriminators of images [14, 30, 58, 59, 77], the proposed model employs a graph regularized in the original VB-SCCD and is termed as VB-SCCD-graph in this paper.

63

The graph term tries to eradicate the spurious sources that are not consistent intra-class. The common source are decomposed as the first step using (Voting Orthogonal Matching Pursuit) VOMP algorithm proposed in [49]. The VB-SCCD-graph model is given below:

$$\langle S \rangle = \arg\min_S \frac{1}{2} \|X - LS\|_F^2 + \frac{\beta}{2} \sum_{i,j=1}^{N} \|s_i - s_j\|_2^2 M_{ij} + \lambda \|VS\|_{1,1}. \qquad (5.2)$$

Here $\|\cdot\|_{1,1}$ is the ℓ_1 norm notation for a matrix, equal to the sum of absolute values of all entries from a matrix. $X \in \mathbb{R}^{N \times T}$ the EEG data, where T is the number of samples from different classes. The second term that penalizes the inconsistent source solutions within the same class is the graph regularization term. The definition of M matrix is given as:

$$M_{ij} = \begin{cases} +1, & \text{if } (s_i, s_j) \text{ belong to the same class;} \\ 0, & \text{if } (s_i, s_j) \text{ otherwise.} \end{cases}$$

The goal of this formulation is to find discriminative sources by decomposing the common source while maintaining the consistency of in-class reconstructed sources.

By Defining D as a diagonal matrix whose entries are row sums of the symmetric matrix M, $D_{ii} = \sum_j M_{ij}$ and $G = D - M$, the last term of Eq.5.2 can be further derived as:

$$\sum_{i,j=1}^{N} \|s_i - s_j\|_2^2 M_{ij} = \sum_{i,j=1}^{N} (s_i^T s_i + s_j^T s_j - 2s_i^T s_j) M_{ij} = 2tr(SGS^T).$$

As a result, Eq.5.2 is written as

$$\langle S \rangle = \arg\min_S \frac{1}{2} \|X - LS\|_F^2 + \beta(Tr(SGS^T)) + \lambda \|VS\|_{1,1} \qquad (5.3)$$

Using variable splitting, Eq.5.3 is equivalent to

$$\min_{S} \frac{1}{2} \|X - LS\|_F^2 + \lambda \|Y\|_{1,1} + \beta(Tr(S^T GS)) \tag{5.4}$$
$$s.t. \quad Y = VS.$$

The new formulation makes the objective function separable with respect to two variables S and Y. For Problem (5.4), S can also be written in a decomposed format as

$$\min_{s_i} \frac{1}{2} \|x_i - Ls_i\|_2^2 + \lambda \|y_i\|_1 + \beta G_{ii} s_i^T s_i + s_i^T h_i$$
$$s.t. \quad y_i = Vs_i,$$

where $h_i = 2\beta(\sum_{j \neq i} G_{ij} s_j)$, and x_i, s_i, y_i and z_i are the i-th column of the corresponding matrix, G_{ij} is the (i, j) entry of matrix G.

Remarks: *connection to spatio-temporal smoothness constraint:*

An important assumption in EEG source imaging is the prior to guarantee spatio-temporal smoothness in the source solution [16, 26, 43, 83], our proposed model can assure the spatial smoothness using total variation constraint plus temporal smoothness can be achieved by promoting in-class consistency with graph regularization.

5.1.3 Optimization with ADMM algorithm

Problem (5.5) can be solved with alternating direction method of multipliers (ADMM) [12] after reformulating it to unconstrained augmented Lagrangian function:

$$L_p(s_i, y_i, u_i) = \frac{1}{2} \|x_i - Ls_i\|_2^2 + \lambda \|y_i\|_1 + \beta G_{ii} s_i^T s_i + s_i^T h_i \tag{5.5}$$
$$+ u_i^T(Vs_i - y_i) + \frac{\rho}{2} \|Vs_i - y_i\|_2^2.$$

Augmented Lagrangian methods can bring robustness to the solution compared to other penalty The variable s_i, y_i, u_i are updated sequentially, with the hope that each subproblem has a closed form solution or can be calculated efficiently. In short, ADMM consists of three substeps, given in Eq.5.6 to Eq.5.8,

$$s_i^{(k+1)} := \arg\min_s L_\rho(s, y_i^{(k)}, u_i^{(k)}) = \arg\min_s \frac{1}{2}\|x_i - Ls\|_2^2 + \beta G_{ii}s^T s + s^T h_i$$
$$+ \frac{\rho}{2}\left\|Vs - y_i^{(k)} + \frac{u_i^{(k)}}{\rho}\right\|_2^2 \tag{5.6}$$

$$y_i^{(k+1)} := \arg\min_y L_\rho(s_i^{(k+1)}, y, u_i^{(k)}) = \arg\min_y \lambda\|y\|_1 + \frac{\rho}{2}\left\|Vs_i^{(k+1)} - y + \frac{u_i^{(k)}}{\rho}\right\|_2^2 \tag{5.7}$$

$$u_i^{(k+1)} := u_i^{(k)} + \rho(Vs_i^{(k+1)} - y_i^{(k+1)}) \tag{5.8}$$

The update of $s_i^{(k+1)}$ has a closed form solution, which is

$$s_i^{(k+1)} = P^{-1}[L^T x_i - h_i + \rho V^T(y_i^{(k)} - \frac{u_i^{(k)}}{\rho})],$$

where $P = L^T L + 2\beta G_{ii}I + \rho V^T V$. The update of $y_i^{(k+1)}$ can use the proximal operator in the ℓ_1 norm. Denote the ℓ_1 norm proximal operator as

$$\text{prox}_\mu(v) = \arg\min_x \mu\|x\|_1 + \frac{1}{2}\|x - v\|_2^2, \tag{5.9}$$

with $\mu > 0$. The above problem (6.18) has a closed form solution, called soft thresholding, defined by a shrinkage function,

$$\text{shrink}(v, \mu) = (|v| - \mu)_+ \text{sgn}(v),$$

Algorithm 5 ADMM framework for solving goal function 5.4

INPUT: Lead field matrix L, EEG signal matrix X, Laplacian Graph G, total variation matrix V, parameter α and β, λ

OUTPUT: Source matrix S

while S^* is not converged

for $i = 1, \ldots, N$

Alternating update until converge:

$$s_i^{(k+1)} = P^{-1}[L^T x_i - h_i + \rho V^T(y_i^{(k)} - \frac{u_i^{(k)}}{\rho})],$$
$$y_i^{(k+1)} = \text{shrink}(V s_i^{(k+1)} + \frac{u_i^{(k+1)}}{\rho}, \frac{\lambda}{\rho}),$$
$$u_i^{(k+1)} := u_i^{(k)} + \rho(V s_i^{(k+1)} - y_i^{(k+1)})$$

end for

end while

---

where $(x)_+$ is x when $x > 0$, otherwise 0. The shrinkage function is efficient to solve ℓ_1 minimization problem due to its calculation is element-wise. As a result, the updates of $y_i^{(k+1)}$ and $z_i^{(k+1)}$ can be expressed as:

$$y_i^{(k+1)} = \text{shrink}(V s_i^{(k+1)} + \frac{u_i^{(k+1)}}{\rho}, \frac{\lambda}{\rho}), \tag{5.10}$$

The procedure for solving problem (5.4) is summarized in Algorithm (5). The update of all s_i is the most time consuming, however the computation time can be greated reduced by using distributed computation since the updates of s_i is independent within the for loop in Algorithm(5).

5.1.4 Numerical Experiment

A realistic head model called "New York Head" [40] and synthetic data with known ground truth is used for validation of our method. The dimension of lead field matrix is 108 by 2004 for the head model. We sample 1s of the data with 200 Hz frequency from each class or brain status. The number of classes are defined to be 3. A

common source extended patch for all 3 classes with 5 neighboring sources to be activated simultaneously. The discriminative task related source extent for each class also has 5 neighboring sources activated. The magnitude of common source is defined to be 0.8 with a standard derivation of 0.1 and the discriminative source is assigned to be 0.2 with a standard derivation to be 0.05. To mimic the noise from other source locations, we defined the 10 spurious sources with the magnitude to be 0.35 or 0.5 for experiments under different signal noise ratios (SNR). The SNR are defined as $20 \log_{10} \frac{\|S\|_2}{\|N\|_2}$. Under the current experiment settings, the factual activated number of source is 20, according to the result in [20], the recover rate is dropped quickly when the number of dipoles are increased, when the number of activated source is 20, the recover rate is about 40% since the lead field matrix has a very high coherence across columns.
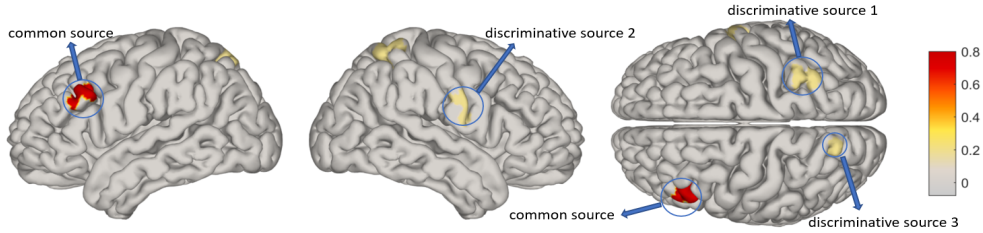
Figure 5.2: Ground truth for all 3 classes aggregated in one figure with a common source and 3 discriminative sources

5.2 Spatial Graph Fractional-Order Total Variation

In pursuit of improving spatial smoothness of source extents, we design a spatial regularization term based on our recent work on graph fractional-order TV [47]. To reduce staircase artifacts of TV, fractional-order TV (also known as total fractional-order variation) has been proposed and widely applied in the image processing community
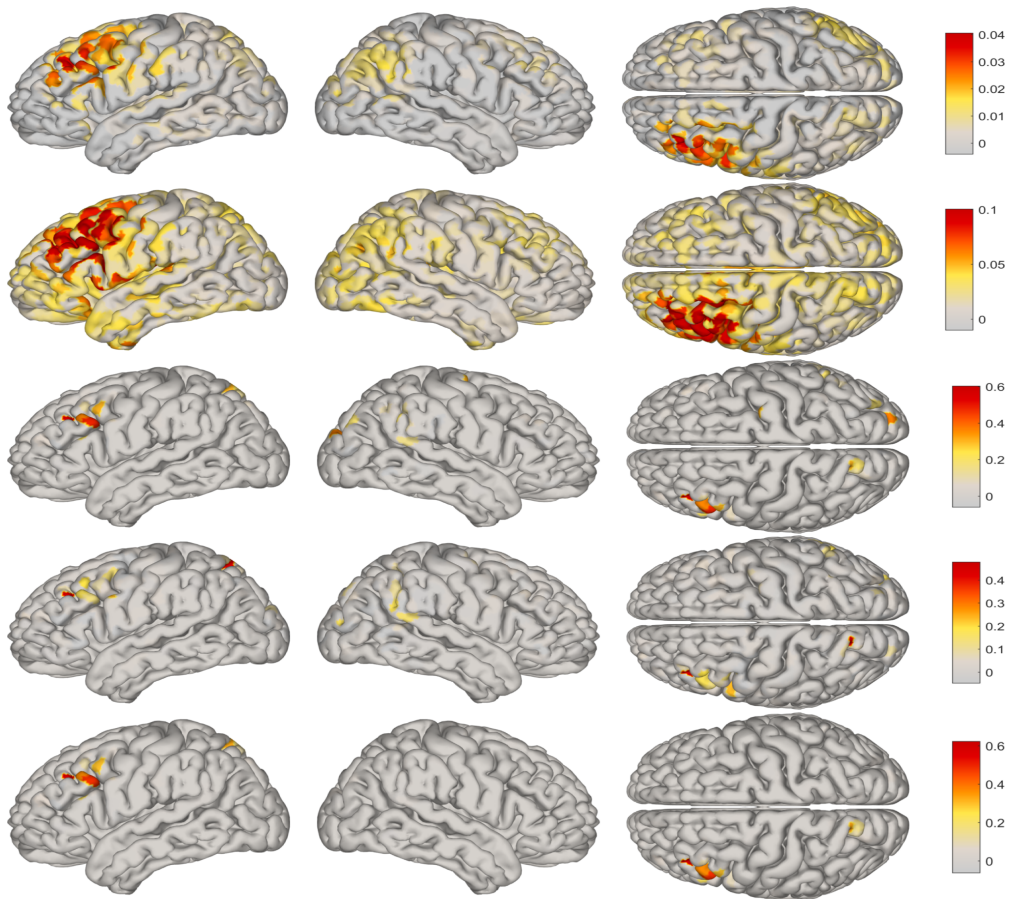
Figure 5.3: Illustration of primary source reconstruction and discriminative source reconstruction by difference methods. The first row is source solution provided by MNE, the second row is from the solution of sLORETA, the third and fourth row are DALM and FISTA method within the MCE framework, the last row is our proposed method. Our method can provide sparse and precise reconstruction of discriminative source.

to improve image smoothness by considering more neighboring information [7, 17, 78]. It is known that the anisotropic fractional-order TV of an image u defined on a 2D rectangular mesh has the following form

$$TV_\alpha(u) = \|\nabla^\alpha u\|_1 = \sum_{i,j=1}^{M} \left(|(D_x^\alpha u)_{i,j}| + |(D_y^\alpha u)_{i,j}| \right),$$

where $\alpha \in (1, 2)$. Here the fractional derivative is based on the Grüwald-Letnikov derivative definition [67]

$$(D_x^\alpha u)_{i,j} = \sum_{k=0}^{K} w_\alpha(k) u(i - k, j),$$

$$(D_y^\alpha u)_{i,j} = \sum_{k=0}^{K} w_\alpha(k) u(i, j - k),$$

where the coefficients are $w_\alpha(k) = (-1)^k \frac{\Gamma(\alpha+1)}{k!\Gamma(\alpha-k+1)}$. Based on this definition, TV_α becomes the traditional TV when $\alpha = 1$. Although valid for $(0, 1) \cup (2, \infty)$, the parameter α is typically set between 1 and 2 to achieve the best performance in practice [17].

Using a triangle mesh, the discretized cortex surface can be treated as a graph with voxel or dipole as graph node. For a specific node v_i, let $d(v_i, v_j)$ be the number of nodes on the shortest path connecting the nodes v_i and v_j, which is in or close to a geodesic of the underlying cortex surface passing through v_i and v_j. Given a path $p = (v_{i=m_0}, v_{m_1}, \ldots, v_{m_K})$ where the shortest distance between v_{m_0} and v_{m_j} is j nodes, the fractional-order derivative along the path p is defined as

$$(D_p^\alpha u)_i := D_p^\alpha u(v_i) = \sum_{j=0}^{K} w_\alpha(j) u(v_{m_j}).$$

The discretized fractional-order TV of u is defined as [47]:

$$TV_\alpha(u) = \|D_\alpha u\|_1 = \sum_{i=1}^{M} \sum_{p \in \mathcal{P}(i;K)} |(D_p^\alpha u)_i|,$$

where $\mathcal{P}(i; K)$ is the set of all paths starting from the i-th node with length of K nodes. Here we use the breadth-first search (BFS) algorithm to first compute the shortest path between each node pair to get a pairwise distance matrix, and then create the matrix $D_\alpha \in \mathbb{R}^{N_p \times D}$ by seeking all N_p paths of length K nodes and recording all nodes on each path. For a specific node v_i, the nodes at level k, i.e., the nodes have shortest distance k from v_i, are assigned the weight $w_\alpha(k)$. Note that K specifies the maximal level of nodes to be used. By the assumption that u has a sparse spatial structure, it is sufficient to use $K \leq 4$ levels of neighboring nodes to achieve the desired accuracy in our experiments.

5.2.1 Proposed EEG Source Imaging Approach

In this section, we present our proposed approach which utilizes the temporal and spatial graph structures of the EEG data to help recognize extended source patches on the cortex and enhance spatial smoothness of source extents. A numerical algorithm is derived by applying the ADMM and an enhanced version based on the derived algorithm called Two-stage Geolocation-based Solution Expansion ADMM (TGSE-ADMM) is proposed.

There has been a large number of work devoted to developing EEG source localization methods by using various regularization techniques, such as Variation-Based Sparse Cortical Current Density (VB-SCCD) [22] which is essentially the TV, In [101], Zhu et al. proposed to use multiple priors including variation-based and wavelet-based constraints. However, based on the assumption that the underlying signal is piecewise constant, TV can easily cause staircase artifacts. To preserve high-order spatial

71

smoothness of the EEG signal defined on the cortex, we use the graph fractional-order total variation described in Section 5.2. On the other hand, previous studies [38, 76] indicated that the brain spontaneous sources contribute most part of the EEG signal. The neurons in our brain still fires even when the subjects are in closed-eye resting state.

By combining the spatial and temporal graph regularizations described in Section 5.2, we propose the following model for EEG discriminative source imaging

$$
\begin{aligned}
&\min_S E(S) + R_s(S) + R_t(S) \\
&= \min_S \frac{1}{2}\|X - LS\|_F^2 + \lambda\|D_\alpha S\|_{1,1} + \frac{\beta}{2}\sum_{i,j=1}^{N}\|s_i - s_j\|_2^2 M_{i,j}
\end{aligned}
\tag{5.11}
$$

where $\beta, \lambda > 0$ are tuning parameters and $\|D_\alpha S\|_{1,1} = \sum_{i=1}^{T}\|D_\alpha s_i\|_1$. Note that an important assumption in EEG source imaging is the prior to guarantee spatiotemporal smoothness in the source solution [16, 26, 43, 54, 83]. Our proposed model is able to enforce high order spatial smoothness via graph fractional-order TV plus temporal smoothness via temporal graph regularization involving label information of brain state.

5.2.2 Proposed Algorithms

To simplify discussion, we first replace the temporal regularization term by (6.4) and rewrite (5.11) as follows

$$
\min_S \frac{1}{2}\|X - LS\|_F^2 + \lambda\|D_\alpha S\|_{1,1} + \beta(\mathrm{tr}(SGS^T)).
\tag{5.12}
$$

By change of variables, (5.12) can be rewritten as

$$
\min_{S,Y} \frac{1}{2}\|X - LS\|_F^2 + \lambda\|Y\|_{1,1} + \beta(\mathrm{tr}(SGS^T)) \text{ s.t. } Y = D_\alpha S.
\tag{5.13}
$$

The new formulation makes the objective function separable with respect to the two variables S and Y. Furthermore, by denoting the i-th column of X and Y by x_i and y_i respectively, we obtain a column-wise form of (5.13)

$$\min_{s_i,y_i} \frac{1}{2}\|x_i - Ls_i\|_2^2 + \lambda\|y_i\|_1 + \beta G_{ii}s_i^T s_i + s_i^T h_i \text{ s.t. } y_i = D_\alpha s_i, \tag{5.14}$$

where $h_i = 2\beta(\sum_{j\neq i} G_{ij}s_j)$ and G_{ij} is the (i, j)-th entry of the matrix G.

ADMM is an efficient method to solve convex and even non-convex problems by decomposing the original problem into several subproblems such that each subproblem has a closed form solution or can be computed efficiently [12]. To apply the ADMM to solve (5.14), we first construct the following augmented Lagrangian function

$$\mathcal{L}(s_i, y_i, u_i) = \frac{1}{2}\|x_i - Ls_i\|_2^2 + \lambda\|y_i\|_1 + \beta G_{ii}s_i^T s_i \\ + s_i^T h_i + u_i^T(D_\alpha s_i - y_i) + \frac{\rho}{2}\|D_\alpha s_i - y_i\|_2^2 \tag{5.15}$$

Then ADMM results in the following two subproblems for updating s_i, y_i:

$$s_i^{(k+1)} = \operatorname*{argmin}_s \mathcal{L}(s, y_i^{(k)}, u_i^{(k)}),$$

$$y_i^{(k+1)} = \operatorname*{argmin}_y \mathcal{L}(s_i^{(k+1)}, y, u_i^{(k)}).$$

The s-subproblem has a least-squares solution

$$s_i^{(k+1)} = \operatorname*{argmin}_s \frac{1}{2}\|x_i - Ls\|_2^2 + \beta G_{ii}s^T s + s^T h_i \\ + \frac{\rho}{2}\|D_\alpha s - y_i^{(k)} + u_i^{(k)}/\rho\|_2^2 \\ = P^{-1}[L^T x_i - h_i + \rho D_\alpha^T(y_i^{(k)} - u_i^{(k)}/\rho)],$$

where $P = L^T L + 2\beta G_{ii}I + \rho D_\alpha^T D_\alpha$. The y-subproblem essentially finds the proximal operator of the ℓ_1-norm, which has a closed form

$$y_i^{(k+1)} = \text{shrink}(D_\alpha s_i^{(k+1)} + u_i^{(k)}/\rho, \lambda/\rho), \tag{5.16}$$

Algorithm 6 Source Imaging Based on Spatial and Temporal Graph Structures

---

INPUT: Lead field matrix L, preprocessed EEG signal matrix X, graph matrix G, precalculated matrix D_α, parameters $\beta, \lambda > 0$, Homotopy solution S_0, and $\kappa > 0$.
OUTPUT: Source matrix S.
Initialize: Set $S^{(0)} = S_0$, $y_i^{(0)} = VS_0$ and $u_i^{(0)} = \kappa \times \mathbf{1}$.
for $t = 1, \ldots, T_{max}$ **do**
    for $i = 1, \ldots, N$ **do**
        while s_i is not converged **do**
$$s_i^{(k+1)} = P^{-1}[L^T x_i - h_i + \rho D_\alpha^T (y_i^{(k)} - u_i^{(k)}/\rho)]$$
$$y_i^{(k+1)} = \text{shrink}(D_\alpha s_i^{(k+1)} + u_i^{(k)}/\rho, \lambda/\rho)$$
$$u_i^{(k+1)} = u_i^{(k)} + \rho(D_\alpha s_i^{(k+1)} - y_i^{(k+1)})$$
        end while
    end for
    update S_t, Y_t
end for

---

where the shrinkage function $\text{shrink}(\cdot, \cdot)$ is defined by

$$\text{shrink}(v, \mu) = (|v| - \mu)_+ \, \text{sgn}(v),$$

where $(x)_+$ is x when $x > 0$, otherwise 0. Here $\text{sgn}(\cdot)$ is the componentwise sign function. The algorithm based on ADMM for solving (5.11) is summarized in Algorithm 6.

Despite its effectiveness, Algorithm 6 is sensitive to the initialization and returns undesirable solutions numerically-either too sparse using the ℓ_1-regularized solution as initial guess or too diffuse using $\mathbf{0}$ as initial guess. To address this issue, we propose a two-stage algorithm based on ADMM and Geolocation-based Solution Expansion (GSE), termed as Algorithm 2, which is empirically shown to be effective in reconstructing large source extents. At the first stage, we run Algorithm 6 with a small graph parameter β to reduce the impact of misleading (initial) solutions from samples of the
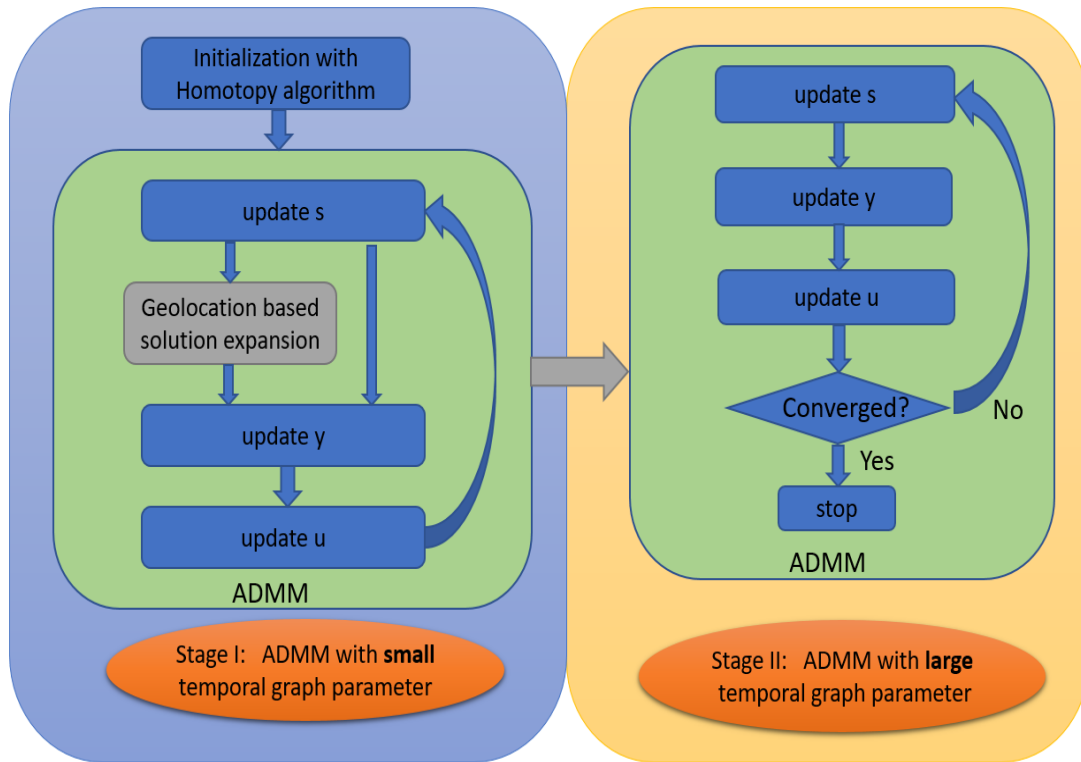
Figure 5.4: Pipeline of Algorithm 2

same class. Here the solution from the homotopy algorithm [93] is set as the initial guess of S. Although Algorithm 6 locates the most desirable source patches and deactivates the wrongly activated sources, the result is prone to have either narrow or flat source extents. To further correct source extents, we perform GSE, i.e., triggering the neighboring sources of ℓ_1 inferred activated sources to give an overestimation at the first few iterations, followed with expanding the solution by finding a large patch of the source extent. An illustration of the effect of GSE is given in Fig.5.5. Then the second stage runs Algorithm 6 with a larger β, which corrects the first stage result by eliminating spurious activated sources. Both stages use Algorithm 6 but with different

75

temporal graph parameters and different initial guesses of S.
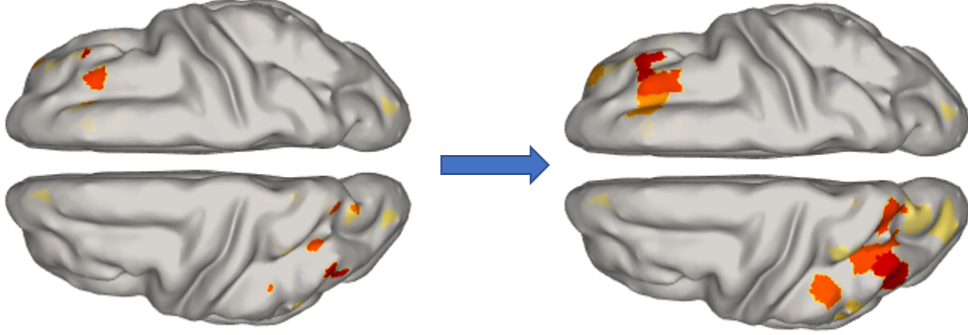
Figure 5.5: Illustration of using GSE to expand sparse discrete solution and produce an over-estimated solution. GSE is done by assigning neighbor voxels the same value as the inferred activated sources.

5.2.3 Numerical Experiment

A realistic head model called "New York Head" [34] is used in our numerical experiment. The lead field matrix is a linear mapping from 2004 sources to 108 electrodes. We use two focal source extents to represent the spontaneous activation pattern shared by different classes and discriminative task-related pattern corresponding to one brain state. To mimic the real world source propagation pattern, one focal source extent is generated with a center source location and neighboring sources with spatial standard deviation along the cortical manifold with $\sigma = 20$ mm. The magnitude of spontaneous center source is 0.8 and the magnitude of task-related center source is 0.5. Both source extents have 15 activated sources by setting other smaller sources to be 0. We also assign 10 randomly selected source with magnitude of 0.35 with variance to be 0.05 to represent spurious sources for each sample. The maximum iteration is set 50 for updating s_i at each stage. We set $\beta = 10^{-5}$ for the first stage and $\beta = 0.1$ for the

second stage. The spatial graph parameter λ is set 10^{-4} to make the data fitting term and the spatial regularization in the same scale. For the GSE operation, we choose 15 sources with largest magnitude, and then assign 5 nearest neighbor sources of them to have the same magnitude starting from the minimum to the largest magnitude of these 15 sources. Fig.5.5 illustrates the effect under the aforementioned setting. The ground truth source activation and reconstructed sources images as well as a brief discussion by different algorithms are summarized in Fig.5.6. In Fig.5.6, the superiority of the proposed two-stage algorithm over sLORETA, MCE, one-stage Algorithm 6 is clearly demonstrated for reconstructing source extents.

For quantitative comparison, we use several metrics including the data fitting r^2, the spatial regularization term R_s defined in (5.11) to measure the spatial smoothness, predicted source precision P= TP/(TP+FP) and sensitivity S=TP/(TP+FN), where TP, FN, FP represents true positive, false negative and false positive respectively. Note that if the predicted source extent has no overlap with the true source extent, both precision and sensitivity is 0. Here P_c and S_c represent precision and sensitivity for the common source, respectively, and P_d and S_d are defined similarly for the discriminative source. We use threshold values 0.35 and 0.25 when calculating sensitivity and accuracy for the common and the discriminative sources for Homotopy, one-stage Algorithm 6 and two-stage Algorithm 2. We also use the mean absolute error (MAE) to measure the discrepancy between the reconstructed source and the ground truth. Table 5.1 summarizes the performance of our proposed algorithm and benchmark algorithms. Since Homotopy and one-stage Algorithm 6 without the GSE operation yield very sparse solutions, their precision is high but with very low sensitivity. sLORETA

has higher sensitivity accuracy than precision due to its diffusiveness. Our proposed method achieves a better balance of precision and sensitivity. Despite of its capability to better explain the data and a smaller spatial regularization term than the proposed result, the result by one-stage Algorithm 6 is very focalized with narrow source extent. The proposed Algorithm 2 corrects the source extent and provides a more useful result in practice.

Table 5.1: Performance Comparison

Algorithm	r^2	R_s	P_c	S_c	P_d	S_d	MAE
sLORETA	0.503	487.7	0.27	0.33	0.14	0.7	84.9
Homotopy	1.000	244.5	0.70	0.19	0.72	0.23	20.0
Algorithm 6	0.979	209.5	0.64	0.20	0.62	0.23	18.6
Algorithm 2	0.976	229.2	0.77	0.54	0.82	0.93	16.8

5.3 Conclusion

In the first part of this chapter, we proposed a model called VB-SCCD-graph which has the advantage to better find the task related activation source extents than traditional method. The proposed ADMM algorithm is given to solve the VB-SCCD-graph model with better performance validated in the numerical experiments. One of the drawbacks for the proposed framework is the total variation term only allow smoothness for the first spatial derivative, and this problem is solved by using graph fractional order TV, which is introduced in the second part of this chapter. In the second part, we propose a novel EEG source imaging model using the spatial graph fractional-order TV and the temporal graph regularization involving label information of brain state. The model is solved efficiently by an ADMM-based algorithm. To further correct source extents, a two-stage algorithm is proposed to combine geolocation-based solution expansion. Numerical experiments have demonstrated that the proposed method can pre-
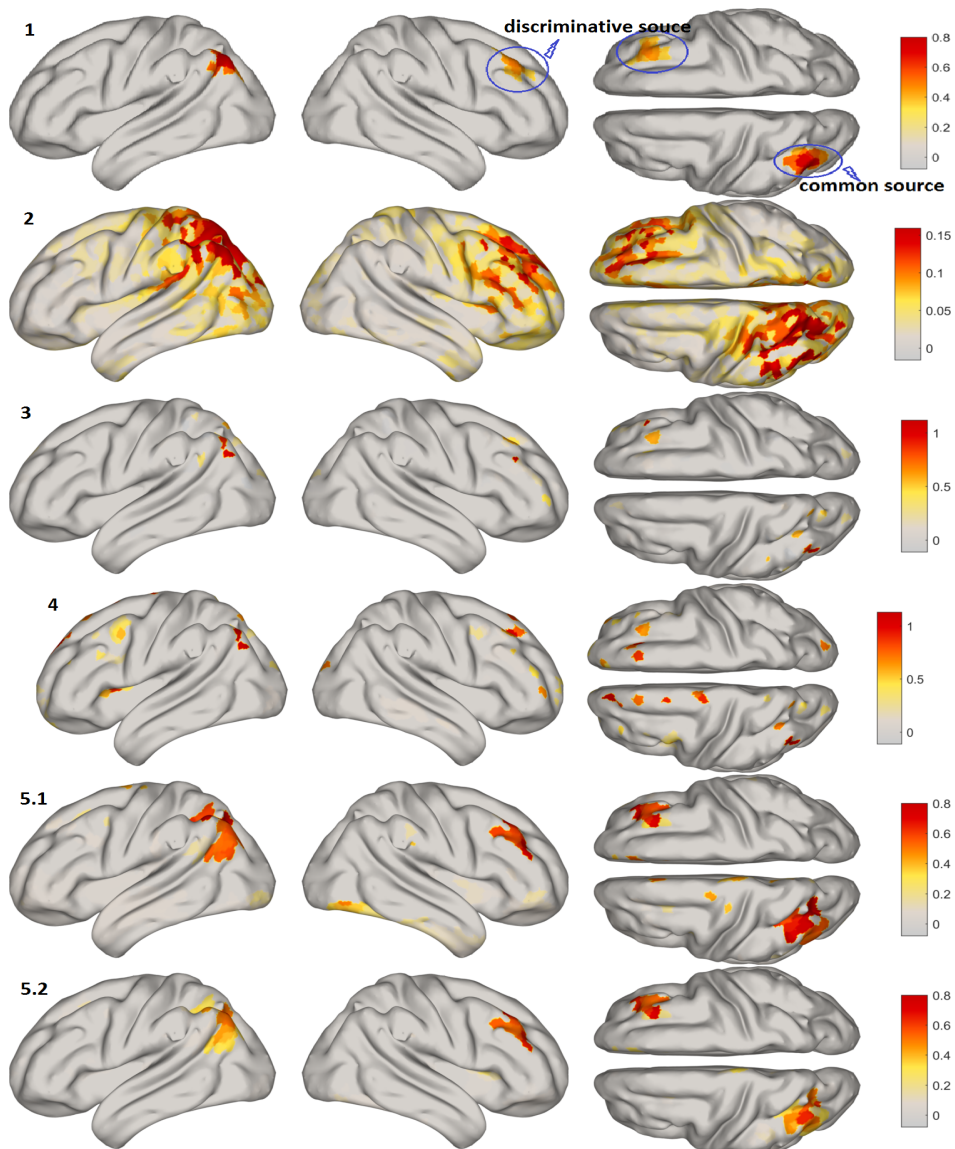
Figure 5.6: Ground truth source activation and reconstructed sources by difference algorithms. The top row is ground truth activation pattern. The 2nd row is the sLORETA solution, the 3rd row is the ℓ_1-regularized solution based on the Homotopy algorithm, the 4th row is the one-stage Algorithm 6 solution without GSE, and the row denoted as 5.1 is the solution after the first stage of the proposed algorithm, the row denoted as 5.2 is our final proposed solution. The sLORETA gives over-diffuse and inaccurate solution. Algorithm 6 with the ℓ_1-regularized solution as initial guess gives a very sparse solution. The proposed two-stage algorithm produces the best solution, where spurious activated sources at the first stage are eliminated at the second stage.

serve high-order spatial smoothness and intra-class consistency, which shows the great potential to achieve high resolution EEG source localization for real-time non-invasive brain imaging research.

Chapter 6

EEG Source Imaging with Graph Regularized Temporal Smooth Low Rank Representation

6.1 Introduction

In the literation review chapter, we introduced different algorithms for ESI problem. One common drawback of the existing ESI algorithms is that they have more discussion on the noises in the sensor level and the studies about spurious noise in the source space is lack in the literature. If perfectly reconstructed, the estimated source is aggregated by task-related source and spurious noise in the source space. The true task-related sources will be corrupted by spurious sources, which motivates us to develop new algorithms to find true task-related source. There are two commonly accepted assumptions (1) spatially sparse (2) temporally continuous for the task-related source activation pattern, which inevitably leads to the low-rank property of the source space. To better discover the task-related source, we impose the low-rank term in the goal function as we consider it is a more direct constraint for spatial sparse. Also, we use a more direct penalty term to temporal smoothness, which is to penalize dissimilarity of temporally neighboring samples based on manifold graph embedding. It is worth-noting that we used the graph regularization term in our previous chapter, however the graph is defined to be fully connected for all the points within one class [50], which inevitably drive all the activate patterns at different time points having the same mag-

nitude, thus making the previously defined graph regularization term rely on a strong assumption and limit its future application for realistic cases.

In this chapter, we propose a novel EEG source imaging model based on temporal graph regularized low-rank representation. The model is solved based on the alternating direction method of multipliers (ADMM) [12]. We conducted extensive numerical experiments to verify the effectiveness on discovering task related low-rank sources. The reconstructed solution is temporally smooth and spatially sparse. The contributions of this chapter are summarized as follows:

1. We propose to consider the noise not only in the sensor level, but also in the source space.

2. A low-rank representation model (LRR) is proposed for the first time on EEG inverse problem inspired by the low-rank property of true task-related source configurations.

3. We redefined graph embedding regularization based on our previous chapter that utilizes temporal vicinity information of samples to promote temporal smoothness.

4. A new algorithm based on ADMM is given which is capable of extracting the low-rank task-related source patterns.

6.2 Inverse Problem and Temporal Graph Structures

In this section, we briefly review the inverse problem and then discuss the design of temporal graph regularization.

6.2.1 The Inverse Problem

The cortex source activations propagate to EEG sensors through a linear mapping matrix called lead field matrix, and it can be described as the following linear model:

$$X = LS + E \tag{6.1}$$

where $X \in \mathbb{R}^{N_c \times N_t}$ is the EEG data measured at a set of N_c electrodes for N_t time points, $L \in \mathbb{R}^{N_c \times N_d}$ is the lead field matrix which maps the source signal to sensors on the scalp, each column of L represents the electrical field of a particular source to the EEG electrodes, $S \in \mathbb{R}^{N_d \times N_t}$ represents the corresponding driving potential in N_d sources locations for the N_t time instants. Since the number of sources is much larger than electrodes, solving S given X is ill-posed with infinite feasible solutions, which necessitates a regularization term to be imposed. Generally, an estimate of S can be found by minimizing the following cost function, which is composed of a quadratic error and a regularization term:

$$\arg \min_S \|E\|_F^2 + \gamma \Theta(S) \quad s.t. \quad X - LS = E, \tag{6.2}$$

where $\|\cdot\|_F$ is the Frobenius Norm. The penalty term $\Theta(S)$ is to encourage neurophysiologically plausible solutions. The regularization term take the form of ℓ_2, ℓ_1 or mixed

norm. For example, spatially smooth formulation as in LORETA estimation or spatially sparse formulation with Least Absolute Shrinkage and Selection Operator (LASSO) estimate.

6.2.2 Temporal Graph Embedding

An important assumption on the source signal is that two temporal adjoint data points should have similar intrinsic activation pattern. In computer vision community, a lot of manifold learning methods have been proposed to find intrinsic similar structure on low-dimensional sub-manifolds embedded in a high dimensional ambient space, such as locally linear embedding [79], Locality Preserving Projection [37], Neighborhood Preserving Embedding [36]. A graph can be viewed as geometric neighborhood relationship between each vertex representing each data sample, the weight between vertex represents similarity between two points [97]. Inspired by the manifold theory [14] and work from Liu et al [55], we use a regularization term to penalize the difference of two neighboring source signal. In our previous work, we use a graph regularization term to promote intra-class consistency [50], but the assumption is too strong by requiring all the reconstructed sources at different time points has the same location as well as signal magnitude as long as they belong to the same class. Now define a temporal graph regularization as

$$R_t(S) = \sum_{i,j=1}^{N} \|s_i - s_j\|_2^2 W_{ij}, \tag{6.3}$$

where s_i is the i-th column of the matrix S, and a binary matrix W is designed as follows

$$W_{ij} = \begin{cases} 1, & \text{if } s_i \in N_k(s_j) \text{ or } s_j \in N_k(s_i) \\ 0, & \text{otherwise.} \end{cases}$$

The graph embedding matrix W contains temporal vicinity information. $N_k(s_i)$ is the set containing k temporally closest points to s_i. This formulation intends to force neighboring source signal having similar pattern. The benefits are twofold, one is for temporal smoothness, another advantage is to make the reconstructed source denoised for intermittent spurious source activates. By defining D as a diagonal matrix whose entries are row sums of the symmetric matrix W, i.e., $D_{ii} = \sum_j W_{ij}$, and denoting $G = D - W$, $R_t(S)$ can be rewritten as:

$$\begin{aligned} R_t(S) &= \sum_{i,j=1}^{N} (s_i{}^T s_i + s_j{}^T s_j - 2s_i{}^T s_j) W_{ij} = \sum_i^N s_i^T s_i w_{ii} - \sum_{i,j=1}^N s_i^T s_j w_{ij} \\ &= 2\operatorname{tr}(SDS^T) - 2\operatorname{tr}(SWS^T) = 2\operatorname{tr}(SGS^T), \end{aligned} \qquad (6.4)$$

where $\operatorname{tr}(\cdot)$ is the trace operator of a matrix, i.e., adding up all diagonal entries of a matrix.

6.3 Proposed EEG Source Imaging Model

Before we present our low-rank model with temporal graph structures, we comment on the limitations of traditional model and come up with the decomposition of task-related source with low-rank property and spontaneous non-task-related spurious sources that is sparsely distributed spatially and with transient patterns. We come up with a graph regularized low-rank representation model and detailed discussion on the purpose of each term in the goal function.

85
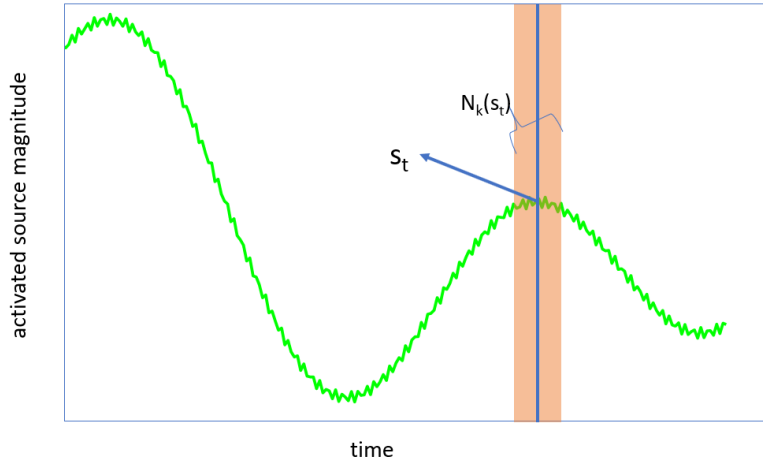
Figure 6.1: Illustration of temporal smoothness. By design the temporal graph matrix G, the reconstructed signal should have consistent pattern within the same neighborhood window.

6.3.1 Decomposition of True and Spurious Sources

In general, two types of noises should be considered, one originates from inaccurate measurement of the sensors modeled by Guassian white noise, which is denoted as E in Eq.(6.1), the other type of noise is called biological noise that comes directly from the spontaneous activations in the source space, which are not task-related and termed as spurious source. The second types of noise (spurious source) also contributes to the EEG signal in the same way as ground truth source. A drawback of traditional models is that they didn't distinguish the spurious sources from the true sources, and the estimated source can be composed of both task-rated source and spurious sources. To address the above mentioned problem, we propose to use a decomposed source spaces, composed of a low-rank source space and spurious sources originates from spontaneous biological noises. The illustration of decomposition of source space as well as the whole

procedure is given in Fig.6.2, where S_1 has a low-rank property and S_2 is sparse, and sum of S_1 and S_2 is no long low-rank, making X lose low-rank structure.
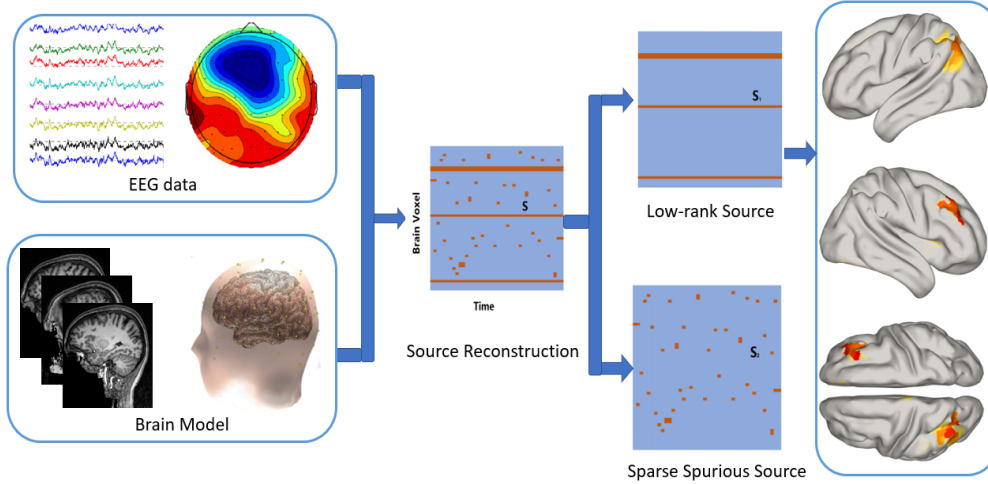
Figure 6.2: Extraction of low-rank true source from spurious source pipeline: After gathering the MRI scans of the head, tissue segmentation is conducted followed by mesh generation. By assigning conductivity values to different tissues and electrodes co-registered with the meshing model, boundary element method (BEM) was used to solve the forward model. Each triangle represents a brain source, the direction of the source is assumed to be perpendicular to the triangular surface. With EEG data and forward brain model, source reconstruction is calculated. The factual source signal S can be decomposed into two source matrix. The task related true sources S_1 have a low-rank property and the spurious sources S_2 are the sparse but not temporally consistent. The low-rank source solution is projected to cortex voxels to illustrate the activation pattern.

6.3.2 Basic Low-Rank Representation (LRR) Model

We argue that during a short period of task-related Evoked Repose Potential (EPR), the number of corresponding activated sources is sparse and remain activated during this period of time, which makes the EPR source matrix low-rank with most

rows being zero. However, the brain signal is known to be heavy noisy, spontaneous activations are also active from different source spots. The low-rank representation model for the EEG inverse problem is introduced as follows:

$$\min_{S,E} \text{rank}(S) + \beta\|S\|_{1,1} + \lambda\|E\|_{1,1}$$
$$\text{s.t.} \quad X = LS + E,$$

(6.5)

where β, λ and γ are positive scalars to balance the rank function, sparsity cost of sources and the reconstruction error. It is pointed out that ℓ_1 on the error term is more robust to outliers, we use ℓ_1 in the row-rank model [53]. The $\|E\|_{1,1}$ is defined as $\sum_j \sum_i |E_{ij}|$. Due to the discrete nature of the rank function, it is a common practice to use a surrogate nuclear norm $\|\cdot\|_*$ instead. The goal function is given as:

$$\min_{S,E}\|S\|_* + \beta\|S\|_{1,1} + \lambda\|E\|_{1,1}$$
$$\text{s.t.} \quad X = LS + E,$$

(6.6)

The above formulation is a simple version trying to estimate the task-related source activation pattern by using low-rank constraint. To promote the temporal smoothness, the Laplacian graph structure is included in the next section followed by the optimization algorithm.

6.3.3 LRR Model with Graph Regularization

Incorporating the previous temporal graph structures, we introduce our proposed model called low-rank representation with temporal graph structures ESI (LRR-TG-ESI). The model is composed of data fitting term to explain the EEG data, temporal graph embedding regularization term that promote temporal smooth, and a ℓ_1 norm for sparsity penalty and nuclear norm for the low-rank structure of ground true source. By

combining the low-rank prior and the temporal graph regularization, we propose the following model for ESI:

$$\min_{S,E} \|S\|_* + \lambda \|E\|_{1,1} + \beta \|S\|_{1,1} + \alpha \operatorname{tr}(SGS^T)$$
$$\text{s.t.} \quad X = LS + E, \tag{6.7}$$

where $\lambda, \beta, \alpha > 0$ are tuning parameters to balance the trade-off of different terms. Our proposed model is able to enforce row-sparse via low-rank prior and temporal smoothness via temporal graph regularization while fitting the EEG data X. Compared to earlier works on the ESI problem, both the low-rank prior and graph regularization is novel, although the graph regularization term has been discussed in our early paper [50], but it is not defined on the temporal manifold, and the previous definition in [50] make the magnitude of source signal to be equal intra-class, which is not realistic in real world. To further consider the spatial smoothness, a total variation term can be imposed as another penalty term, such as first order total variation (TV) regularization in Ref. [22, 65], fractional order TV in [47, 75], and similar algorithm can be derived under the framework of ADMM, however further investigation with constraints of TV is our future work.

6.4 Numerical Algorithm

To solve (6.7), an algorithm in the ADMM framework is developed. The augmented Lagrangian function of (6.7) is

$$L(S, M, E, T_1, T_2, \mu) = \|S_1\|_* + \lambda\|E\|_{1,1} + \beta\|M\|_{1,1} + \alpha \operatorname{tr}(SGS^T)$$
$$+ \langle T_1, X - LS - E \rangle + \langle T_2, M - S \rangle + \frac{\mu}{2} \times (\|X - LS - E\|_F^2 + \|M - S\|_F^2) \tag{6.8}$$

By some simple algebra, (6.8) can be reformulated as

$$L(S, M, E, T_1, T_2, \mu) = \|S\|_* + \lambda\|E\|_{1,1} + \beta\|M\|_{1,1} + \alpha \operatorname{tr}(SGS^T) + \frac{\mu}{2} \times (\|X - LS - E + \frac{T_1}{\mu}\|_F^2$$
$$+ \|M - S + \frac{T_2}{\mu}\|_F^2) - \frac{1}{2}\mu(\|T_1\|_F^2 + \|T_2\|_F^2), \tag{6.9}$$

where T_1 and T_2 are Lagrangian multipliers and μ is a parameter for the augmented Lagragian term. The variables are updates alternately in a Gauss-Seidel manner by minimizing the augmented Lagrangian function, with other variables fixed. For symbolic simplicity, we rewrite Eq.(6.9) into the following form:

$$L(S, M, E, T_1, T_2\mu) = \|S\|_* + \lambda\|E\|_{1,1} + \beta\|M\|_{1,1}$$
$$+ h(S, E, M, T_1, T_2, \mu) - \frac{1}{2}\mu(\|T_1\|_F^2 + \|T_2\|_F^2), \tag{6.10}$$

where

$$h(S, E, M, T_1, T_2, \mu) = \alpha \operatorname{tr}(SGS^T) + \frac{\mu}{2} \times (\|X - LS - E + \frac{T_1}{\mu}\|_F^2 + \|M - S + \frac{T_2}{\mu}\|_F^2).$$

If the augmented Lagrangian function is difficult to minimize with respect to a variable, a linearized approximate surrogate function can used, hence the algorithm bears the

name Linearized Alternating Direction method [48, 97]. Updating S by minimizing $h(S, E^k, M^k, T_1^k, T_2^k, \mu^k)$ (suppose we are at iteration k) is equivalent to minimize the following goal function with the other variables fixed:

$$L_S = \|S\|_* + h(S, E^k, M^k, T_1^k, T_2^k, \mu^k), \tag{6.11}$$

which is approximated by optimizing its linearizion at S_1^k plus a quadratic proximal term, given as:

$$S = \underset{S}{\operatorname{argmin}} \|S\|_* + \langle \nabla_S h(S^k), S - S^k \rangle + \frac{\eta}{2} \|S - S^k\|_F^2. \tag{6.12}$$

Here η is a constant satisfying

$$\eta > 2\alpha \|G\|_2 + \mu(1 + \|L\|_2^2), \tag{6.13}$$

where $\|\cdot\|_2$ is the spectral norm of a matrix, i.e, the largest singular value. As long as (6.13) is satisfied, (6.12) is a good approximate to (6.11). The solution to (6.12) has a closed form using a singular value thresholding operator (SVT) [15] given as:

$$S^{k+1} = \Theta_{\eta^{-1}}(S^k - \nabla_S h(S^k)/\eta), \tag{6.14}$$

where $\Theta_\varepsilon(A) = U S_\varepsilon(\Sigma)V^T$ is the SVT operator, in which $U\Sigma V^T$ is the singular value decomposition of A and $S_\varepsilon(s)$ is defined as $\sin(x)\max(|x| - \varepsilon, 0)$. $\nabla_{S_1} h(S_1^k)$ is calculated as

$$\nabla_S h(S^k) = \alpha(S^k G + S^k G^T) + \mu L^T (LS - X + E - \frac{T_1}{\mu}) + \mu(S - M - \frac{T_2}{\mu}) \tag{6.15}$$

91

To update M and E, it is equivalent to solve the following problem:

$$\underset{M}{\text{argmin}} \frac{\mu}{2}\|M - S + \frac{T_2}{\mu}\|_F^2 + \beta\|M\|_{1,1} \qquad (6.16)$$

$$\underset{E}{\text{argmin}} \frac{\mu}{2}\|X - LS - E + \frac{T_1}{\mu}\|_F^2 + \lambda\|E\|_{1,1} \qquad (6.17)$$

The general form of (6.16)–(6.17) is a ℓ_1 norm proximal operator defined as

$$\text{prox}_\mu(V) = \arg\min_X \mu\|X\|_{1,1} + \frac{1}{2}\|X - V\|_F^2, \qquad (6.18)$$

with $\mu > 0$. The above problem (6.18) has a closed form solution, called soft thresholding, defined by a shrinkage function,

$$\text{shrink}(V, \mu) = (|V| - \mu)_+ \text{sgn}(V),$$

where $(x)_+$ is x when $x > 0$, otherwise 0. The shrinkage function is defined as element-wise operator. Problem (6.16)–(6.17) has a close form solution described with the shrinkage function. After updating all the variables, these Lagrange multipliers are updated by

$$\begin{aligned} T_1 &= T_1 + \mu(X - LS - E) \\ T_2 &= T_2 + \mu(M - S). \end{aligned} \qquad (6.19)$$

The parameter μ is updated by $\mu = \min(\rho\mu, \mu_{max})$. A summarized algorithm is given as Algorithm 1. We initialize the S with the estimate S_0 from ℓ_1 solver.

It's worth noting that the data fitting term we use is $\ell_{1,1}$ norm of E in the model, and there are other options. Generally, if the Gaussian noise E is small, then the norm $\|E\|_F$, is an appropriate choice, but for random data corruption, $\ell_{1,1}$ should be used, and

Algorithm 7 Source Imaging Based on Spatial and Temporal Graph Structures
_____
    INPUT: Lead field matrix L, preprocessed EEG signal matrix X, graph matrix G,
    precalculated matrix D_α, parameters $\alpha, \zeta > 0$, and $\beta > 0$.
    OUTPUT: Source matrix S.
    Initialize: Set $S = S_0, J = 0, M = 0$.
    while not converged **do**
        update S according to
         $S^{k+1} = \tilde{\Theta}_{\eta^{-1}}(S^k - \nabla_S h(S^k)/\eta)$,
        update M according to Equation (6.16),
        update E according to Equation (6.17),
        update T_1, T_2 according to Equation (6.19),
        update $\mu = \min(\rho\mu, \mu_{max})$,
    end while
_____

for sample specific data corruption, $\ell_{2,1}$ [24, 66, 98], should be used. It has been shown

that $\ell_{2,1}$ is more robust to large outliers in some samples. Although the norm used in

Algorithm 1 is $\ell_{1,1}$, it can be extended to $\ell_{2,1}$ norm of E, where $\|E\|_{2,1}$ is defined as

$$\|E\|_{2,1} = \sum_{i=1} \sqrt{\sum_{j=1} E_{ij}^2}.$$

In stead of solving (6.17) to update E, the following goal function (6.20) needs to be

solved to update E.

$$\operatorname*{argmin}_{E} \frac{\mu}{2}\|X - LS - E + \frac{T_1}{\mu}\|_F^2 + \lambda\|E\|_{2,1} \tag{6.20}$$

By substituting $K = X - LS + \frac{T_1}{\mu}$, if E^* is the optimal solution of

$$\min_{E} \frac{\lambda}{\mu}\|E\|_{2,1} + \frac{1}{2}\|E - K\|_F^2 \tag{6.21}$$

Based on the Lemmas in Ref [94], the solution to (6.21) is

$$e_i^* = \begin{cases} \frac{\|k_i\|_2 - \lambda/\mu}{\|k_i\|_2} k_i, & \text{if } \lambda/\mu \leqslant \|k_i\|_2, \\ 0, & \text{otherwise,} \end{cases}$$

where e_i^* and k_i is the i-th column of matrix E^* and K respectively.

Convergence: The convergence of Algorithm 1 can be easily derived from [48]. Even though the update of M and E is separated in Algorithm 1, they can be combined in one step to become a larger block step and simultaneously solving for (M, E) which is the same case described by LADMAP algorithm [48]. The convergence analysis in [48] can be applied to our case, thus the algorithm convergence is guaranteed [97].

6.5 Numerical Experiments

In this section, we conducted several experiments to illustrate the effectiveness of our proposed method. Since both the nuclear norm and the graph regularization is relative new for the ESI problem, we started from the simple model (6.6) to help the readers understand the property and impacts of low-rank prior along with data fidelity term and sparsity term for source reconstruction. In the first experiment, we did a comprehensive exploration for different parameter settings by varying the weights between low-rank term, data fitting term and sparsity term. In the second experiment, we illustrate the temporal smoothing functionality of the graph regularization term for uncorrupted smooth source and corrupted source with abrupt signal jumps. In the third experiment, we give comprehensive numerical results by testing our algorithm against the benchmark algorithms to showcase the effectiveness of the proposed method in reconstructing task-related source, where we show that our algorithm can not only find

the activated locations, but also reconstruct the time-course of source activation with high precision.

6.5.1 Head Model

A realistic head model, referred to as New York Head model [40], is used in our numerical experiment. The New York Head model is based on highly detailed MRI images derived ICBM152 anatomy, which is a nonlinear average of the T1-weighted structural MRI of 152 adults and calculated with state-of-the-art finite element electrical modeling. The New York Head model is considered to be highly accurate since it considers six tissue types when conducting segmentation, which is scalp, skull, CSF, gray matter, white matter, air cavities, with a native MRI resolution of 0.5 mm^3. The dimension of the lead field matrix used in the numerical experiment part is 2004 by 108, representing a linear mapping from 2004 sources to 108 electrodes.

6.5.2 Experiment 1: Test on Simple Low-rank Model

To understand the property of low-rankness, we start from a simple model to help the readers understand the property of low-rank in the EEG source imaging and the validity of low-rank when recovering the accurate location as well as time course of source signal. Like in [34], eight octants are divided as regions of interest (ROI) are considered, which are Right Anterior Inferior (RAI), Right Anterior Superior (RAS), Right Posterior Inferior (RPI), Right Posterior Superior (RPS), Left Anterior Inferior (LAI), Left Anterior Superior (LAS), Left Posterior Inferior (LPI), Left Posterior Superior (LPI). In the simple experiments, we selected 2 different ROIs and randomly select

one activated voxel in each of these ROIs, and a $4th$ order moving average time series is generated, as illustrated in Fig.6.3.
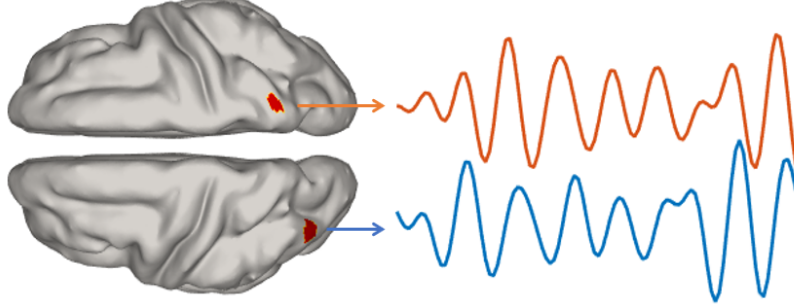
Figure 6.3: Illustration of two activated sources time series on two different ROIs.

At each location, a time series with length of 500 were generated to represent the source activation time-course. At each time point, two randomly picked sources are activated to simulate the non-task related spurious noise with mean of 0 and variance to be 1. The task-related activate pattern has low-rank property, however, the noise corrupted source space is no longer low-rank. We repeated our experiment 50 times for all the combinations of λ and β, where $\lambda = \{0.01, 0.02, 0.03, 0.05, 0.1, 0.2, 0.5\}$ and $\beta = \{0.005, 0.01, 0.015, 0.02, 0.05, 0.1\}$. The reconstructed error (RE) metric used here is

$$\text{RE} = \|\hat{S} - S\|_2 / \|S\|_2, \tag{6.22}$$

where $\hat{S}$ represents the reconstructed source. We define the SNR $= 10 \log_{10} \frac{P_s}{P_n}$, where P_s and P_n are the power of signal and noise respectively. The violin plot is used to visualize the distribution of reconstruction errors, in corresponding to β and λ respectively in Fig.6.4a and Fig.6.4b. Increasing β will penalize the strength of signal and make the

reconstruction error to be large when λ is small. However, When λ is set to be 0.5, the weight of data fidelity is high, thus driving the solution have a better data fidelity, which can balance off the increase of β.

(a)   (b)
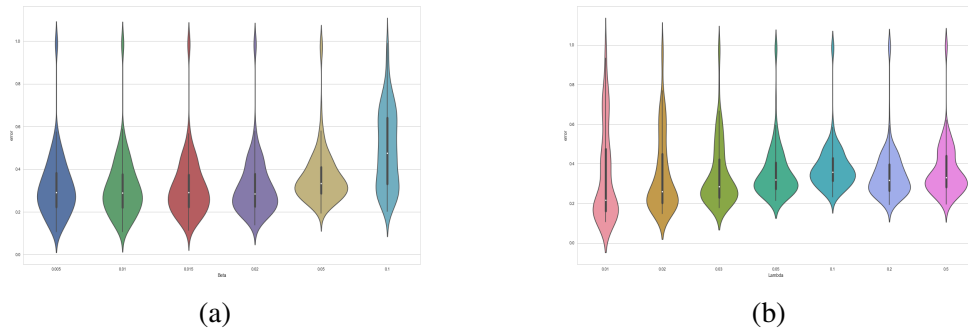
Figure 6.4: Averaged reconstruction error and rank varying (a) λ and (b) β over 50 experiments.

The averaged reconstruction error of 50 experiments for all of β and λ is given in Fig.6.5a and the averaged rank for the estimated source for all the combination of β and λ is given in Fig.6.5b. As we increase the value of λ, the rank is also increasing, which underlies the trade-off between explaining the data and finding the latent low-rank structure of the source space. Increasing λ means more weight on the data fitting term, and the spurious source can also be recovered, thus increasing the rank of the reconstructed source.

To empirically understand and explain the reconstruction error in Fig.6.5a, we visualize the curve fitting performance for truth source time series and the reconstructed source time-course corresponding to different level of reconstruction error. We picked the curve fitting cases when the reconstructed error is 0.2, 0.4, 0.8 and 1 respectively. For error equal to 0.2, we picked one experiment and plot the fitting of time series which

97

(a)	(b)
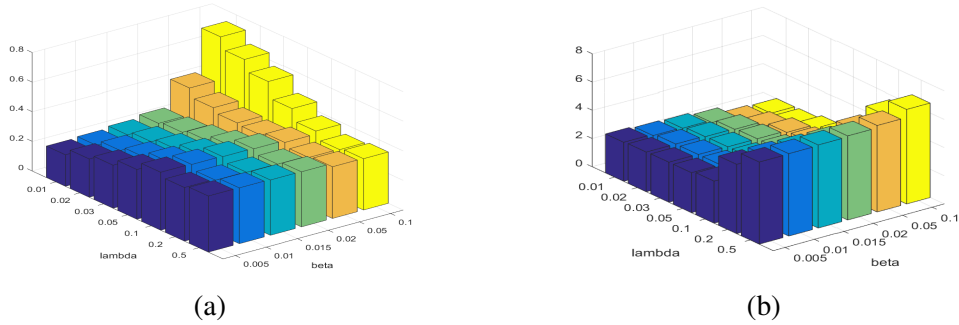
Figure 6.5: Averaged reconstruction error and rank varying λ and β over 50 experiments.(a) average of reconstruction error for different λ and β (b) average of rank for the source matrix S. Increasing λ means more weight on data fidelity and the rank becomes higher. Our model works well with a wide range of parameter setting.

demonstrated a very good curve fitting of the ground truth vs the reconstructed one as is shown in part (a) of Fig.6.6. Also we picked another experiment whose error equal to 0.4 and it is shown in part (b) of Fig.6.6. The curve fitting is slightly worse than the previous one but it is hard to notice the difference compared to the previous one, however according to our error metric, the error is 0.4. One thing to notice is that in both situations, the reconstructed rank equal to the ground truth rank, which is equal to 2, moreover, the estimated two active source location is exactly the ground true locations. We also examined the case when error is up to 0.8, and the curve fitting plot is given in part (c) of Fig.6.6. We examined this happened when we set $\lambda = 0.01$ and $\beta = 0.1$. In this case, the penalty for sparsity is 0.1, which means too much penalty for the sparse term and the signal magnitude is reduced by the shrinkage operation. We also notice than in the experiment, the error can be up to 1 no matter what parameter settings are given, as can be seen in the top region of Fig.6.4a and Fig.6.4b. The curve fitting plot for the failed case is given in part (d) of Fig.6.6.

98
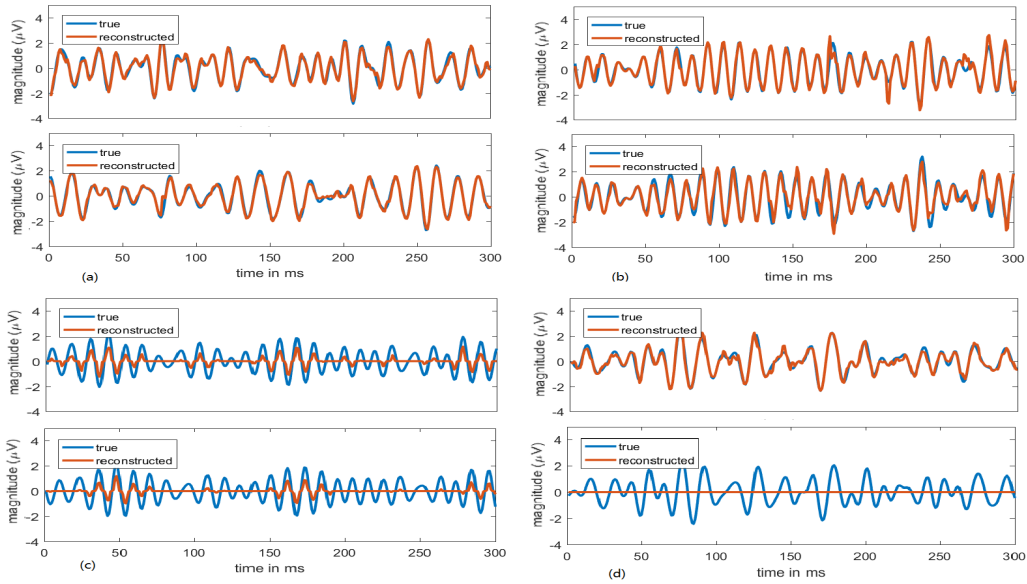
Figure 6.6: Source time course fitting illustration: (a): ground truth time course vs reconstructed for two activated source at different ROIs in one experiment when fitting error equal to 0.2. Here $\lambda = 0.02$ and $\beta = 0.005$.(b): ground truth time course vs reconstructed for two activated source when fitting error equal to 0.4. Here $\lambda = 0.5$, $\beta = 0.01$. (c): ground truth time course vs reconstructed for two activated source when fitting error equal to 0.8. Here $\lambda = 0.01$ and $\beta = 0.1$. (d): ground truth time course vs reconstructed for two activated source when fitting error equal to 1. Here $\lambda = 0.02$ and $\beta = 0.01$. The curve fitting of (b) is slightly worse than (a), corresponding to the RE= 0.2 and RE= 0.4. When the sparsity parameter is set too large, the reconstructed magnitude is smaller than the ground truth as is shown in (c). For some cases, only the time course in one source location is reconstructed shown in (d) with RE to be 1.0.

Although the situation is very rare when $RE = 1$, we want to visualize the activation pattern on the cortex to see how discrepant the reconstructed location compared to the true source location. For comparison, Fig. 6.7 is given when $RE = 0.4$ and $RE = 1$. The reconstructed source locations on two ROIs are exactly the same with the ground true location when $RE = 0.4$, when $RE = 1$, one source location is reconstructed perfectly while the other source location is not accurately located, however the neighboring sources are reconstructed.

To check how the rank of S evolve during the iterations, the boxplot of the rank at selected steps are given in Fig.6.8. Starting from an initial value with high rank, the rank of $\hat{S}$ is decreasing as the iteration proceeds. We set the maximum rank to be 20, during the iteration process, the rank of S is converged to very small number for most of the cases.

6.5.3 Experiments 2: Test LRR with Temoral Graph Prior

In this section, we solve the LRR-TG-ESI problem (6.7) with graph regularization term to test its impact on the reconstructed signal. Under the same setting with Experiment 1, we assign different values $\{0.01, 0.02, 0.05, 0.1, 0.5\}$ for the graph regularization parameter α. The original source signal was smooth, then it was corrupted with randomly number at some time points. There are also 2 randomly picked activated sources representing spurious sources with mean of 0 and variance to be 1. The "temporal smoothing" impact of the graph regularization is shown in Fig.6.9, where $\lambda = 0.02$ and $\beta = 0.01$. In Fig.6.9, the original signal is corrupted and not smooth at some time points, we set the neighbor size to be 2 (the closest signal before and after
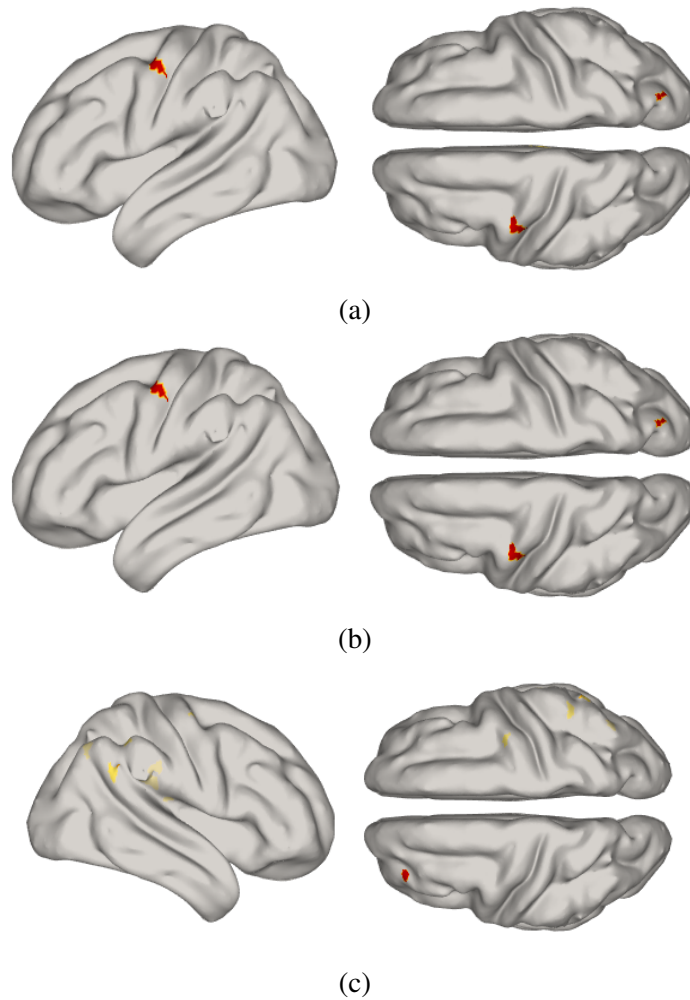
Figure 6.7: (a) Ground truth source activation pattern (b) Reconstructed source activation when 0.4. This plot illustrates the perfect localization of ground true sources. (c) Reconstructed source activation when RE is 1. This plot illustrates when our algorithm failed to recover one of the the exact locations of two activated sources, while the other one can be recovered perfectly. the pictures on the left is the reconstructed location, but still close to the ground truth.

101
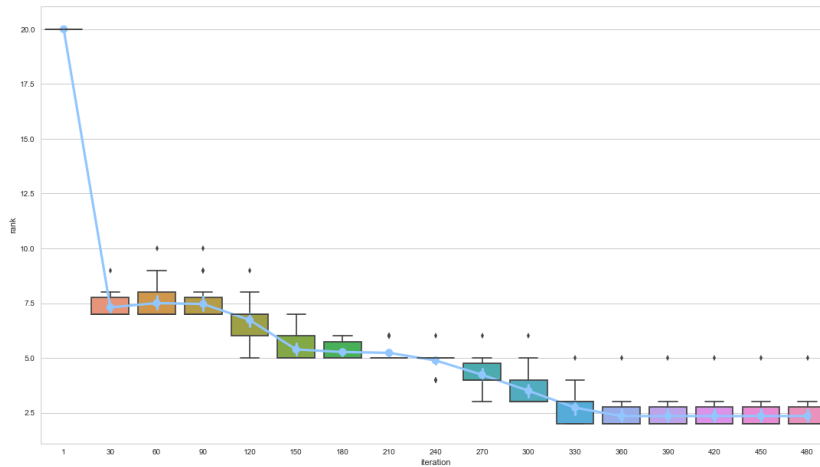
Figure 6.8: Convergence of rank of S during iteration procedure: In the first iteration, we set the maximum rank to be 20, and in most case the rank will converge to 2.

the one to be estimated) when calculating the Laplacian matrix. It is evident from the formulation (6.3) that the graph regularization term will decrease the dissimilarity of temporally neighbored reconstructed source. If α is set to be 0.5, the graph regularization term penalized heavily on the curvature of the reconstructed signal as is illustrated in Fig.6.9. We can see that with the temporal graph prior, the reconstructed source is more smooth. It is worth noticing that the main purpose of temporal graph prior is not to smooth the time course for the activated locations, the main purpose is to filter out the spurious activations that are short transients with abrupt jumps. Combined with the low-rank prior, the temporal graph prior can filter the spurious activations and reconstruct the task related activated source. The randomly planted spurious sources are filter out by penalizing the graph regularization and nuclear norm, and in most of the cases, the final rank is 2 can be achieved within a wide range of parameters. The time series plots of original EEG signal, corrupted EEG signal, and EEG signal recovered

102

from the reconstructed sources from (6.7) by setting $\lambda = 0.02$ and $\beta = 0.01$, as well as the topoplots at 42 ms is given in Fig.6.10. To illustrate again the impact of the graph regularization, α is chosen from $\{0.01, 0.02, 0.05, 0.1, 0.5\}$. The first row is the EEG data generated from the task-related sources (persistent and low-rank), the second row is the EEG data from the task-related sources and the spurious source, the SNR is -0.72 dB, which means the energy of spurious source is slightly larger than the task-related sources. The 3rd row is the EEG data calculated from forward model after the source is reconstructed from our proposed model with $\alpha = 0.01$. The 4th-7th row is the time series plots when $\alpha = 0.02, 0.05, 0.1, 0.5$ respectively. The topoplots on the right part of Fig.6.10 is are sampled from 42 ms of the EEG data on the left.
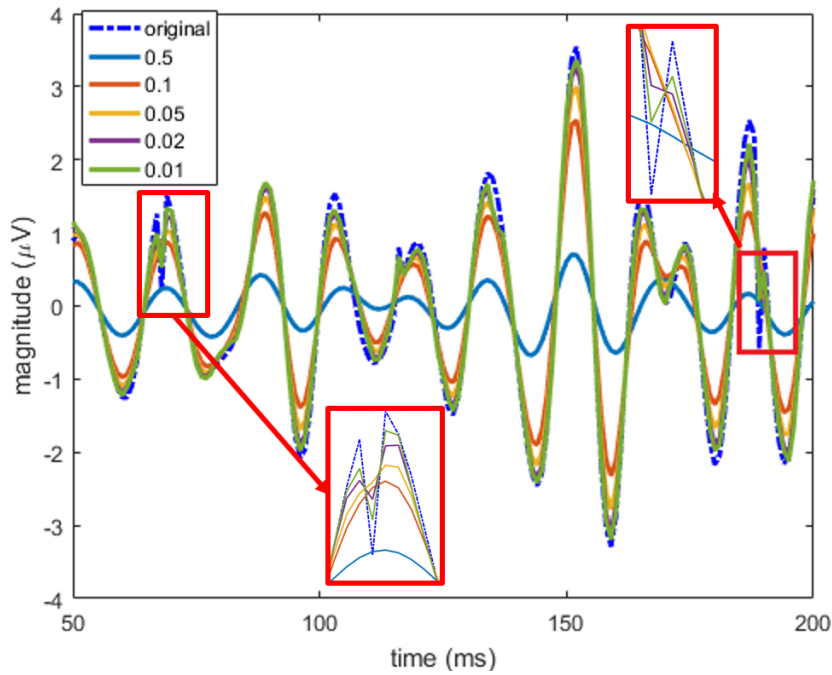
Figure 6.9: Illustration of the smoothing effect of temporal graph regularization: reconstructed time courses from varied graph regularization parameters.
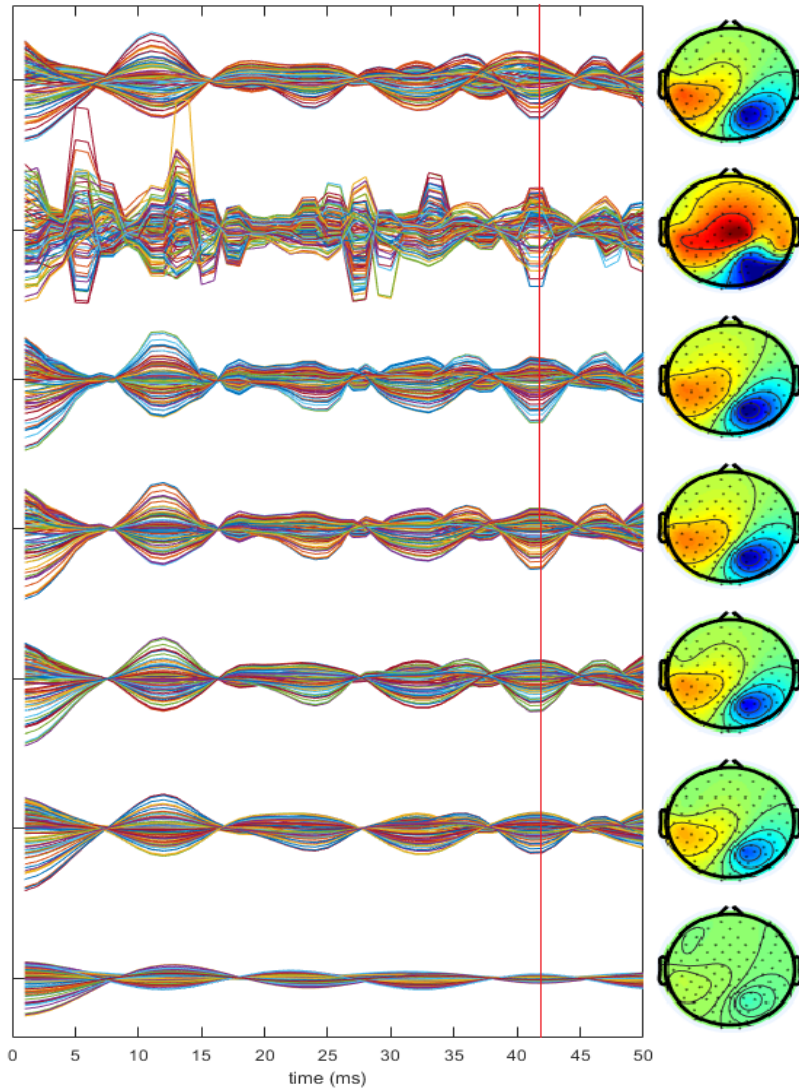
Figure 6.10: EEG time series plot of the uncorrupted EEG signal, corrupted EEG signal vs the reconstructed EEG signal using the proposed method and the corresponding topoplots at 42 ms: The 1st row is the time series plot of the original uncorrupted EEG data, the 2nd row is the plots for corrupted EEG data, the 3rd row is the EEG data reconstructed by applying our algorithm with $\alpha = 0.01$, the 4th row is the reconstructed EEG data with $\alpha = 0.02$, the 5th row is the reconstructed EEG data with $\alpha = 0.05$, the 6th row is the reconstructed EEG data with $\alpha = 0.10$, the 7th row is the reconstructed EEG data with $\alpha = 0.5$. The spurious source in the source space corrupted the task-related EEG data, and by using our graph regularized LRR model, the true EEG data can be recovered.

104

6.5.4   Experiments 3: Comprehensive Comparison with Benchmark Algorithms

The purpose of previous numerical experiments is to validate each term of the goal function and to understand their properties. The trade-off between low-rankness, data fidelity, sparsity, temporal smooth are fully discussed by varying different parameters. In this part, a comprehensive study is conducted to compare the proposed algorithm with the popular ESI algorithms such as MNE [31], sLORETA [71], MCE and well as the state-of-art algorithm mixed-norm estimate (MxNE) [26].

We generated independent sources in different ROIs for easy validation purpose, the number of independent sources varied from 2 to 4 corresponding to different rank of ground-truth source, and the number of spurious source are generated by randomly activating the sources on the cortex with a random scalar whose mean value to be 0, and the variance is 1. Moreover, the noise on sensor level is also added to the EEG data. Two of the MCE algorithms are selected, which are Homotopy and FISTA [93]. For MxNE algorithm, we choose $\ell_{2,1}$ to enforce ℓ_2 norm on the temporal time series of each voxel and ℓ_1 norm to impose spatial sparsity.

To measure the performance, we introduced 5 metrics, including 1) CPU time in seconds, 2) rank of the calculated source, 3) Sparsity, measuring the number of nonzero elements in the source space at each time point, 5) Reconstruction Error (RE) defined in Eq.(6.22), 5) Localization Error (LE), which is calculated using the shortest path algorithm over the irregular meshes from the reconstructed source location to the ground truth location. The LE metric is the most important one, since it measures the discrepancy in location, the other metrics give information of the property of the rendered solution. To calculate LE for each ROI with activated sources, we first locate source with

the largest activation magnitude in this ROI, and calculate the shortest path distance from the located source to the ground truth location. We conduct the same procedure for all the activated ROI, and calculate the average value of all the distances at each time point. The final LE is the averaged distance value for all the 500 time points for each experiments.

All the algorithms are implemented in Matlab except MxNE which we call as a Python script (MultiTaskLasso.py) under the linear model of scikit-learn library [72] from Matlab. The formulation for MxNE is

$$||X - LS||_F^2 + \gamma||S||_{2,1} \tag{6.23}$$

We found that parameter tuning process for MxNE algorithm is very time consuming, even though there is only one parameter for the unweighted version. If the parameter γ in Eq.(6.23) is tuned for one experiment with good performance, and we use the same setting of parameter and the same setting to generate random source activation patterns, the reconstructed source matrix can be a zero matrix. We tuned the parameter γ according to the best LE performance when the rank is 2 and the number of spurious activated source is 2. By conducting experiments for parameter tuning of MxNE, we set γ in Eq.(6.23). For our proposed algorithm, we set $\lambda = 0.01$ and $\beta = 0.01$, which were tested to have good performance for the same case when the rank is 2 and the number of spurious activated source is 2, and the graph parameter α is also set to be 0.01. 10 experiments were conducted under the same setting and the performance of all the algorithms are summarized in Table 6.1 to Table 6.3. The SNR is calculated after the noise signal is generated and it was averaged from 10 experiments under the same experiment

106

setting. As can be seen from the tables, our algorithm is the most accurate to locate the task related activated source. The CPU time of our algorithm is between Homotopy and FISTA algorithm. The running time for Python version of MxNE is much faster than our proposed algorithm, but there are many cases that MxNE algorithm failed, thus making the overall accuracy drop significantly. Although our algorithm have more parameter, it is a more sophisticated model that allows better controllability to customize the weight of different terms in the goal function. Although MxNE has large RE and LE, it is still worth noting that the MxNE algorithm we used is a simple version with $\ell_{2,1}$ norm discussed in Ref. [26], and the algorithm to solve the goal function 6.23 is coordinate descent, other algorithms can be tested to solve the same problem. MCE model solve using ℓ_1 algorithms Homotopy and FISTA can render good LE accuracy, and Homotopy outperforms FISTA in all the experiment with better speed, which confirms the comparison discussed in [50] [94].

Table 6.1: Source Reconstruction Performance Comparison (Rank=2)

Method	Rank =2; SNR= -0.356 dB					Rank =2; SNR= -1.12 dB					Rank =2; SNR= -1.67 dB				
	Time	Rank	Sparsity	RE	LE	Time	Rank	Sparsity	RE	LE	Time	Rank	Sparsity	RE	LE
Homotopy	0.41	449	65	0.80	2.02	0.41	449.8	84.4	0.95	3.31	0.50	459.3	91.15	0.97	4.57
FISTA	2.76	500	1812.4	0.62	3.93	2.76	500	1920.4	0.89	9.39	2.73	500	1888.0	0.80	11.25
sLORETA	0.055	500	2004	1.18	33.5	0.05	500	2004	1.26	34.13	0.056	500	2004.0	1.32	38.31
WMN	8.4e-5	107	2004	0.99	22.6	8.4e-5	107	2004	0.99	31.47	8.4e-5	107	2004.0	0.99	28.46
MxNE	0.026	7.9	7.9	0.95	42.1	0.023	10	10	0.97	45.79	0.028	11.8	11.8	1.04	68.80
Proposed	0.75	3.3	3.3	0.24	**0.145**	0.75	4.8	4.8	0.414	**1.94**	0.83	6.4	6.5	0.42	**2.27**

Table 6.2: Source Reconstruction Performance Comparison (Rank=3)

Method	Rank =3; SNR= 0.938 dB					Rank =3; SNR= -0.174 dB					Rank =3; SNR= -0.784 dB				
	Time	Rank	Sparsity	RE	LE	Time	Rank	Sparsity	RE	LE	Time	Rank	Sparsity	RE	LE
Homotopy	0.36	445.4	77.6	0.64	5.18	0.48	464	87.2	0.68	6.1	0.46	474.1	92.5	0.84	5.88
FISTA	2.64	500	1812.5	0.69	9.33	2.56	500	1969.0	1.23	21.5	2.67	500	1939.2	0.94	17.44
sLORETA	0.057	500	2004	1.90	41.93	0.06	500	2004	1.81	43.9	0.05	500	2004.0	1.25	46.60
WMN	8.4e-5	107	2004	6.79	29.55	7.6e-5	107	2004	6.82	35.63	7.3e-5	107	2004.0	0.99	34.41
MxNE	0.026	9.2	9.2	0.91	64.95	0.028	10	10	0.98	67.95	0.028	12.2	12.2	0.96	57.49
Proposed	0.72	5.2	5.2	0.43	**2.98**	0.80	6.1	6.1	0.488	**3.82**	0.75	7.3	7.3	0.45	**2.86**

Table 6.3: Source Reconstruction Performance Comparison (Rank=4)

Method	Rank = 4; SNR= 1.04 dB					Rank =4; SNR= 0.603 dB					Rank =4; SNR= −0.179 dB				
	Time	Rank	Sparsity	RE	LE	Time	Rank	Sparsity	RE	LE	Time	Rank	Sparsity	RE	LE
Homotopy	0.45	448	78.7	0.57	3.77	0.41	467.3	87.9	0.62	5.87	0.46	475.1	93.15	0.62	5.35
FISTA	2.97	500	1978.7	1.03	16.54	2.46	500	1964.5	1.01	16.64	2.45	500	1961.9	1.35	19.4
sLORETA	0.058	500	2004	1.99	45.3	0.058	500	2004	1.72	49.26	0.050	500	2004.0	1.71	49.38
WMN	7.8e-5	107	2004	7.43	31.0	7.8e-5	107	2004	6.63	33.49	7.8e-5	107	2004.0	6.66	38.00
MxNE	0.024	11.9	11.9	0.997	68.36	0.023	11.7	11.7	0.947	56.42	0.025	13.9	13.9	0.99	61.46
Proposed	0.79	5.9	6.8	0.38	**2.24**	6.9	7.8	7.8	0.43	**3.90**	0.76	10.1	14.3	0.44	**4.5**

6.6 Conclusion

In this chapter, we propose to consider the noise not only on the sensor level, but also in the source space. We come up with an EEG source imaging model based on temporal graph structures and low-rank representation. The model is solved with our proposed algorithm based on ADMM. Numerical experiments are conducted to verify the effectiveness of the proposed work on discovering task related low-rank sources. We delineate the discussion on the properties and impacts for each term in the cost function to help better understand our proposed graph regularized low rank representation model. Compared the traditional model, our proposed one can find the intrinsic task related activation patterns and suppress the spurious source patterns.

Chapter 7

Conclusion and Future Work

In summary, we proposed the concept of discriminative ESI which aims to find the task-related sources and reduce the contamination from high background noises or spurious sources, and reformulated the traditional ESI problem by inclusion of label information. We use the state-of-art sparse representation algorithms to recover the task related spatial and temporal smooth regularizations. Discriminative source activation pattern corresponding to different cognitive tasks provides more insights compared to the activation pattern reconstructed from traditional methods. To discover discriminative ESI, label information was integrated to the traditional ESI problem, and several frameworks have been proposed: (1) A sparse dictionary learning framework was proposed and a revised version of discriminative K-SVD (DK-SVD) algorithm is given to solve the formulated supervised dictionary learning problem. As the proposed learning framework incorporated the EEG label information of different brain status, it is capable of learning a sparse representation that reveal the most discriminative brain activity sources among different brain states. (2) A graph regularized ESI model, which implicitly use label information in the graph regularization term to promote in-class consistency and out-class discrimination, an efficient algorithm called feature sign search used used to optimize the proposed model. (3) As ESI always favors spatially smooth activation pattern instead of isolated discrete activations, we included first-order to-

tal variation (TV) and spatial graph Fractional Order Total Variation (gFOTV) with ADMM algorithm and practical technique to find a better spatially smoothing source activations. (4) Traditional EEG Source Imaging (ESI) methods usually do not distinguish the task-related and spurious non-task-related sources that jointly generate EEG signal, which will inevitable yield misleading reconstructed activation patterns. We proposed to infer the true task-related EEG sources location by exploiting its low-rank property. To find a source activation pattern with low rank structure, thus a novel ESI models based on low-rank representation was developed. Simulation results illustrates the effectiveness of those several proposed methods under different Signal Noise Ratio (SNR) and variant of source configuration settings.

The future work can be summarized as below:

- Combine EEG and fMRI data for better source localization. As EEG always contains a lot of noise, the source localization performance can be bad due to those noise. Better prior can be included. fMRI can provide good prior information with high spatial resolution. Multi-modality analysis should be very beneficial for EEG source localization.

- There are many ways to build the head model, and to explore different setup of head models on the performance of ESI algorithms should be beneficial to guide the procedure of building better head models. The discussion on the impact of tissue conductivity value, choice of BEM or FEM algorithms, choice of will arouse a lot of interests to the ESI community.

- As deep learning exhibits great potential of solving image reconstruction inverse

problem, an use of deep learning to solve EEG inverse problem should be explored.

- ESI for Ictal EEG. As Ictal EEG contains less noise, ESI with real data Ictal EEG can be more accurate than scalp EEG. Future research should combine ESI and functional connectivity to find the driver of the seizure using Ictal EEG data.

Bibliography

[1] Headmodel of aojeda. `https://github.com/aojeda/headModel`. Accessed: 2018-02-23.

[2] ACAR, Z. A., AND MAKEIG, S. Neuroelectromagnetic forward head modeling toolbox. *Journal of neuroscience methods 190*, 2 (2010), 258–270.

[3] AHARON, M., ELAD, M., AND BRUCKSTEIN, A. K-SVD: An algorithm for designing overcomplete dictionaries for sparse representation. *IEEE Transactions on Signal Processing 54*, 11 (Nov 2006), 4311–4322.

[4] ANWAR, A., MUTHALIB, M., PERREY, S., GALKA, A., GRANERT, O., WOLFF, S., HEUTE, U., DEUSCHL, G., RAETHJEN, J., AND MUTHURAMAN, M. Effective connectivity of cortical sensorimotor networks during finger movement tasks: a simultaneous fnirs, fmri, eeg study. *Brain topography 29*, 5 (2016), 645–660.

[5] ASIF, M. S., AND ROMBERG, J. Sparse recovery of streaming signals using ℓ_1-homotopy. *IEEE Transactions on Signal Processing 62*, 16 (2014), 4209–4223.

[6] BABADI, B., OBREGON-HENAO, G., LAMUS, C., HÄMÄLÄINEN, M. S., BROWN, E. N., AND PURDON, P. L. A subspace pursuit-based iterative greedy hierar-

chical solution to the neuromagnetic inverse problem. *NeuroImage 87* (2014), 427–443.

[7] BAI, J., AND FENG, X. Fractional-order anisotropic diffusion for image denoising. *IEEE Transactions on Image Processing 16*, 10 (2007), 2492–2502.

[8] BAILLET, S., AND GARNERO, L. A bayesian approach to introducing anatomo-functional priors in the eeg/meg inverse problem. *IEEE Transactions on Biomedical Engineering 44*, 5 (1997), 374–385.

[9] BARTON, M. J., ROBINSON, P. A., KUMAR, S., GALKA, A., DURRANT-WHYTE, H. F., GUIVANT, J., AND OZAKI, T. Evaluating the performance of kalman-filter-based eeg source localization. *IEEE transactions on biomedical engineering 56*, 1 (2009), 122–136.

[10] BECKER, H., ALBERA, L., COMON, P., GRIBONVAL, R., AND MERLET, I. Fast, variation-based methods for the analysis of extended brain sources. In *Signal Processing Conference (EUSIPCO), 2014 Proceedings of the 22nd European* (2014), IEEE, pp. 41–45.

[11] BEKHTI, Y., LUCKA, F., SALMON, J., AND GRAMFORT, A. A hierarchical bayesian perspective on majorization-minimization for non-convex sparse regression: application to M/EEG source imaging. *arXiv preprint arXiv:1710.08747* (2017).

[12] BOYD, S., PARIKH, N., CHU, E., PELEATO, B., AND ECKSTEIN, J. Distributed optimization and statistical learning via the alternating direction method

of multipliers. *Foundations and Trends in Machine Learning 3*, 1 (2011), 1–122.

[13] CAI, B., ZILLE, P., STEPHEN, J. M., WILSON, T. W., CALHOUN, V. D., AND WANG, Y. P. Estimation of dynamic sparse connectivity patterns from resting state fmri. *IEEE Transactions on Medical Imaging* (2017).

[14] CAI, D., HE, X., HAN, J., AND HUANG, T. S. Graph regularized nonnegative matrix factorization for data representation. *IEEE Transactions on Pattern Analysis and Machine Intelligence 33*, 8 (2011), 1548–1560.

[15] CAI, J.-F., CANDÈS, E. J., AND SHEN, Z. A singular value thresholding algorithm for matrix completion. *SIAM Journal on Optimization 20*, 4 (2010), 1956–1982.

[16] CASTAÑO-CANDAMIL, S., HÖHNE, J., MARTÍNEZ-VARGAS, J.-D., AN, X.-W., CASTELLANOS-DOMÍNGUEZ, G., AND HAUFE, S. Solving the EEG inverse problem based on space–time–frequency structured sparsity constraints. *NeuroImage 118* (2015), 598–612.

[17] CHEN, D., SUN, S., ZHANG, C., CHEN, Y., AND XUE, D. Fractional-order TV-L2 model for image denoising. *Central European Journal of Physics 11*, 10 (2013), 1414–1422.

[18] CHEN, G. Automatic EEG seizure detection using dual-tree complex wavelet-fourier features. *Expert Systems with Applications 41*, 5 (2014), 2391–2394.

[19] COSTA, F., BATATIA, H., CHAARI, L., AND TOURNERET, J.-Y. Sparse EEG source localization using bernoulli laplacian priors. *IEEE Transactions on Biomedical Engineering 62*, 12 (2015), 2888–2898.

[20] COSTA, F., BATATIA, H., OBERLIN, T., D'GIANO, C., AND TOURNERET, J.-Y. Bayesian eeg source localization using a structured sparsity prior. *NeuroImage 144* (2017), 142–152.

[21] CUSTO, A., VULLIEMOZ, S., GROUILLER, F., VAN DE VILLE, D., AND MICHEL, C. Eeg source imaging of brain states using spatiotemporal regression. *Neuroimage 96* (2014), 106–116.

[22] DING, L. Reconstructing cortical current density by exploring sparseness in the transform domain. *Physics in Medicine and Biology 54*, 9 (2009), 2683.

[23] DONOHO, D. L. For most large underdetermined systems of linear equations the minimal 1-norm solution is also the sparsest solution. *Communications on pure and applied mathematics 59*, 6 (2006), 797–829.

[24] DU, S., MA, Y., AND MA, Y. Graph regularized compact low rank representation for subspace clustering. *Knowledge-Based Systems 118* (2017), 56–69.

[25] FRISTON, K. J., HOLMES, A. P., WORSLEY, K. J., POLINE, J.-P., FRITH, C. D., AND FRACKOWIAK, R. S. Statistical parametric maps in functional imaging: a general linear approach. *Human brain mapping 2*, 4 (1994), 189–210.

[26] GRAMFORT, A., KOWALSKI, M., AND HÄMÄLÄINEN, M. Mixed-norm estimates for the M/EEG inverse problem using accelerated gradient methods. *Physics in medicine and biology 57*, 7 (2012), 1937.

[27] GRAMFORT, A., PAPADOPOULO, T., OLIVI, E., AND CLERC, M. Openmeeg: opensource software for quasistatic bioelectromagnetics. *Biomedical engineering online 9*, 1 (2010), 45.

[28] GRAMFORT, A., STROHMEIER, D., HAUEISEN, J., HÄMÄLÄINEN, M. S., AND KOWALSKI, M. Time-frequency mixed-norm estimates: Sparse M/EEG imaging with non-stationary source activations. *NeuroImage 70* (2013), 410–422.

[29] GRECH, R., CASSAR, T., MUSCAT, J., CAMILLERI, K. P., FABRI, S. G., ZERVAKIS, M., XANTHOPOULOS, P., SAKKALIS, V., AND VANRUMSTE, B. Review on solving the inverse problem in EEG source analysis. *Journal of Neuroengineering and Rehabilitation 5*, 1 (2008), 1.

[30] GUO, H., JIANG, Z., AND DAVIS, L. S. Discriminative dictionary learning with pairwise constraints. In *Asian Conference on Computer Vision* (2012), Springer, pp. 328–342.

[31] HÄMÄLÄINEN, M. S., AND ILMONIEMI, R. J. Interpreting magnetic fields of the brain: minimum norm estimates. *Medical & Biological Engineering Computing 32*, 1 (1994), 35–42.

[32] HASSAN, M., DUFOR, O., MERLET, I., BERROU, C., AND WENDLING, F. EEG source connectivity analysis: from dense array recordings to brain networks. *PloS one 9*, 8 (2014), e105041.

[33] HAUFE, S. *Towards EEG source connectivity analysis*. PhD thesis, Technical University of Berlin, 10623 Berlin, Germany, Nov. 2011.

[34] HAUFE, S., AND EWALD, A. A simulation framework for benchmarking EEG-based brain connectivity estimation methodologies. *Brain topography* (2016), 1–18.

[35] HAUFE, S., NIKULIN, V. V., ZIEHE, A., MÜLLER, K.-R., AND NOLTE, G. Combining sparsity and rotational invariance in EEG/MEG source reconstruction. *NeuroImage 42*, 2 (2008), 726–738.

[36] HE, X., CAI, D., YAN, S., AND ZHANG, H.-J. Neighborhood preserving embedding. In *Computer Vision, 2005. ICCV 2005. Tenth IEEE International Conference on* (2005), vol. 2, IEEE, pp. 1208–1213.

[37] HE, X., YAN, S., HU, Y., NIYOGI, P., AND ZHANG, H.-J. Face recognition using laplacianfaces. *IEEE transactions on pattern analysis and machine intelligence 27*, 3 (2005), 328–340.

[38] HIPP, J. F., HAWELLEK, D. J., CORBETTA, M., SIEGEL, M., AND ENGEL, A. K. Large-scale cortical correlation structure of spontaneous oscillatory activity. *Nature neuroscience 15*, 6 (2012), 884–890.

[39] HUANG, Y., PARRA, L. C., AND HAUFE, S. The new york head -a precise standardized volume conductor model for EEG source localization and tes targeting. *NeuroImage 140* (2016), 150 – 162. Transcranial electric stimulation (tES) and Neuroimaging.

[40] HUANG, Y., PARRA, L. C., AND HAUFE, S. The new york heada precise standardized volume conductor model for EEG source localization and tES targeting. *NeuroImage 140* (2016), 150 – 162.

[41] JIANG, Z., LIN, Z., AND DAVIS, L. S. Label consistent K-SVD: Learning a discriminative dictionary for recognition. *IEEE Transactions on Pattern Analysis and Machine Intelligence 35*, 11 (2013), 2651–2664.

[42] KOULOURI, A. Reconstruction of electric fields and source distributions in eeg brain imaging.

[43] LAMUS, C., HÄMÄLÄINEN, M. S., TEMEREANCA, S., BROWN, E. N., AND PURDON, P. L. A spatiotemporal dynamic distributed solution to the MEG inverse problem. *NeuroImage 63*, 2 (2012), 894–909.

[44] LEAHY, R., MOSHER, J., SPENCER, M., HUANG, M., AND LEWINE, J. A study of dipole localization accuracy for meg and eeg using a human skull phantom. *Electroencephalography and clinical neurophysiology 107*, 2 (1998), 159–173.

[45] LEE, H., BATTLE, A., RAINA, R., AND NG, A. Y. Efficient sparse coding algorithms. In *Advances in neural information processing systems* (2006), pp. 801–

808.

[46] LI, C., JACOBS, D., HILTON, T., DEL CAMPO, M., CHINVARUN, Y., CARLEN, P. L., AND BARDAKJIAN, B. L. Epileptogenic source imaging using cross-frequency coupled signals from scalp eeg. *IEEE Transactions on Biomedical Engineering 63*, 12 (2016), 2607–2618.

[47] LI, Y., QIN, J., HSIN, Y.-L., OSHER, S., AND LIU, W. s-SMOOTH: Sparsity and smoothness enhanced EEG brain tomography. *Frontiers in Neuroscience 10* (2016), 543.

[48] LIN, Z., LIU, R., AND SU, Z. Linearized alternating direction method with adaptive penalty for low-rank representation. In *Advances in neural information processing systems* (2011), pp. 612–620.

[49] LIU, F., HOSSEINI, R., ROSENBERGER, J., WANG, S., AND SU, J. Supervised discriminative EEG brain source imaging with graph regularization. In *International Conference on Medical Image Computing and Computer-Assisted Intervention (MICCAI) (in press)* (2017), Springer.

[50] LIU, F., ROSENBERGER, J., LOU, Y., HOSSEINI, R., SU, J., AND WANG, S. Graph regularized eeg source imaging with in-class consistency and out-class discrimination. *IEEE Transactions on Big Data 3*, 4 (Dec 2017), 378–391.

[51] LIU, F., WANG, S., ROSENBERGER, J., SU, J., AND LIU, H. A sparse dictionary learning framework to discover discriminative source activations in eeg brain mapping. In *AAAI* (2017), pp. 1431–1437.

[52] LIU, F., XIANG, W., WANG, S., AND LEGA, B. Prediction of seizure spread network via sparse representations of overcomplete dictionaries. In *International Conference on Brain and Health Informatics* (2016), pp. 262–273.

[53] LIU, G., LIN, Z., YAN, S., SUN, J., YU, Y., AND MA, Y. Robust recovery of subspace structures by low-rank representation. *IEEE Transactions on Pattern Analysis and Machine Intelligence 35*, 1 (2013), 171–184.

[54] LIU, H., SCHIMPF, P. H., DONG, G., GAO, X., YANG, F., AND GAO, S. Standardized shrinking LORETA-FOCUSS (SSLOFO): a new algorithm for spatio-temporal EEG source reconstruction. *IEEE Transactions on Biomedical Engineering 52*, 10 (2005), 1681–1691.

[55] LIU, K., YU, Z. L., WU, W., GU, Z., AND LI, Y. Straps: A fully data-driven spatio-temporally regularized algorithm for M/EEG patch source imaging. *International journal of neural systems 25*, 04 (2015), 1550016.

[56] LIU, K., YU, Z. L., WU, W., GU, Z., LI, Y., AND NAGARAJAN, S. Bayesian electromagnetic spatio-temporal imaging of extended sources with markov random field and temporal basis expansion. *NeuroImage 139* (2016), 385–404.

[57] LONG, C., PURDON, P., TEMEREANCA, S., DESAI, N., HAMALAINEN, M., AND BROWN, E. Large scale kalman filtering solutions to the electrophysiological source localization problem-a meg case study. In *Engineering in Medicine and Biology Society, 2006. EMBS'06. 28th Annual International Conference of the IEEE* (2006), IEEE, pp. 4532–4535.

[58] LU, X., WANG, Y., AND YUAN, Y. Graph-regularized low-rank representation for destriping of hyperspectral images. *IEEE transactions on geoscience and remote sensing 51*, 7 (2013), 4009–4018.

[59] LU, X., YUAN, H., YAN, P., YUAN, Y., AND LI, X. Geometry constrained sparse coding for single image super-resolution. In *Computer Vision and Pattern Recognition (CVPR), 2012 IEEE Conference on* (2012), IEEE, pp. 1648–1655.

[60] MACHADO, S., ARIAS-CARRIÓN, O., SAMPAIO, I., BITTENCOURT, J., VELASQUES, B., TEIXEIRA, S., NARDI, A. E., PIEDADE, R., AND RIBEIRO, P. Source imaging of p300 visual evoked potentials and cognitive functions in healthy subjects. *Clinical EEG and neuroscience* (2014), 1550059413514389.

[61] MAHJOORY, K., NIKULIN, V. V., BOTREL, L., LINKENKAER-HANSEN, K., FATO, M. M., AND HAUFE, S. Consistency of EEG source localization and connectivity estimates. *NeuroImage 152* (2017), 590–601.

[62] MÉGEVAND, P., SPINELLI, L., GENETTI, M., BRODBECK, V., MOMJIAN, S., SCHALLER, K., MICHEL, C. M., VULLIEMOZ, S., AND SEECK, M. Electric source imaging of interictal activity accurately localises the seizure onset zone. *J Neurol Neurosurg Psychiatry 85*, 1 (2014), 38–43.

[63] MHEICH, A., HASSAN, M., DUFOR, O., KHALIL, M., AND WENDLING, F. Combining eeg source connectivity and network similarity: Application to object categorization in the human brain. *arXiv preprint arXiv:1606.01017* (2016).

[64] MICHEL, C. M., MURRAY, M. M., LANTZ, G., GONZALEZ, S., SPINELLI, L., AND DE PERALTA, R. G. EEG source imaging. *Clinical neurophysiology 115*, 10 (2004), 2195–2222.

[65] MICHEL, V., GRAMFORT, A., VAROQUAUX, G., EGER, E., AND THIRION, B. Total variation regularization for fmri-based prediction of behavior. *IEEE transactions on medical imaging 30*, 7 (2011), 1328–1340.

[66] NIE, F., HUANG, H., CAI, X., AND DING, C. H. Efficient and robust feature selection via joint $\ell_{2,1}$-norms minimization. In *Advances in neural information processing systems* (2010), pp. 1813–1821.

[67] OLDHAM, K. B., AND SPANIER, J. *The Fractional Calculus.* Academic Press, New York, 1974.

[68] OOSTENVELD, R., FRIES, P., MARIS, E., AND SCHOFFELEN, J.-M. Fieldtrip: open source software for advanced analysis of meg, eeg, and invasive electro-physiological data. *Computational intelligence and neuroscience 2011* (2011), 1.

[69] OU, W., HÄMÄLÄINEN, M. S., AND GOLLAND, P. A distributed spatio-temporal EEG/MEG inverse solver. *NeuroImage 44*, 3 (2009), 932–946.

[70] PARKER, S. G., AND JOHNSON, C. R. Scirun: a scientific programming environment for computational steering. In *Proceedings of the 1995 ACM/IEEE conference on Supercomputing* (1995), ACM, p. 52.

[71] PASCUAL-MARQUI, R. D., ET AL. Standardized low-resolution brain electromagnetic tomography (sLORETA): technical details. *Methods Find Exp Clin Pharmacol 24*, Suppl D (2002), 5–12.

[72] PEDREGOSA, F., VAROQUAUX, G., GRAMFORT, A., MICHEL, V., THIRION, B., GRISEL, O., BLONDEL, M., PRETTENHOFER, P., WEISS, R., DUBOURG, V., ET AL. Scikit-learn: Machine learning in python. *Journal of Machine Learning Research 12*, Oct (2011), 2825–2830.

[73] PERRIER, J., CLOCHON, P., BERTRAN, F., COUQUE, C., BULLA, J., DENISE, P., AND BOCCA, M.-L. Specific EEG sleep pattern in the prefrontal cortex in primary insomnia. *PloS one 10*, 1 (2015), e0116864.

[74] PHAM, D. S., AND VENKATESH, S. Joint learning and dictionary construction for pattern recognition. In *2008 IEEE Conference on Computer Vision and Pattern Recognition* (June 2008), pp. 1–8.

[75] QIN, J., LIU, F., WANG, S., AND ROSENBERGER, J. Eeg source imaging based on spatial and temporal graph structures. In *International Conference on Image Processing Theory, Tools and Applications* (2017).

[76] RAICHLE, M. E. The brain's dark energy. *Science 314*, 5803 (2006), 1249–1250.

[77] RAMIREZ, I., SPRECHMANN, P., AND SAPIRO, G. Classification and clustering via dictionary learning with structured incoherence and shared features. In

Computer Vision and Pattern Recognition (CVPR), 2010 IEEE Conference on (2010), IEEE, pp. 3501–3508.

[78] REN, Z., HE, C., AND ZHANG, Q. Fractional order total variation regularization for image super-resolution. *Signal Processing 93*, 9 (2013), 2408–2421.

[79] ROWEIS, S. T., AND SAUL, L. K. Nonlinear dimensionality reduction by locally linear embedding. *science 290*, 5500 (2000), 2323–2326.

[80] SOHRABPOUR, A., LU, Y., KANKIRAWATANA, P., BLOUNT, J., KIM, H., AND HE, B. Effect of eeg electrode number on epileptic source localization in pediatric patients. *Clinical Neurophysiology 126*, 3 (2015), 472–480.

[81] SOHRABPOUR, A., LU, Y., WORRELL, G., AND HE, B. Imaging brain source extent from EEG/MEG by means of an iteratively reweighted edge sparsity minimization (ires) strategy. *NeuroImage 142* (2016), 27–42.

[82] SONG, C., ZHUANG, T., AND WU, Q. Hybrid weighted minimum norm method a new method based LORETA to solve EEG inverse problem. In *2005 IEEE Engineering in Medicine and Biology 27th Annual Conference* (2006), pp. 1079–1082.

[83] STROHMEIER, D., BEKHTI, Y., HAUEISEN, J., AND GRAMFORT, A. The iterative reweighted mixed-norm estimate for spatio-temporal MEG/EEG source reconstruction. *IEEE transactions on medical imaging 35*, 10 (2016), 2218–2228.

[84] TADEL, F., BAILLET, S., MOSHER, J. C., PANTAZIS, D., AND LEAHY, R. M. Brainstorm: a user-friendly application for meg/eeg analysis. *Computational intelligence and neuroscience 2011* (2011), 8.

[85] UUTELA, K., HÄMÄLÄINEN, M., AND SOMERSALO, E. Visualization of magnetoencephalographic data using minimum current estimates. *NeuroImage 10*, 2 (1999), 173–180.

[86] VEGA-HERNÁNDEZ, M., MARTÍNEZ-MONTES, E., SÁNCHEZ-BORNOT, J. M., LAGE-CASTELLANOS, A., AND VALDÉS-SOSA, P. A. Penalized least squares methods for solving the EEG inverse problem. *Statistica Sinica* (2008), 1535–1551.

[87] WIPF, D., AND NAGARAJAN, S. A unified bayesian framework for meg/eeg source imaging. *NeuroImage 44*, 3 (2009), 947–966.

[88] WOODBURY, M. A. Inverting modified matrices. *Memorandum report 42* (1950), 106.

[89] WRIGHT, J., AND MA, Y. Dense error correction via ℓ^1-minimization. *IEEE Transactions on Information Theory 56*, 7 (2010), 3540–3560.

[90] WRIGHT, J., MA, Y., MAIRAL, J., SAPIRO, G., HUANG, T. S., AND YAN, S. Sparse representation for computer vision and pattern recognition. *Proceedings of the IEEE 98*, 6 (2010), 1031–1044.

[91] XIANG, J., WANG, Y., CHEN, Y., LIU, Y., KOTECHA, R., HUO, X., ROSE, D. F., FUJIWARA, H., HEMASILPIN, N., LEE, K., ET AL. Noninvasive local-

ization of epileptogenic zones with ictal high-frequency neuromagnetic signals: Case report. *Journal of Neurosurgery: Pediatrics 5*, 1 (2010), 113–122.

[92] YAMASHITA, O., GALKA, A., OZAKI, T., BISCAY, R., AND VALDES-SOSA, P. Recursive penalized least squares solution for dynamical inverse problems of eeg generation. *Human brain mapping 21*, 4 (2004), 221–235.

[93] YANG, A. Y., SASTRY, S. S., GANESH, A., AND MA, Y. Fast ℓ 1-minimization algorithms and an application in robust face recognition: A review. In *Image Processing (ICIP), 2010 17th IEEE International Conference on* (2010), IEEE, pp. 1849–1852.

[94] YANG, J., YIN, W., ZHANG, Y., AND WANG, Y. A fast algorithm for edge-preserving variational multichannel image restoration. *SIAM Journal on Imaging Sciences 2*, 2 (2009), 569–592.

[95] YANG, M., ZHANG, L., FENG, X., AND ZHANG, D. Sparse representation based fisher discrimination dictionary learning for image classification. *International Journal of Computer Vision 109*, 3 (2014), 209–232.

[96] YANG, Y., AMINOFF, E., TARR, M., AND ROBERT, K. E. A state-space model of cross-region dynamic connectivity in MEG/EEG. In *Advances in Neural Information Processing Systems* (2016), pp. 1234–1242.

[97] YIN, M., GAO, J., AND LIN, Z. Laplacian regularized low-rank representation and its applications. *IEEE transactions on pattern analysis and machine intelligence 38*, 3 (2016), 504–517.

[98] YIN, M., GAO, J., LIN, Z., SHI, Q., AND GUO, Y. Dual graph regularized latent low-rank representation for subspace clustering. *IEEE Transactions on Image Processing 24*, 12 (2015), 4918–4933.

[99] ZHANG, Q., AND LI, B. Discriminative K-SVD for dictionary learning in face recognition. In *2010 IEEE Computer Society Conference on Computer Vision and Pattern Recognition* (June 2010), pp. 2691–2698.

[100] ZHANG, Z., XU, Y., YANG, J., LI, X., AND ZHANG, D. A survey of sparse representation: algorithms and applications. *IEEE access 3* (2015), 490–530.

[101] ZHU, M., ZHANG, W., DICKENS, D. L., AND DING, L. Reconstructing spatially extended brain sources via enforcing multiple transform sparseness. *NeuroImage 86* (2014), 280–293.

Vita

Feng Liu was born in Dezhou, Shandong Province, China on August 8th, 1987. He received the Bachelor of Engineering degree from Qingdao University, Qingdao, China in 2010, and Master of Engineering degree from Huazhong University of Science and Technology in 2013. Starting from Jan 2013 to May 2014, he was a Ph.D. student in Electrical and Computer Engineering department in Virginia Commonwealth University, Richmond VA, and in Aug 2014, he transferred to University of Texas at Arlington pursuing a Ph.D. degree in Industrial Engineering. From May 2015 to Jan 2016, he worked as an Operations Research (machine learning) intern in CSX Transportation Corporation in Jacksonville, Florida. His research interests include machine learning for computational neuroscience, chaotic dynamical systems, control theory. He has published multiple papers on Chaos, Neurocomputing, PLOS One, MICCAI, AAAI, IEEE Transactions on Big data, etc. He is an active reviewer for Information Sciences, Neurocomputing, Physica A, Brain Informatics, etc.

Permanent address: 19251 Preston Rd
                        Dallas, Texas 75252